RF SPUTTERED Si_xGe_{1-x} AND $Si_xGe_{1-x}O_y$ THIN FILMS FOR UNCOOLED INFRARED DETECTORS

by

MUKTI M RANA

Presented to the Faculty of the Graduate School of
The University of Texas at Arlington in Partial Fulfillment
of the Requirements
for the Degree of

DOCTOR OF PHILOSOPHY

THE UNIVERSITY OF TEXAS AT ARLINGTON
MAY 2007

To my parents - Abul Kasem and Monwara Begum

ACKNOWLEDGEMENTS

"Praise be to Allah, the lord of the worlds." First I would like to thank to Professor Donald Butler for his continuous monitoring, support, advice and guidance to finish my PhD. Since I started to work under his supervision (Fall, 2003), I had every freedom to talk with him for any of the research related field. I found him helpful and courteous at all occasions. I would like to thank to Professor Zeynep Çelik-Butler for her help at different times particularly during noise measurement. I would like to thank other members of my dissertation committee Professor Ronald Carter, Dr. Rasool Kenerangui, Dr. Choong-Un Kim for giving their consent to be in my committee. I would like to provide special thanks to Dr. Aamer Mahmood, Dr. Mazharul Haque and Asutosh Dave-all my former colleagues for their help during device fabrication and characterization. I would to thank my other colleagues-Min, Shiva, Murali, Sandeep, Tanvir, Shariar, Vinayak, Suraj, Vijay, Erkin for their help.

My parents and my parents in laws helped me by proving financial and mental supports for finishing my PhD. I would like to thank them along with my sister Bilkis and my brother in law Selim and sister in law Senjuti for their support. I would like to thank to my other brothers and sisters - Hasan, Zubery, and Jakelin for their encouragement to finish my PhD. I would like to thank to Yunus Patel for his support.

I would like to thank to Nano Fab staffs Dr. Nasir Basit, Dennis Bueno, Jim Florence, Susan Stoltje and former staff Dr. Vance Ley and Dr. Ashwath and Michael Coviello, Rashed of Material Science Engineering for their help at different times.

Up in the front, I have to mention the name of my wife Tahnia Ashrafi who had provided me with mental support and encouragement.

February 23, 2007

ABSTRACT

RF SPUTTERED Si_xGe_{1-x} and $Si_xGe_{1-x}O_y$ THIN FILMS FOR UNCOOLED INFRARED DETECTORS

Publication No. ______

Mukti M Rana, PhD.

The University of Texas at Arlington, 2007

Supervising Professor: Donald P Butler

The objective of this work is to test the feasibility of using radio frequency (RF) magnetron sputtered Si_xGe_{1-x} and $Si_xGe_{1-x}O_y$ thin films as the sensing material in uncooled infrared detectors, and find a suitable combination of Si_xGe_{1-x} and $Si_xGe_{1-x}O_y$ thin films for this purpose. Thus, fabricating and characterizing microbolometers by using Si_xGe_{1-x} and $Si_xGe_{1-x}O_y$ thin films as the sensing material are the ultimate goal of this work.

Thin films of Si_xGe_{1-x} and $Si_xGe_{1-x}O_y$ were deposited by RF magnetron sputtering at room temperature from a single target of Si_xGe_{1-x} in Ar or Ar : O_2 environment. The silicon and oxygen concentrations were varied in a parametric investigation of the dependence of the electrical and optical characteristics of the thin films on composition. As Si concentration was increased in Si_xGe_{1-x} films, the temperature coefficient of resistance (TCR) was decreased. For $Si_xGe_{1-x}O_y$ films, the addition of oxygen to Si_xGe_{1-x}, increased the activation energy, and TCR. TCR was measured to vary from -2.27 %/K to -8.69 %/K. The optical bandgap was increased with the increasing concentration of oxygen in $Si_xGe_{1-x}O_{y.}$ To compare 1/*f*-noise from each film, the value of the volume normalized Hooge coefficient was determined for all the films. The normalized Hooge coefficient was found to increase with the increasing concentration of O_2. With the addition of O_2 to Si_xGe_{1-x}, the transmittance of the films found to be increased while the reflectance remained almost constant. The optical bandgap was increased with the increasing concentration of O_2. A suitable atomic composition of $Si_xGe_{1-x}O_y$ for uncooled infrared detector applications was found to have a TCR of -5.10 %/K.

Microbolometers of doped Si_xGe_{1-x} were fabricated and characterized. A TCR of 1.25%/K with a device resistance of 41.4 KΩ was achieved. Thermal conductivity was found to be 1×10^{-5} WK^{-1} for these doped Si_xGe_{1-x} microbolometers. The presence of high 1/*f*-noise was observed which caused to degrade bolometers performance.

Uncooled $Si_xGe_{1-x}O_y$ microbolometers were fabricated and passivated by forming gas at 250 °C for different interval of time to reduce noise. The value of normalized Hooge coefficient for 1/*f*-noise (K_f) was decreased from 7.54×10^{-7} to 2.21×10^{-10} after 8 hours of forming gas passivation performed at 250 °C. The highest

responsivity and detectivity obtained from $Si_xGe_{1-x}O_y$:H microbolometers were 1.05×10^4 (V/W) and 8.27×10^6 (cm-$Hz^{1/2}$/W) respectively while the room temperature TCR was -4.80%/K. The lowest thermal conductivity was found to be 4×10^{-8} WK^{-1}.

Cavity based tunable Fabry-Perot microspectrometer was fabricated using bulk micromachining technology. The device was fabricated by using Al_2O_3 as the support layers for both top and bottom part of the cavity. Al was used as the mirror and electrode materials for both top and bottom parts. Polyimide was used as the sacrificial material to form the cavity. The device is still under test to measure its performance.

TABLE OF CONTENTS

ACKNOWLEDGEMENTS... iv

ABSTRACT vi

LIST OF ILLUSTRATIONS.. xiii

LIST OF TABLES.. xvii

Chapter

1. INTRODUCTION……… 1

  1.1 Infrared Radiation…. 1

    1.1.1 Blackbody Radiation.. 1

    1.1.2 Application of Infrared Radiation... 2

  1.2 Infrared Detectors….. 3

    1.2.1 Photon Detector………………………………………….. .. 3

    1.2.2 Thermal Detector…………………………………………… 4

  1.3 Bolometer………………………………….. 5

    1.3.1 Noise Sources in Bolometers………………………………… 7

    1.3.2 Bolometer Figures of Merits…..……………………………….. 9

      1.3.2.1 Spectral Response…………………………….... 9

      1.3.2.2 Temperature Coefficient of Resistance (TCR)……………………………. 9

      1.3.2.3 Responsivity…………………………….……… 10

1.3.2.4 Detectivity……………………………………… 10

1.3.2.5 Noise Equipment Power (NEP)………………...... 10

1.3.2.6 Noise Equivalent Temperature Difference (NETD)…………..………………….. 11

1.4 Conclusions……….. 11

2. Si_xGe_{1-x} AND $Si_xGe_{1-x}O_y$ THIN FILMS FOR INFRARED SENSING MATERIAL.. 12

2.1 Sensing Materials for Microbolometers 12

2.2 Experimental Details…………………………………………………… 13

2.2.1 Deposition 13

2.2.2 Characterization.. 14

2.3 Results and Discussions.. 19

2.4 Conclusions……….. 38

3. DOPED Si_xGe_{1-x} MICROBOLOMETER 39

3.1 Introduction……….. 39

3.2 Bolometer Fabrication 39

3.3 Bolometer Characterization and Discussions 44

3.4 Conclusions……….. 52

4. FORMING GAS PASSIVATION OF $Si_xGe_{1-x}O_y$ MICROBOLOMETERS 53

4.1 Introduction……….. 53

4.2 Experimental Details… 57

4.2.1 Bolometer Fabrication 57

4.2.2 Noise Measurement 60

4.2.3 Forming Gas Passivation 61

4.2.4 Crystallinity and Atomic Composition Test 62

4.2.5 Noise Data Analysis……………………………………….. 64

4.3 Results and Discussions.. 64

4.4 Conclusions…………... 72

5. HIGH RESPONSIVITY a-$Si_xGe_{1-x}O_y$:H MICROBOLOMETER………... 73

5.1 Introduction……….. 73

5.2 Experimental Details 73

5.2.1 Bolometer Fabrication 73

5.2.2 Bolometer Characterization 76

5.3 Results and discussions………... 77

5.4 Challenges Faced in Fabricating Microbolmeters………….. 89

5.4 Conclusions……….. 90

6. FABRICATION AND CHARACTERIZATION OF CAVITY BASED FABRY-PEROT MICROSPECTROMETER……………….. 91

6.1 Introduction……….. 91

6.2 Device Fabrication……….. 92

6.3 Conclusions……..…….. 99

7. SUMMARY AND CONCLUSIONS……………….. 100

7.1 Si_xGe_{1-x} and $Si_xGe_{1-x}O_y$ Thin Films
For Infrared Sensing Material Introduction………….......................... 100

7.2 Doped Si_xGe_{1-x} Microbolometer………... 101

7.3 Forming Gas Passivation of
$Si_xGe_{1-x}O_y$ Microbolometers ……….………................................... 101

7.4 Fabrication and Characterization
of a-$Si_xGe_{1-X}O_y$:H Microbolometers……….………......................... 101

7.5 Fabrication of Cavity Based
Fabry-Perot Microspectrometer……….………................................. 102

REFERENCES 103

BIOGRAPHICAL INFORMATION... 111

LIST OF ILLUSTRATIONS

Figure Page

1.1 Cross section of a bolometer 5

2.1 Devices mounted on a package 14

2.2 Spectrum of EDX analysis to determine
the atomic composition of a sample by SEM 15

2.3 Cryostat with ZnSe window to characterize the device 16

2.4 Noise measurement setup for thin films 18

2.5 Reflectance and transmittance
measurement setup for thin films 20

2.6 X-ray diffraction from a sample
with $Si_{0.125}Ge_{0.8365}O_{0.039}$ 22

2.7 Plot of Ln (R) versus $1/k_BT$ for
sample with $Si_{0.099}Ge_{0.871}O_{0.031}$ 23

2.8 Variations of activation energy and
TCR with silicon concentration 24

2.9 Variations of activation energy
with oxygen concentration in $Si_xGe_{1-x}O_y$ 26

2.10 Variations of TCR with
oxygen concentration in $Si_xGe_{1-x}O_y$ 27

2.11 Voltage PSD for 1/*f*-noise for devices
$Si_{0.15}Ge_{0.85}$, $Si_{0.088}Ge_{0.76}O_{0.031}$ and $Si_{0\cdot 118}Ge_{0.847}O_{0.034}$ 29

2.12 Transmission through $Si_{0.15}Ge_{0.85}O_y$ thin
films with varying oxygen concentration
and 15% silicon concentration 30

2.13 Reflection through $Si_{0.15}Ge_{0.85}O_y$ thin films with varying oxygen concentration and 15% silicon concentration 31

2.14 Transmission through cover glass substrate 33

2.15 Transmission and reflection through $Si_{0.15}Ge_{0.85}$ thin film 34

2.16 Determination of optical bandgap energy of $Si_xGe_{1-x}O_y$ thin film from transmission and reflection data 35

2.17 Optical bandgap energies of $Si_xGe_{1-x}O_y$ thin films 36

3.1 Figure 3.1 Doped a-$Si_{0.15}Ge_{0.85}$ bolometer fabrication steps: schematic (left) and optical microscope picture (right) after (a) SiN deposition and Al pattern (b) polyimide cure (c) Ti arm pattern (d) Au contact and bond pad pattern (e) a-$Si_{0.15}Ge_{0.85}$ and Au lift off (f) polyimide ash…………40

3.2 (a) SEM micrograph of suspended $60 \times 60\ \mu m^2$ detectors array (b) Closer view of an individual $60 \times 60\ \mu m^2$ detector 43

3.3 Dependence of TCR and resistance on temperature for device 10C52 46

3.4 *I –V* characteristics of 10C52 in air 47

3.5 *I-V* characteristics of different metal and doped n-$Si_{0.15}Ge_{0.85}$ contacts 49

3.6 *I-V* characteristics of device 10C52 for determining G_{th} by Joule heating method 50

3.7 Noise voltage PSD of device 10C52 at different bias currents 51

4.1 a) Cross sectional area of a $Si_xGe_{1-x}O_y$ Microbolometer (b) SEM micrograph of $60 \times 60\ \mu m^2$ microbolometer array 54

4.2 SEM micrograph of warped microbolometer arrays without silicon nitride sandwich layer 55

4.3 Schematic for noise measurement setup 56

4.4 X-ray diffraction from $Si_{0.11758}Ge_{0.87}O_{0.0125}$ annealed for 8 hours at 250 ^{o}C in forming gas 63

4.5 Noise voltage PSD of device SLB1 at different interval of passivation time for 0.3 μA bias current 67

5.1 Cross section of a-$Si_{0.15}Ge_{0.85}O_{0.0236}$:H microbolometer with (a) Ni Contact (b) NiCr contact 74

5.2 SEM micrograph of suspended 40×40 μm^2 microbolometers arrays after surface micromachining (a) 10 × 10 array of microbolometers (b) closer view of microbolometers 75

5.3 Variations of resistance and TCR at different temperature for 21B1b 80

5.4 *I-V* characteristic from device 19C1a 81

5.5 Determination of thermal conductivity by Joule heating method 82

5.6 Variations of responsivity and detectivity at different chopper frequencies for device 21B1b with 2.5 μm long pass filter placed in front of the device. 83

5.7 Noise voltage PSD of device 21B1b with signal modulated at 9 Hz 84

5.8 Variations of responsivity and detectivity at different chopper frequencies for device 21B1b 85

5.9 Curled sandwich structure detector's array after ten hours of ashing. Partially etched bond pads are seen clearly (a) SEM picture (b) optical microscope picture 88

6.1 Cross section of a cavity based Fabry-Perot microspectrometer 92

6.2 Figure 6.2 Microscopic view of microspectrometer at the end of different fabrication steps (a) after bottom electrode patterning (a) after bottom electrode patterning (b) after bottom mirror patterning (c) after sacrificial polyimide patterning (d) after top electrode patterning (e) after top mirror patterning (f) after top Al_2O_3 electrode patterning (g) after backside Al etching (h) after bulk micromachining (picture was taken from back side of the wafer, the bottom of Al layer can be seen through hole) 93

6.3 Completed microspectrometer after ashing (a) SEM picture (b) optical microscope picture 94

LIST OF TABLES

Table Page

2.1 Properties $Si_xGe_{1-x}O_y$ Thin Films 25

4.1 Variation of Noise Parameters in Different Devices with Different Passivation Time 68

5.1 Measured Figures of Merits of Different $Si_xGe_{1-x}O_y$ Microbolometers 86

CHAPTER 1

INTRODUCTION

1.1 Infrared Radiation

Infrared (IR) radiation extends from 0.75 to 1,000 µm wavelengths and lies in between visible light and microwave signals. IR band can be classified into five sub regions. These are: near IR (NIR) that ranges from 0.75 to 1.4 µm, short wavelength IR (SWIR) that ranges from 1.4 to 3 µm, mid wavelength IR (MWIR) which ranges from 3 to 8 µm, long wavelength IR (LWIR) that ranges from 8 to 15 µm, and far wavelength IR (FWIR) which extends from 15 to 1,000 µm.

1.1.1 Blackbody Radiation

Every object whose temperature is more than absolute zero, radiates IR radiation. A black body is considered as a perfect absorber and perfect radiator. Plank's law mentioned in (1.1) expresses the amount of energy radiated by a blackbody at a temperature T and wavelength λ.

$$M_{e,\lambda}(\lambda,T) = \frac{2\pi hc^2}{\lambda^5[e^{hc/\lambda k_B T} - 1]} \tag{1.1}$$

Here, M is known as spectral radiant exitance in W/(cm^2- µm),

h is the Plank's constant,

c is the speed of light in the propagation medium,

k_B is the Boltzmann's constant, $k_B = 1.38\times10^{-23}$ J/K.

Real life objects (other than blackbody) exhibit the absorption and radiation differently from a blackbody. Typically peak exitance occurs for this case is much less than that of a blackbody source. Peak exitance from a black body occurs at 9.7 μm at 25 ^{o}C.

1.1.2 Applications of Infrared Radiation

IR radiation has a wide range of applications. IR radiation is used in night vision cameras to see an object. Difference of temperature is detected from the radiation of objects and that turns into an image. IR radiation is used by firefighters in smoky environment to see because IR is transparent in smoky environment. IR radiation is used to detect and record thermal pattern of a body by implementing thermal imager which is defined as thermography. Thermography is widely used in law enforcement, search and rescue in toxic or smoke filled environment, and medical imaging. It is also used in industry for quality and condition assurance and maintenance (for example, by monitoring the temperature of perishable food items like meat). Thermography is used in forensic investigations of electrical, mechanical, and structural systems. IR radiation is used to remove ice from aircraft and heating asphalt pavements during new construction, or in repair of damaged asphalt. In industrial processing it can be used to observe hot spots and micro-cracks and monitor machines and processes for proper temperature. Fourier transform infrared spectroscopy (FTIR) is used to determine the atomic composition and structure of a material. IR data transmission is used to communicate with computer peripherals. Usually, remote controls use the IR to command appliances. Scanning radiometers in weather satellites are used to produce thermal images which can enable an analyst to determine cloud heights and types, to calculate land and surface water temperatures, and to locate ocean surface features. IR radiation is widely used in surveillance systems.

1.2 Infrared Detectors

Infrared detectors are the photo detectors which responses to the infrared radiation. Different infrared detectors operate in different regions of infrared spectrum. They convert the incident infrared light flux to a measurable electrical quantity like voltage, resistance, inductance or capacitance as the output. There are two types of infrared detectors. One is photon detector and the other is thermal detector.

1.2.1 Photon Detector

In a photon detector, the photons are converted into electron hole pairs provided that the photon has the energy equal or greater than the band gap energy of the material, E_g. Mathematically we can write

$$h\nu \geq E_g \tag{1.2}$$

Here, ν is the optical frequency of the photon in cycles/s.

ν can be related with speed and wavelength of light as mentioned in (1.3). The lowest energy photon can be detected at the wavelength λ_c is expressed by (1.3).

$$E_g = \frac{hc}{\lambda_c} \tag{1.3}$$

Substituting the values of constant in (1.3), we obtain (1.4)

$$\lambda_c(\mu m) = \frac{1.238}{E_g(eV)} \tag{1.4}$$

So for photon detectors, the cutoff wavelength is determined by energy gap of the material. For materials having smaller energy gap, electrons are thermally excited into the conduction band, which in turn produces non desirable dark current. The dark current as well as shot noise associated with dark current generated electrons can be prevented by cooling the detectors cryogenically. This cooling scheme made photon detectors expensive. Photoconductive, photovoltaic, photoemissive are the examples of photon detectors. HgCdTe, Si, PbS, GaAs, InSb, PbSe, Ge are some of the popular materials used for photon detectors.

1.2.2 Thermal Detector

For thermal detectors, the absorbed radiation causes the detector temperature to change. This temperature rise causes change in some of the measurable electrical quantities like resistance, voltage, capacitance, inductance etc. So, the absorption of heat energy is very important in case of a thermal detector to have distinct change in electrical quantities to be measured. Thermal detectors are usually slow in response as their thermal mass must experience a rise and fall in temperature. Thermal detectors usually run at room temperature which made them inexpensive as compared to photon detectors. The spectral response of thermal detectors is broader than that of photon detectors. Bolometers, thermocouples, pyroelectric detectors are the examples of thermal detectors.

1.3 Bolometer

Bolometers are thermal detectors whose resistance changes with temperature. The effect is that of change in resistance of a material to the heating effect of the incident radiation.

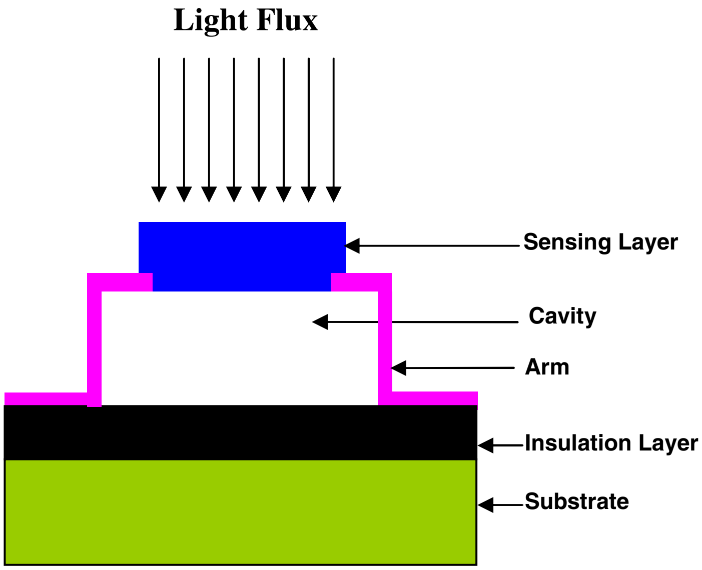

Figure 1.1 Cross section of a bolometer

The rate of heat transfer is an important factor in determining the speed of thermal detection process. Reduced thermal mass of the bolometer will result in heating up the sensing layer faster. Figure 1.1 shows the cross section of a microbolometer. The separation of sensing material from the substrate will reduce both the thermal mass and heat loss. Once the detector element is heated above the ambient, the temperature gradient serves as the driving force for heat flow. Conduction and radiation are the main heat flow mechanisms in thermal detectors. Of these, conduction dominates. Paths of heat loss through conduction depend on the device geometry and typically are the metal arms linking the detector pixel to the bond pads. For the general case of a dc biased bolometer exposed to a modulated light source, the heat balance expression can be written by (1.5)

$$C_{th}\frac{dT}{dt} = \eta P_{signal} + I_b^2 R(T) - 2\varepsilon A_d \sigma (T^4 - T_0^4) - G_{th}(T - T_0) \qquad (1.5)$$

where, C_{th} is the thermal mass or heat capacity (JK^{-1}), $\frac{dT}{dt}$ is the rate of change of temperature of the detector, η is the optical absorption efficiency of the detector, P_{signal} is the incident optical signal power (W), I_b is the bias current (A), R is the temperature dependent device resistance (Ω), ε is the detector emissivity (assumed equal to absorptivity at all wavelengths), A_d is the detector area (cm^2), σ is the Stefan-Boltzmann constant (5.67x10^{-12} W/cm^{2}K^4), T_0 is the temperature of the heat sink (K), G_{th} is the thermal conductance of the detector (WK^{-1}). (1.5) can be simplified to (1.6)

$$C_{th}\frac{d\Delta T}{dt} + (G_{th} + G_{rad} - \alpha P_I)\Delta T = \eta P_{signal} + P_I \qquad (1.6)$$

where, $G_{rad} = 8\varepsilon A_d \sigma T_0^3$,. is the radiative conductance of the material and α is the temperature coefficient of resistant (TCR) and is defined as normalized rate of change of the detector resistance and P_I is the heating effect of the incident radiation. Substituting the value of the effective conductance of the material, $G_{eff} = G_{th} + G_{rad} - \alpha P_I$, in (1.6)

$$C_{th}\frac{d\Delta T}{dt} + G_{eff}\Delta T = \eta P_{signal} + P_I \qquad (1.7)$$

1.3.1 Noise Sources in Bolometers

Noise limits set the lower level of sensitivity of detector. Bolometer's performance is degraded mainly by six possible noise sources internal to it [1]. These are Johnson noise, shot noise, generation recombination (g-r) noise, one over frequency noise (1/*f*), temperature fluctuation noise, and background noise. The bolometer's figures of merits are limited by the noise behavior of the bolometer [2] and 1/*f*-noise is the major limiting factor in the performance of a microbolometer. The most dominant source of noise in bolometers is 1/*f*-noise [3].

1/*f*-noise can be expressed by Hooge's formula [4]

$$V^2_{1/f} = \int S^{\Delta f}{}_v df = \int \frac{\alpha_H V_b^2}{fN} df \tag{1.8}$$

where, f is the electrical frequency, α_H is the Hooge coefficient, N is the number of fluctuators in the sample, V_b is the bias voltage, and S_v is the voltage noise power spectral density. 1/*f*-noise also can be expressed as [3]

$$V_{1/f} = KV_b\sqrt{\frac{\rho}{WLtf}} \tag{1.9}$$

Here, K is a constant which depends on the type of material, ρ is the resistivity of the material, W, L, and t are the width, length and thickness of the active part of bolometer. Origin of 1/*f*-noise is still a controversial issue. As can be seen from (1.9) that, among other factors 1/*f*-noise is dependent on the geometry, property and deposition condition of the material. 1/*f*-noise usually exists at low frequencies. It has a slope of 1/*f* and hence it is called 1/*f*-noise.

Johnson noise is caused by the random thermal motion of charge carriers in a resistive element and is not affected by the direct current flow in the circuit. Local random thermal motion of carriers sets up fluctuating charge gradients even though charge neutrality exists generally across a resistor. Mathematically it is given by

$$V_j = \sqrt{4k_B TR\Delta f} \tag{1.10}$$

where, *R* is the resistance of the device, *T* is the temperature of the detector, and *Δf* is the frequency bandwidth over which the noise is measured. As can be seen, every resistor with a finite resistance value shows Johnson noise above absolute temperature. Johnson noise is visible at the higher frequencies, and has flat shape in frequency spectrum.

The temperature fluctuation noise is noise due to the heat conduction of isolated thermal detector with the substrate and is a function of the thermal conductance. Mathematically, it is given by [5]

$$V_{TF} = \frac{2I_b R\alpha T\sqrt{\Delta f k_B}}{\sqrt{G_{th}(1+\omega^2\tau_{th}^2)}} \tag{1.11}$$

where, ω is the modular frequency of the incident IR radiation, and τ_{th} is the thermal time constant of the bolometer and is defined as

$$\tau_{th} = \frac{G_{th}}{C_{th}} \tag{1.12}$$

The background noise is the noise associated with random fluctuations in the radiative exchange with the detector. For a detector surrounded by a blackbody at temperature T_B, it is expressed as [5]

$$V_{BG} = \frac{I_b R \alpha \sqrt{8 A_d \eta \sigma k_B (T^5 + T_B^5) \Delta f}}{G_{th} \sqrt{(1+\omega^2 \tau_{th}^2)}} \tag{1.13}$$

The generation and recombination noise (V_{g-r}) is occurred due to the generation and recombination of carriers. The shot noise (V_{shot}) is present when there exists a non-Ohmic metal-semiconductor contact like in diode.

The total noise, V_n, in a bolometer is the summation of all the individual noise sources and is given by

$$V_n = \sqrt{V_{1/f} + V_j + V_{BG} + V_{TF} + V_{g-r} + V_{shot}} \tag{1.14}$$

1.3.2 Bolometer Figures of Merits

1.3.2.1 Spectral Response

It describes in a relative sense the manner by which a bolometer changes its output signal in response to changes in wavelength of the input signal. Photon detectors ideally exhibits a relative response per unit radiant power per unit wavelength interval which rises linearly with increasing wavelength, peaks, and then drops off sharply to zero. This is because their response is generally proportional to photon arrival rate for energies greater than the semiconductor absorption edge. On the other hand, thermal detectors, which respond to the radiant power rather than the photon rate, exhibit ideally a spectral response to unit radiant power per unit wavelength interval which is wavelength independent.

1.3.2.2 Temperature Coefficient of Resistance (TCR)

TCR is expressed as

$$\alpha = \frac{1}{R}.\frac{dR}{dT} \tag{1.15}$$

TCR is a material property.

1.3.2.3 Responsivity

Responsivity is a measure of the dependence of the signal output of a detector upon the input radiant power. The detector output signal may be current or voltage. Thus the voltage responsivity, R_v, is defined as the detector output voltage per unit of detector input power.

$$R_v = \frac{\eta \alpha R I_b}{G_{th}(1+\omega^2\tau^2)^{1/2}} \tag{1.16}$$

Voltage responsivity is expressed in V/W while current responsivity is expressed in A/W.

1.3.2.4 Detectivity

Detectivity, D^* is the area normalized signal to noise ratio. It has the unit of cmHz$^{1/2}$/Watt. The Detectivity can be expressed by

$$D^* = \frac{R_v\sqrt{A_d \Delta f}}{\Delta v_n} \tag{1.17}$$

where, Δv_n is the total noise voltage observed in the electrical bandwidth Δf .

1.3.1.5 Noise Equivalent Power (NEP)

The NEP is the rms incident power necessary to produce a signal-to noise ratio of unity. The units of NEP are Watts. NEP is related to the detectivity by the following equation

$$NEP = \frac{(A_d \Delta f)^{1/2}}{D^*} \tag{1.18}$$

1.3.2.6 Noise Equivalent Temperature Difference (NETD)

NETD is defined as the change in temperature of an extended area blackbody imaged upon a focal plane array, which gives rise to a change in signal to noise ratio of unity in the output of the electronics. This is a figure of merit for a complete camera, which takes into account the optics, focal plane array performance, and read-out electronics. It can be expressed by (1.19).

$$NETD = \frac{4F^2}{\tau_0 D^* \sqrt{A_d} (\Delta P / \Delta T)_{\lambda_1 - \lambda_2}} \tag{1.19}$$

Here, F is the f/number of optics, τ_0 is the transmittance of the optics, and $(\Delta P / \Delta T)_{\lambda_1 - \lambda_2}$ is the derivative with respect to temperature of the power radiated by a blackbody at room temperature within the spectral interval between wavelengths λ_1 and λ_2. Most thermal imaging systems operate either in the 3-5 µm atmospheric window or through 8-14 µm atmospheric window, where $(\Delta P / \Delta T)_{\lambda_1 - \lambda_2}$ can be shown to equal to 2×10^{-5} W/cm^{2}K and 2.6×10^{-4} W/cm^{2}K, respectively.

1.4 Conclusions

This Chapter discussed introduction to infrared and infrared detectors. It also discussed working principles of bolometer and different noise sources associated with bolometer. It also discussed different figures of merits for bolometers.

CHAPTER 2

Si_xGe_{1-x} AND $Si_xGe_{1-x}O_y$ THIN FILMS FOR INFRARED SENSING MATERIAL

2.1 Sensing Materials for Microbolometers

A bolometer can be made of any material which exhibits a temperature dependent change of resistance. However, the sensing material to be used in the bolometer must have the following properties

a. Capable of absorbing the infrared radiation.

b. Have high TCR, so a small change in temperature would result for significant change in the bolometer resistance.

c. Have moderate resistivity

d. Have low $\frac{1}{f}$ noise.

Moreover, in order to integrate the detector with the read out circuitry, it is preferred that the thermister be a conventional semiconductor so its processing is fully compatible with conventional post-CMOS silicon micromachining technology.

Common materials used as the thermister in microbolometers include the semiconducting phase of Y-Ba-Cu-O [6], poly-Si [7], poly-SiGe alloys [8], VO_x [9], metal resistors such as Ti [10], Nb [11], Pt [12], amorphous Si and Ge [13] and amorphous Si-Ge alloys [14]. Silicon and germanium alloys are a good choice for the thermometer because they are conventional semiconductors and their processing can be fully compatible with post-CMOS micromachining technology. The semiconducting phase of Y-Ba-Cu-O has a high TCR of -3.1 %/K but this is not a conventional semiconductor. Dobrzanski et al. [7] and Sedky et al. [8] used poly-Si and poly-SiGe alloys respectively to have a TCR of around -2.5 to -3 %/K, but they require a deposition temperature of 650 ^{o}C to achieve the desired crystallinity by chemical vapor deposition (CVD) technique. VO_x is widely accepted as sensing material because of its relatively low 1/*f*-noise (23.39 nV/Hz$^{1/2}$ at a bias current of 19.3 μA at 5 Hz) [15] and high IR absorption (η=0.8) [16]. VO_x has a TCR value of around -1.86 %/K but it requires a post-deposition annealing at 500 ^{o}C. It is also not a conventional semiconductor. Metal resistors have very low 1/*f*-noise but their TCR is also low which results in a low responsivity as well as detectivity. Amorphous Si and Ge display a TCR of -2.6 %/K. Iborra et al. [17] obtained the TCR of -4.21 %/K from $Ge_xSi_{1-x}O_y$.

2.2 Experimental Details

This section describes the deposition and characterization techniques of Si_xGe_{1-x} and $Si_xGe_{1-x}O_y$ thin films.

2.2.1 Deposition

Thin films of Si_xGe_{1-x} and $Si_xGe_{1-x}O_y$ were deposited by RF magnetron sputtering from a single 3-inch diameter target in an Ar or Ar : O_2 environment. The target was prepared by bonding pieces of a Si wafer to a Ge sputter target with the area occupied by the Si pieces determining the Si concentration. A turbo pump evacuated the chamber to a base pressure of 3×10^{-6} Torr before sputtering. Sputtering was performed at 10 mTorr pressure onto 25 mm square glass substrates. A RF power of 160 watts was used to sputter the films.

2.2.2 Characterization

A section of the glass substrate was mounted on a ceramic package for electrical characterization. Figure 2.1 shows the devices mounted on a package for characterization. Gold wires were attached to the sample by indium bonding.

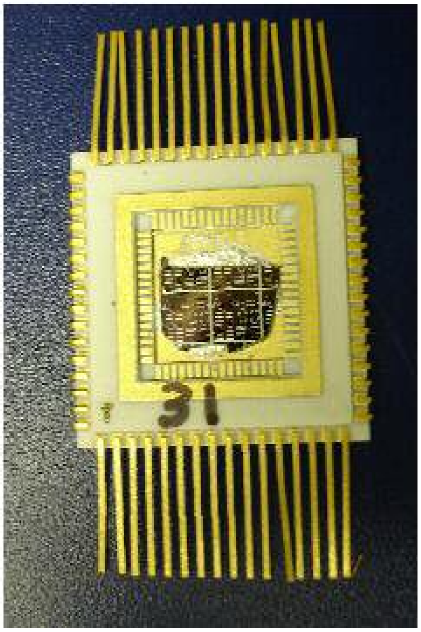

Figure 2.1 Devices mounted on a package

The film thickness was measured from steps on the deposited films by a Mahr Perthometer M1 profilometer. The film composition was measured by Energy–Dispersive X-ray analysis (EDX) in a JOEL JSM-I6845 scanning electron microscope (SEM). An accelerating voltage of 19 keV was applied to determine the standard peaks as well as the concentration of each constituent element in the sample. Figure 2.2 shows the spectrum for EDX analysis from a sample. A Siemens model D500 θ-2θ

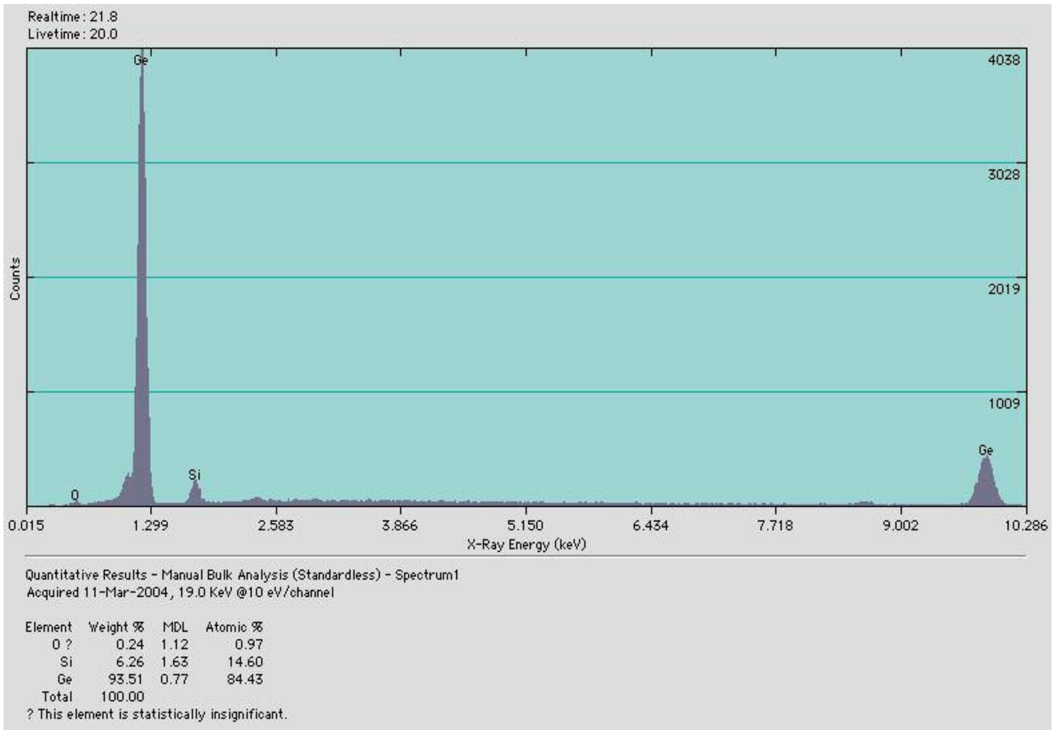

```
Realtime : 21.8
Livetime : 20.0
```

```
Quantitative Results - Manual Bulk Analysis (Standardless) - Spectrum1
Acquired 11-Mar-2004, 19.0 KeV @10 eV/channel

Element   Weight %   MDL    Atomic %
    O ?       0.24   1.12       0.97
     Si       6.26   1.63      14.60
     Ge      93.51   0.77      84.43
  Total     100.00
? This element is statistically insignificant.
```

Figure 2.2 Spectrum of EDX analysis to determine the atomic composition of a sample by SEM

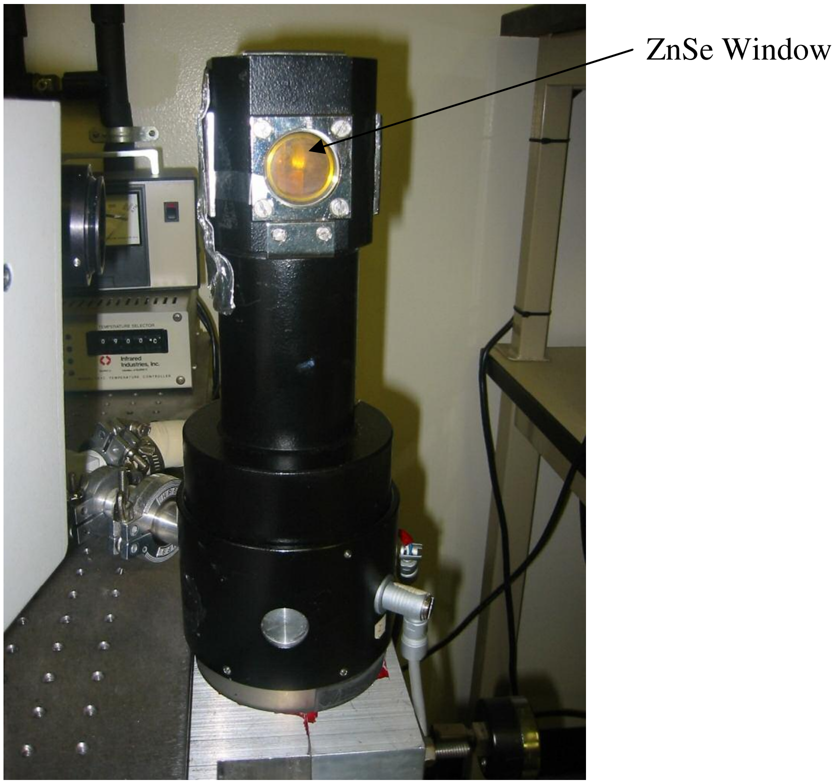

Figure 2.3 Cryostat with ZnSe window to characterize the device

diffractometer using Cu K α radiation was used to measure the X-ray Diffraction (XRD) for all the samples. The 2θ angle was varied from 2° to 120°.

The resistance versus temperature (R-T) characteristics was measured in a Leybold ROK 10-300 K closed-cycle cryostat refrigerator evacuated to 50 mTorr and TCR was calculated by numerically differentiating the R-T characteristic. The temperature inside the cryostat was varied from 200 K to 325 K by a LakeShore DRC-91C temperature controller. The resistance of each film composition was measured by two wire resistance measurement method. The value of the resistance at 298 K from the R-T data was used to calculate the resistivity. Figure 2.3 shows the cryostat with ZnSe window.

The electrical noise was measured in each device by voltage biasing the device and measuring the noise current through the use of a 10 kΩ series resistor. The device resistance was much larger than the 10 kΩ series resistance providing a good voltage bias. A Stanford Research Instruments model SR560 amplifier using a gain of 750 amplified the voltage across the resistor. The amplified noise signal was measured with a Hewlet-Packard HP 3562A signal analyzer. The noise power spectral density was recorded over the frequency range of 1 Hz to 100 kHz. In this manner, a voltage noise power spectral density was recorded that was a combination of the Johnson noise voltage from 10 kΩ series resistor and the 1/*f*-noise current from the $Si_xGe_{1-x}O_y$ thin film device. Each device was biased at three different bias currents and the average value of noise voltage power spectral density at 10 Hz was used to calculate the

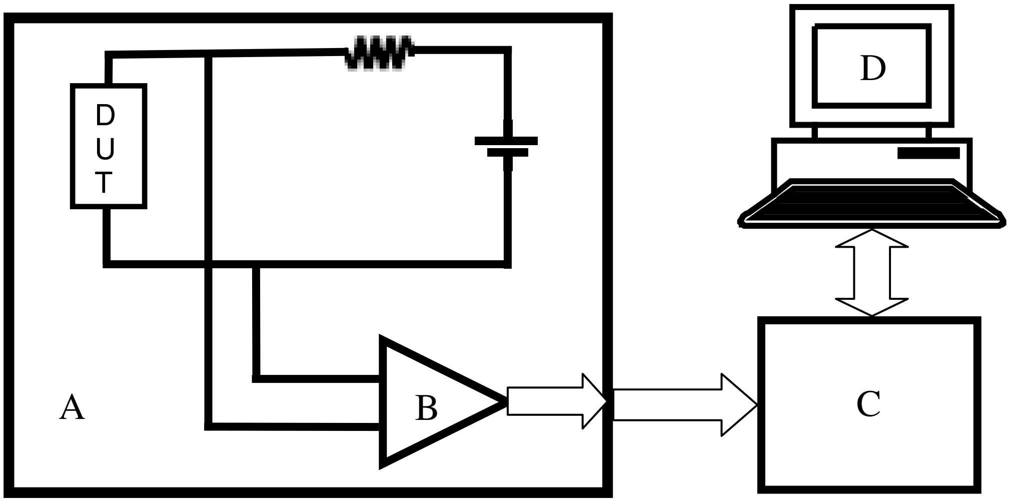

A Electromagnetically Shielded Room
B Low Noise Pre-Amplifier SRS 570
C HP 3562 Dynamic Signal Analyzer
D Computer

Figure 2.4 Noise measurement setup for thin films normalized Hoogie coefficient for 1/*f*-noise (K_f). The devices were placed in a low-frequency electromagnetically shielded room to minimize the influence of extraneous noise signals. Figure 2.4 shows the noise measurement setup.

The optical transmission and reflection characteristics of the thin films were measured to determine the optical bandgap. The characteristics were measured using an Oriel 60071 light source housing a 6575-IR ceramic element and a 60077 ZnSe condenser/collimator. The radiating element can be modeled as 1450 K blackbody source. Narrow-band spectral analysis was performed with an Oriel MS-257 monochromator/spectrograph. The net usable range of this system was 0.6-15 µm. An Oriel 70124 pyroelectric detector used to detect the transmitted or reflected signal through the samples. The IR source was chopped at a frequency of 70 Hz. A Hewlet-Packard HP 3562A signal analyzer was used to analyze the response obtained from pyroelectric detector through the samples. The signal analyzer simultaneously measured the signal amplitude and noise as the wavelength was varied from 600 nm to 3000 nm. Figure 2.5 shows the transmittance, reflectance measurement set up.

2.3 Results and Discussions

XRD from a sample with $Si_{0.125}Ge_{0.8365}O_{0.039}$ is shown in Figure 2.6. As with this sample, no sharp peaks were observed form any samples, which suggested that the films of Si_xGe_{1-x} and $Si_xGe_{1-x}O_y$ are amorphous.

To observe the effect of combining Si with the Ge, three different targets with compositions of $Si_{0.15}Ge_{0.85}$, $Si_{0.30}Ge_{0.70}$, and $Si_{0.40}Ge_{0.60}$ were prepared and sputtered in

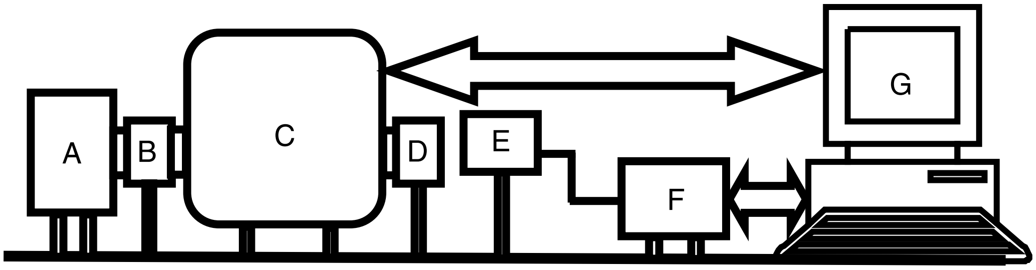

A Thermal Light Source
B Mechanical Chopper
C Monochromator
D Device
E Pyroelectric Detector
F HP 3562 Dynamic Signal Analyzer
G Computer

Figure 2.5 Reflectance and transmittance measurement setup for thin films an Ar environment. The activation energy is related with the resistance and temperature by the following equation

$$R(T) = R_0 e^{\frac{E_a}{k_B T}} \tag{2.1}$$

where, $R(T)$ is the resistance at temperature T, R_0 is the pre-exponential factor, and E_a is the activation energy. An Arrhenius plot of Ln (R) versus $1/k_BT$ and a straight line was obtained from that plot. Figure 2.7 shows the plot of Ln (R) versus $1/k_BT$ for sample $Si_{0.099}Ge_{0.871}O_{0.031}$. The small deviation from a straight line indicates a weaker temperature dependence of R_0. Figure 2.8 shows the variations of TCR, and activation energy while Si concentration was varied in $Si_{1-x}Ge_x$ thin films. It can be seen that the TCR first increased as the Si concentration was increased from 0 % to 15 % and then decreased for higher Si concentrations. Ahmed et al. [18] reported to have an increase in resistivity from approximately 8×10^2 Ω-cm to 2×10^3 Ω-cm while the Si concentration was increased from 15 % to 30 %. Measured resistances agree with this result. The addition of Si to Ge will decrease the mobility of the carriers resulting in the increase in resistivity.

The resistivity and thereby the TCR depend on the activation energy of the mobile carriers at a certain temperature. Later, we see that since the optical bandgap was found to decrease at higher Si concentrations in Si_xGe_{1-x}, the activation energy as well as the TCR is expected to decrease with increasing Si concentration. Ahmed et al. [18], however, found that the increase in TCR was only from -2 %/K to -2.05 %/K, which is small compared to the large increase in resistivity.

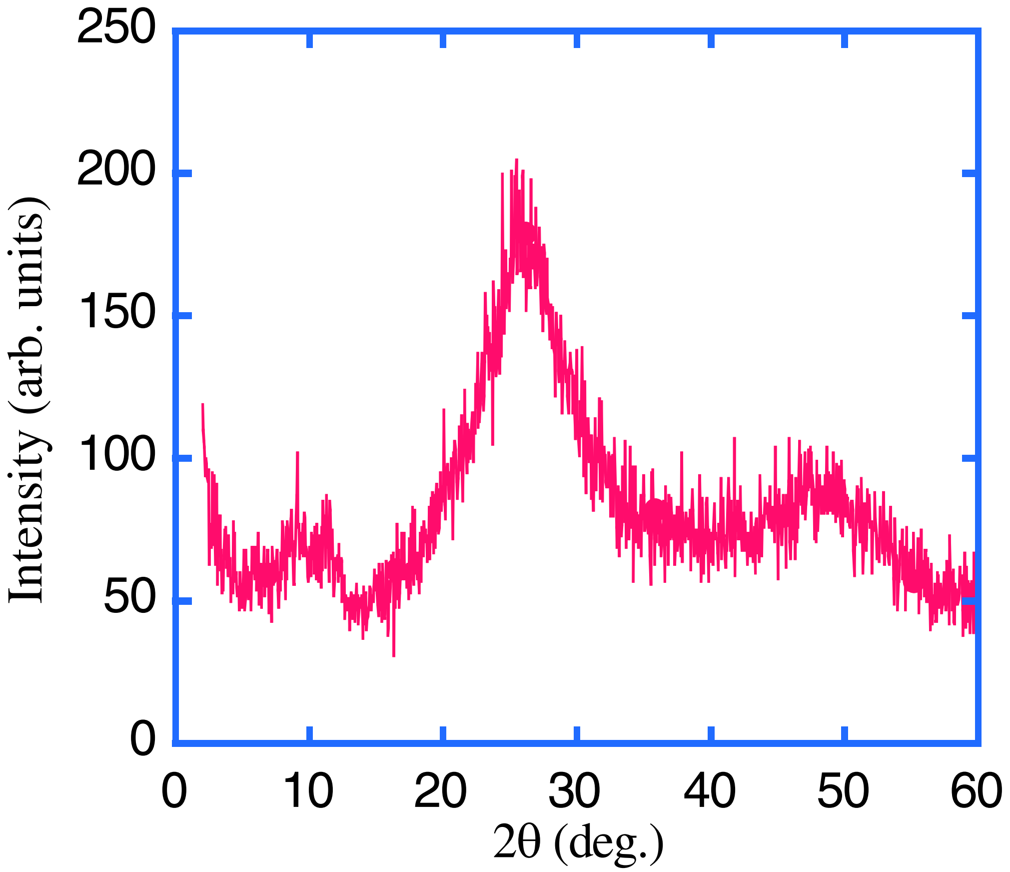

Figure 2.6 X-ray diffraction from a sample with $Si_{0.125}Ge_{0.8365}O_{0.039}$

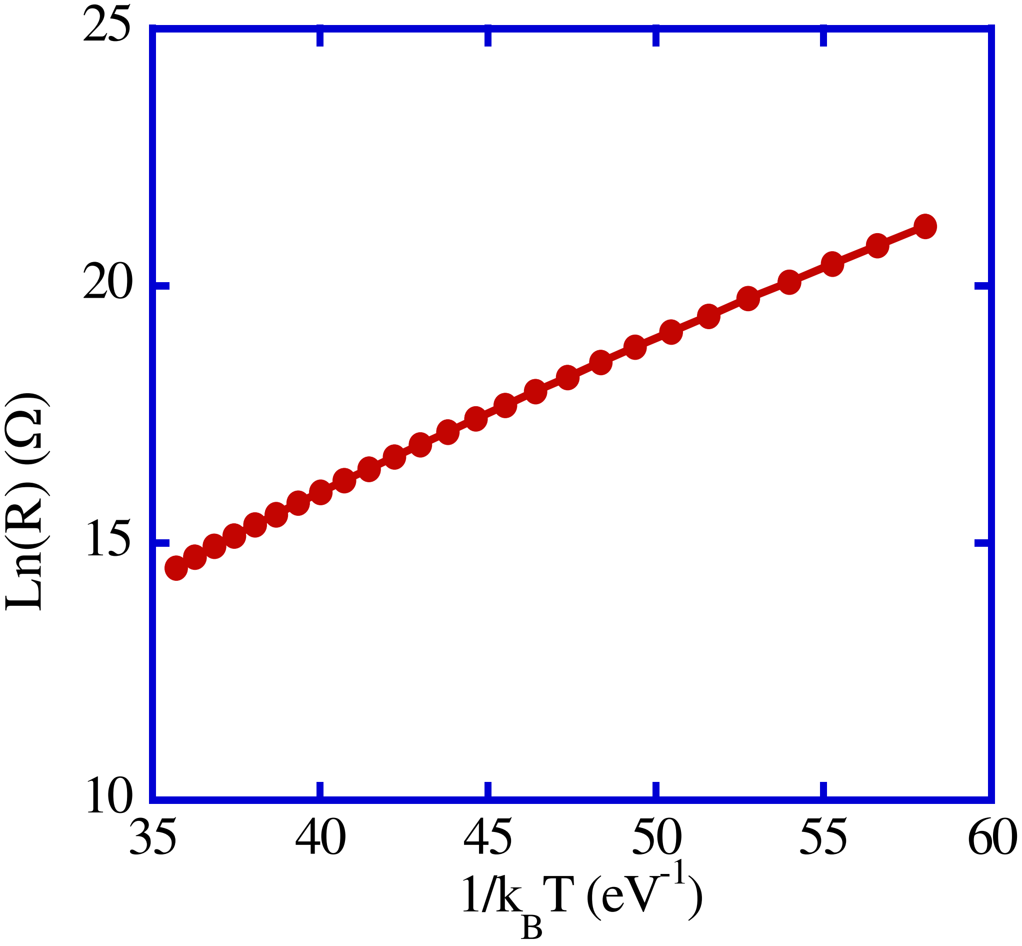

Figure 2.7 Plot of Ln (R) versus $1/k_BT$ for sample with $Si_{0.099}Ge_{0.871}O_{0.031}$

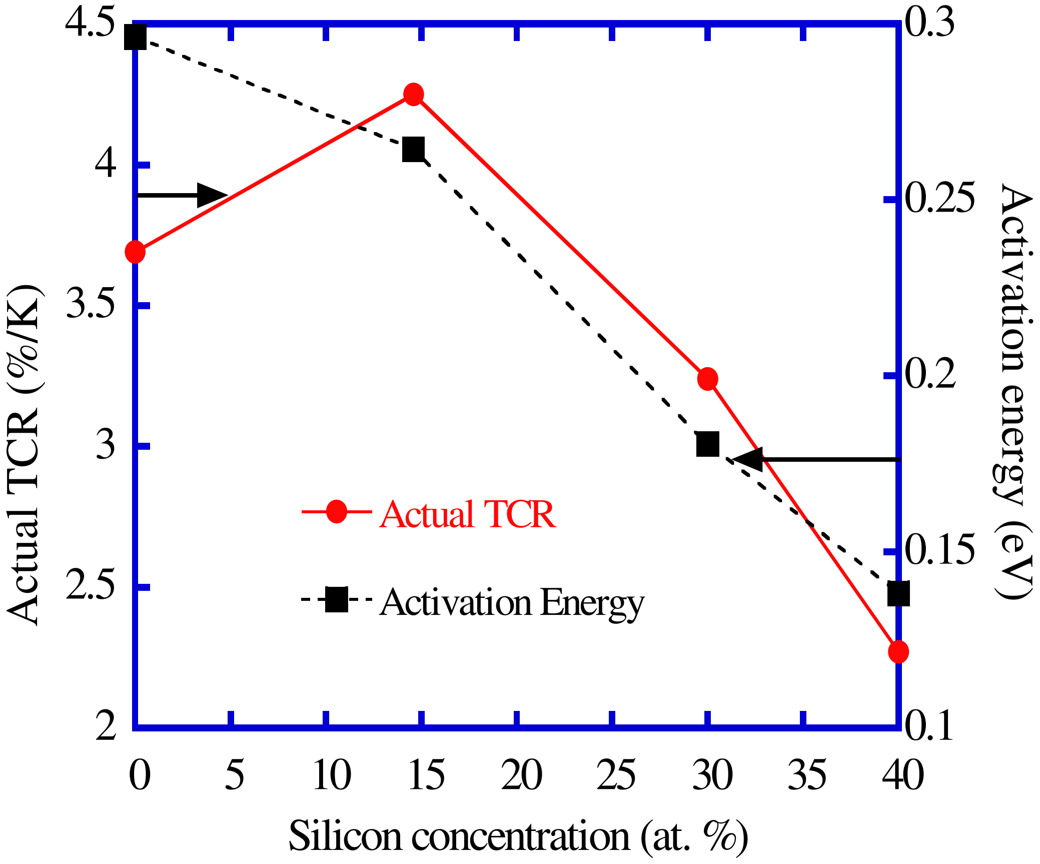

Figure 2.8 Variations of activation energy and TCR with silicon concentration

The effect of adding oxygen to the $Si_{1-x}Ge_x$ was investigated by sputtering from three different targets with composition $Si_{0.15}Ge_{0.85}$, $Si_{0.30}Ge_{0.70}$, and $Si_{0.40}Ge_{0.60}$ in a mixture of Ar and O_2 environment. The O_2 flow increased at fixed RF power and fixed Ar flow to increase the oxygen concentration in the deposited films. Figure 2.9 and Figure 2.10 shows the variations of activation energy and TCR with oxygen concentration in $Si_xGe_{1-x}O_y$ respectively. Later, it is shown that increasing the oxygen concentration in the $Si_xGe_{1-x}O_y$ also resulted in an increase in the optical bandgap. Clement et al. [19] found that the resistivity was varied from 2×10^3 Ω-cm to 5×10^3 Ω-cm when the oxygen content (y) in $Ge_xSi_{1-x}O_y$ was varied from 0.42 to 0.78. Similar resistivity values were obtained in this work.

Table 2.1 Properties of $Si_xGe_{1-x}O_y$ Thin Films

SAMPLE	Normalized Hooge parameter, K_f	TCR, α (%/K)	Activation Energy, E_a (eV)	Optical Bandgap, E_g (eV)
$Si_{0.15}Ge_{0.85}$	1.70×10^{-10}	-4.2	0.264	0.91
$Si_{0.099}Ge_{0.871}O_{0.031}$	4.3×10^{-11}	-4.4	0.297	0.80
$Si_{0.118}Ge_{0.847}O_{0.034}$	1.10×10^{-10}	-4.6	0.310	0.81
$Si_{0.125}Ge_{0.8365}O_{0.039}$	$< 2.58 \times 10^{-8*}$	-5.1	0.324	0.89
$Si_{0.114}Ge_{0.834}O_{0.052}$	$< 2.35 \times 10^{-6*}$	-5.7	0.368	0.89
$Si_{0.172}Ge_{0.736}O_{0.092}$	$< 4.06 \times 10^{-3*}$	-6.7	0.453	1.4
$Si_{0.294}Ge_{0.706}$	9.55×10^{-11}	-3.2	0.181	0.89
$Si_{0.269}Ge_{0.692}O_{0.039}$	3.12×10^{-8}	-3.5	0.191	0.75
$Si_{0.281}Ge_{0.628}O_{0.092}$	$< 4.17 \times 10^{-4*}$	-4.9	0.336	1.1
$Si_{0.269}Ge_{0.579}O_{0.152}$	$< 3.62 \times 10^{-4*}$	-7.3	0.577	1.2
$Si_{0.427}Ge_{0.573}$	$< 5.08 \times 10^{-10*}$	-2.3	0.138	0.89
$Si_{0.386}Ge_{0.599}O_{0.015}$	2.45×10^{-10}	-2.6	0.155	0.86
$Si_{0.425}Ge_{0.524}O_{0.052}$	$< 4.19 \times 10^{-9*}$	-3.4	0.222	0.86
$Si_{0.380}Ge_{0.525}O_{0.095}$	$< 3.36 \times 10^{-7*}$	-4.7	0.304	0.83
$Si_{0.411}Ge_{0.421}O_{0.168}$	$< 1.30 \times 10^{-4*}$	-8.7	0.658	0.87
Ge	2.07×10^{-10}	-3.7	0.296	0.96

*System limited noise

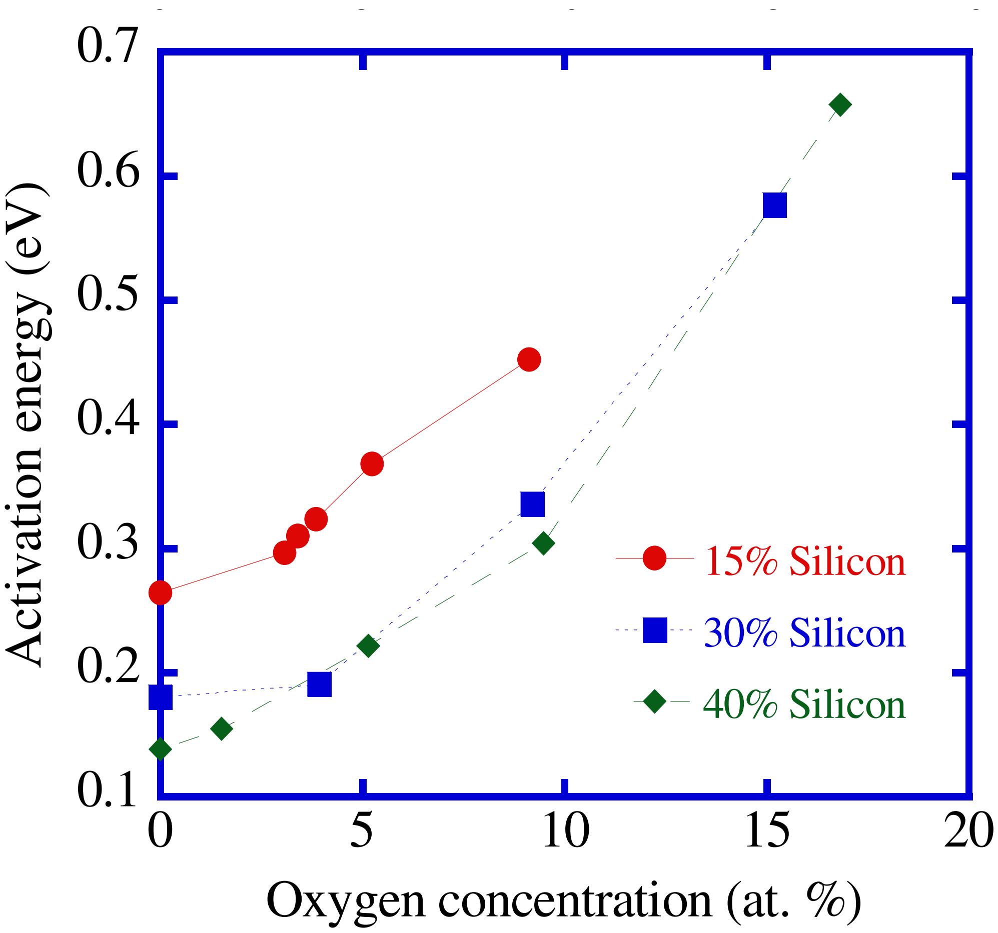

Figure 2.9 Variations of activation energy with oxygen concentration in $Si_xGe_{1-x}O_y$

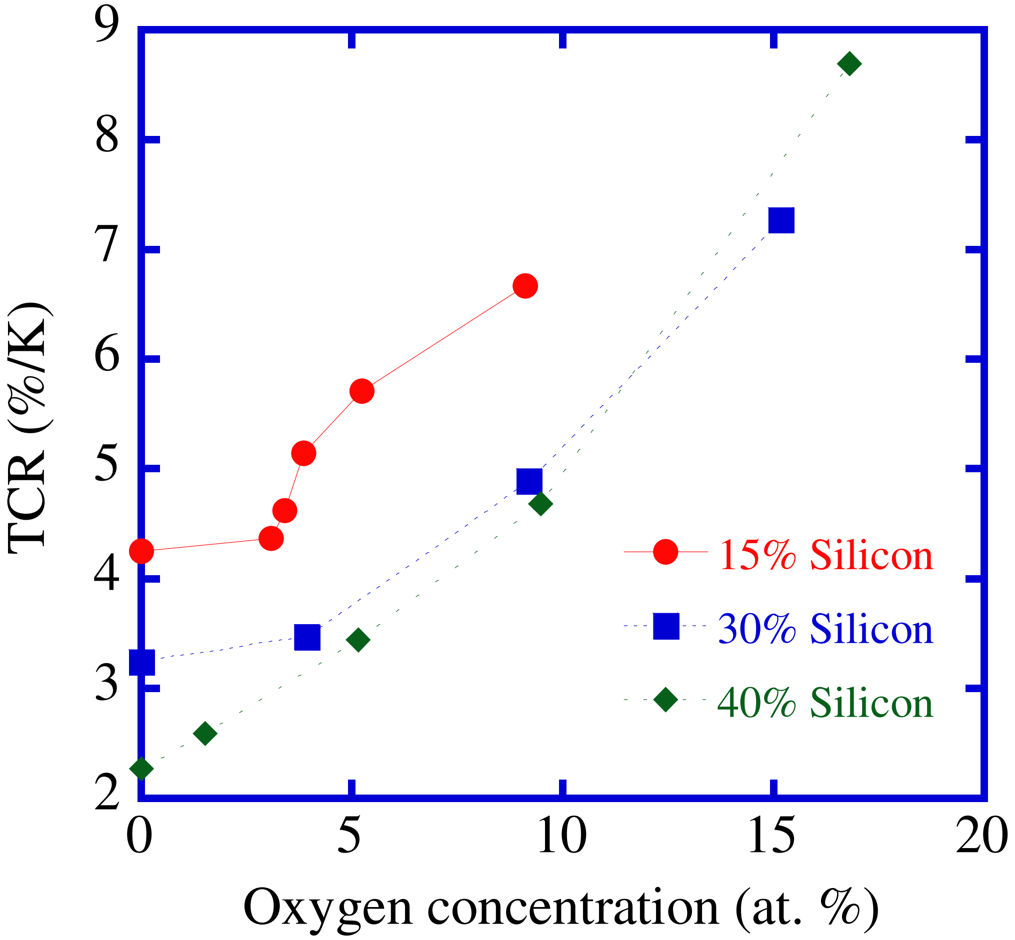

Figure 2.10 Variations of TCR with oxygen concentration in $Si_xGe_{1-x}O_y$

To demonstrate the comparison of 1/*f*-noise from different samples, the noise spectra from three samples are plotted in Figure 2.11. The noise spectra were measured with the same current of 1.79 μA flowing through each device. In this manner, the 1/*f*-noise displayed in the plot reflects the magnitude of K_f for the particular sample. Figure 2.11 shows the contribution of the 1/*f*-noise at low frequency and the Johnson noise of the 10 kΩ series resistor at higher frequencies. The 1/*f*-noise voltage power spectral density shown reflects the 1/*f*-noise current from the device flowing through the 10 kΩ series resistor. Table 2.1 shows the value of the factor K_f as well as the TCR, activation energy, and optical bandgap for different devices. There is a general trend that as the oxygen concentration is increased, the value of K_f is increased, reflecting higher 1/*f*-noise at higher oxygen concentrations. It should be noted that in some devices, particularly with high resistance, the noise spectra was system limited so only a upper bound on the normalized Hooge coefficient, K_f, could be determined. The upper bounds appear high in the case of the high resistance samples because the current used to normalize the power spectral density in computing the bound for the normalized Hooge coefficient are small. The measured values of the normalized Hooge coefficient reflect comparatively high 1/*f*-noise. Ahmed et al. [20] reported the value of 1/*f*-noise factor $k_{1/f}$ to be 2.9×10^{-11} for amorphous $Ge_xSi_{1-x}O_y$ bolometers where Sedky et al. [3] reported to have a noise value of 1×10^{-11} V^2/Hz at 1 Hz for reduced pressure CVD deposited poly SiGe bolometers. The noise values obtained in this work are compatible with those values. The origin of the 1/*f*-noise and its reduction is discussed in chapter 4.

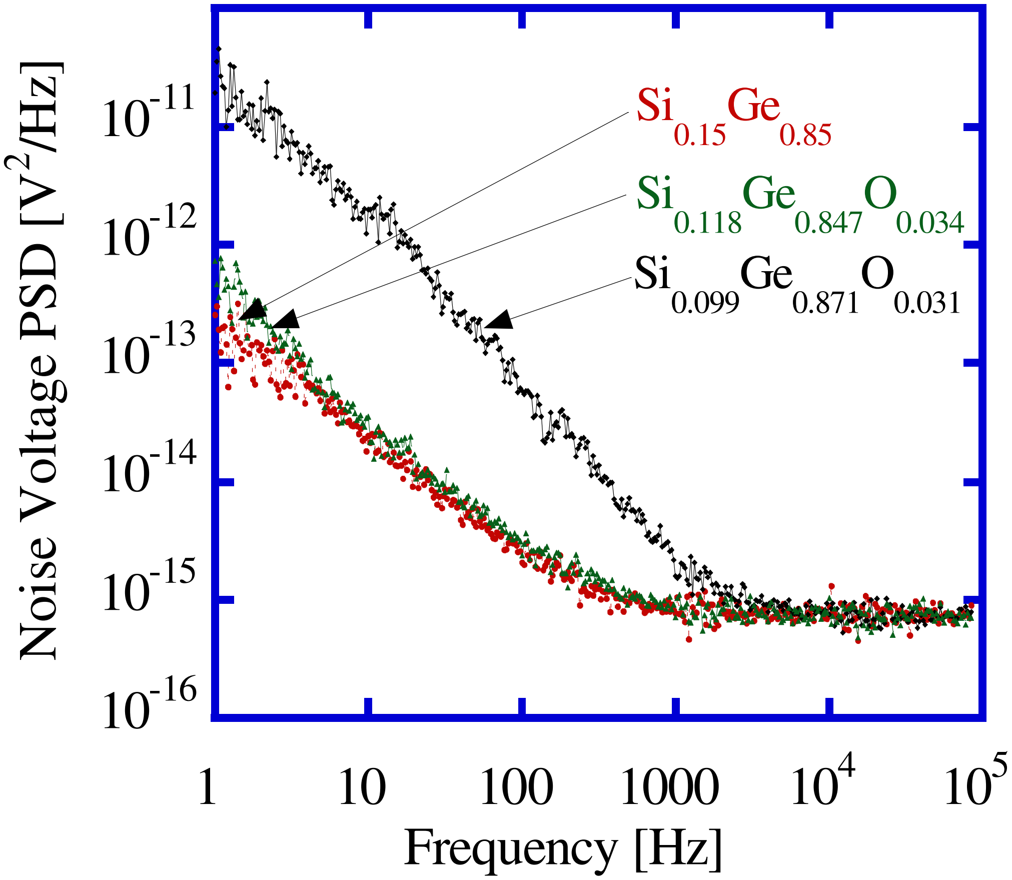

Figure 2.11 Voltage PSD for 1/*f*-noise for devices $Si_{0.15}Ge_{0.85}$, $Si_{0.088}Ge_{0.76}O_{0.031}$ and $Si_{0\cdot 118}Ge_{0.847}O_{0.034}$

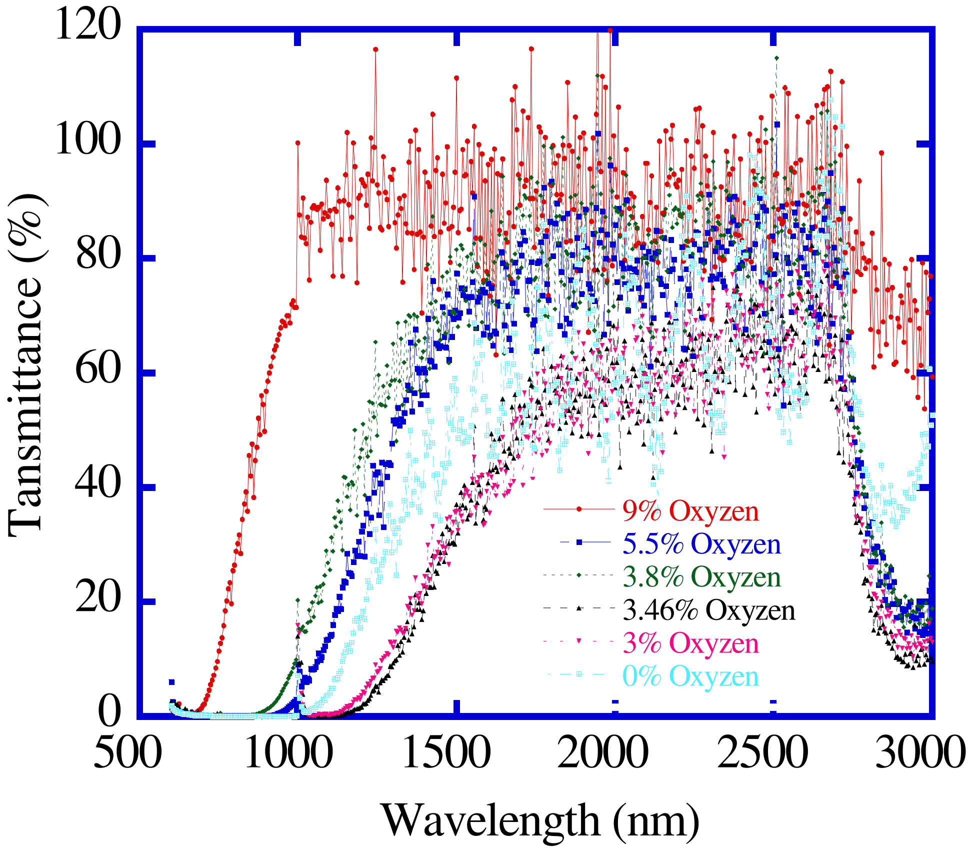

Figure 2.12 Transmission through $Si_{0.15}Ge_{0.85}O_y$ thin films with varying oxygen concentration and 15% silicon concentration

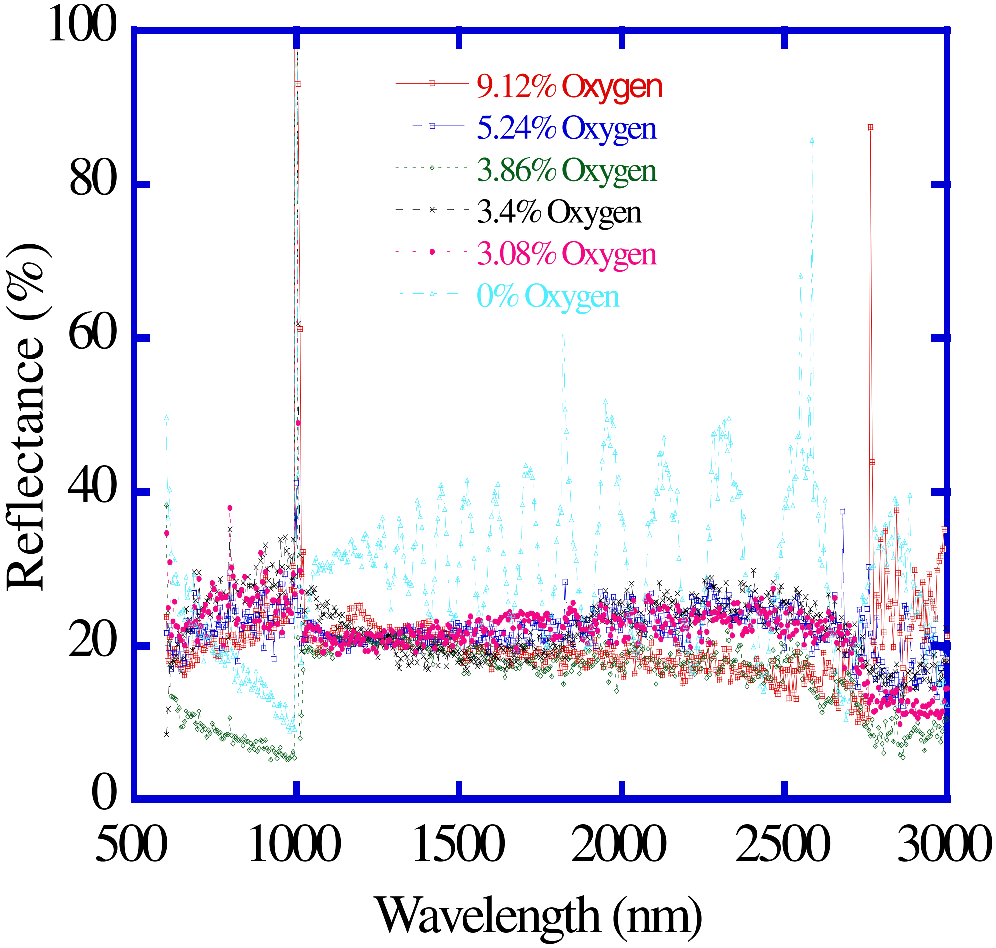

Figure 2.13 Reflection through $Si_{0.15}Ge_{0.85}O_y$ thin films with varying oxygen concentration and 15% silicon concentration

Optical transmission and reflection through $Si_{0.15}Ge_{0.85}O_y$ thin films are shown in Figure 2.12 and Figure 2.13 respectively. The transmission characteristics display attenuation of the optical signal at short wavelengths due to the photogeneration of carriers for photon energies greater than the optical bandgap. As the wavelength increases, the transmission increases as the photon energy becomes less than the band gap. Near 3000 nm, the absorption of the glass substrate is displayed. The addition of oxygen to $Si_xGe_{1-x}O_y$ tends to increase the transmittance through the samples at the longer wavelengths compared to lower oxygen concentrations. This is due to the smaller optical bandgap at lower oxygen concentrations. The transition from low transmittance to high transmittance was found to be sharper as more oxygen was added to the thin films. The reflectance of the samples was relatively constant over the wavelength range and only decreased slightly with increasing oxygen concentrations. The devices with 30 % and 40 % silicon concentrations exhibited the similar transmission and reflection characteristics as the oxygen concentration was varied. It can be seen from Figure 2.14 that the transmission through cover glass substrate is almost 100% in the wavelength range we are looking for, suggesting the transmission and reflection characteristics of $Si_{1-x}Ge_xO_y$ thin films solely belong to them. The transmittance and reflectance of sample $Si_{0.15}Ge_{0.85}$ are plotted together in Figure 2.15.

The optical bandgap, E_g, was obtained by fitting the optical absorption coefficient α to Tauc's [21], [22], [23], [24] relation for an indirect bandgap semiconductor.

$$[\alpha(h\nu)]^{1/2} = B(h\nu - E_g) \tag{2.2}$$

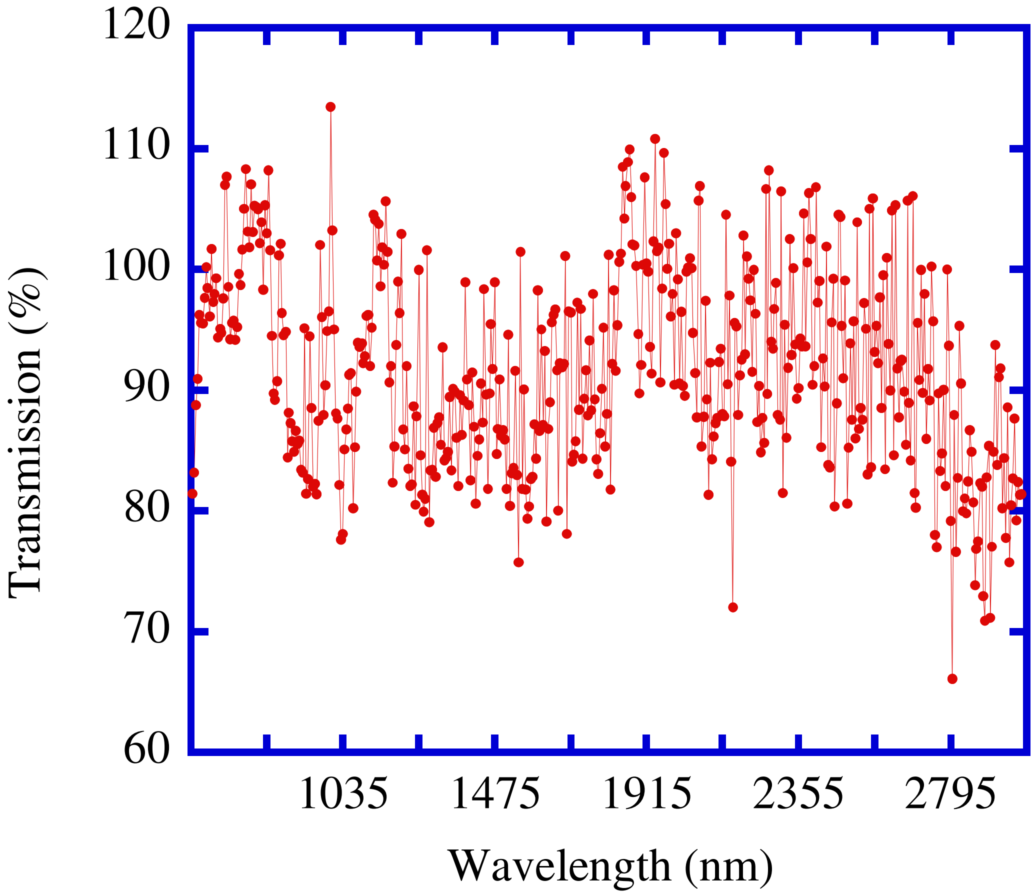

Figure 2.14 Transmission through cover glass substrate

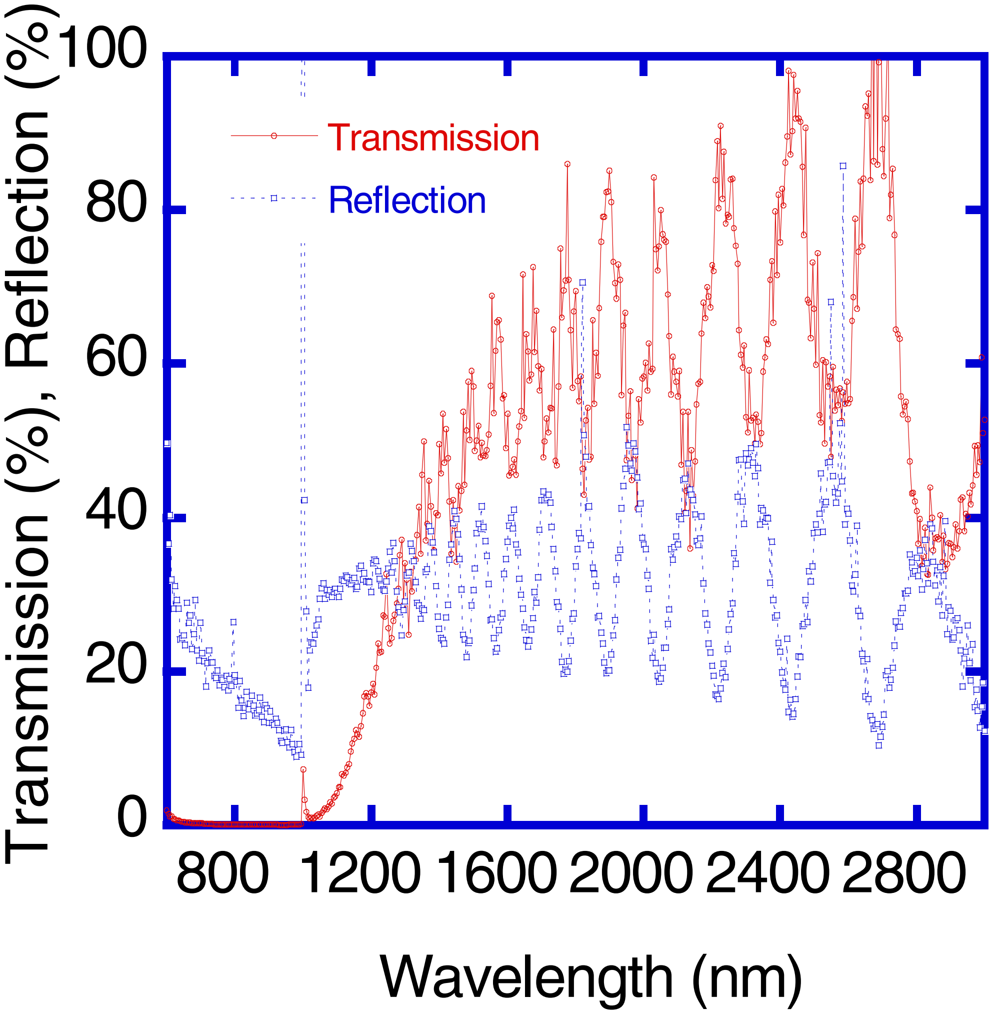

Figure 2.15 Transmission and reflection through $Si_{0.15}Ge_{0.85}$ thin film

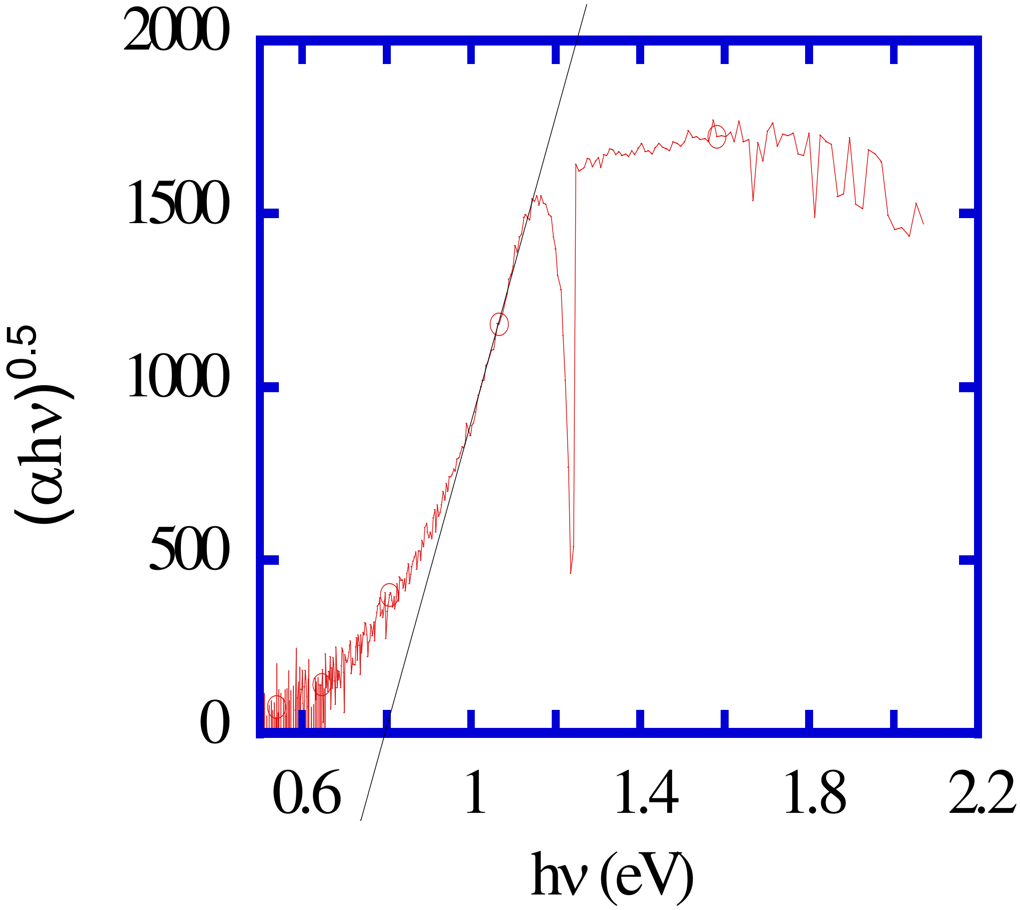

Figure 2.16 Determination of optical bandgap energy of $Si_xGe_{1-x}O_y$ thin film from transmission and reflection data

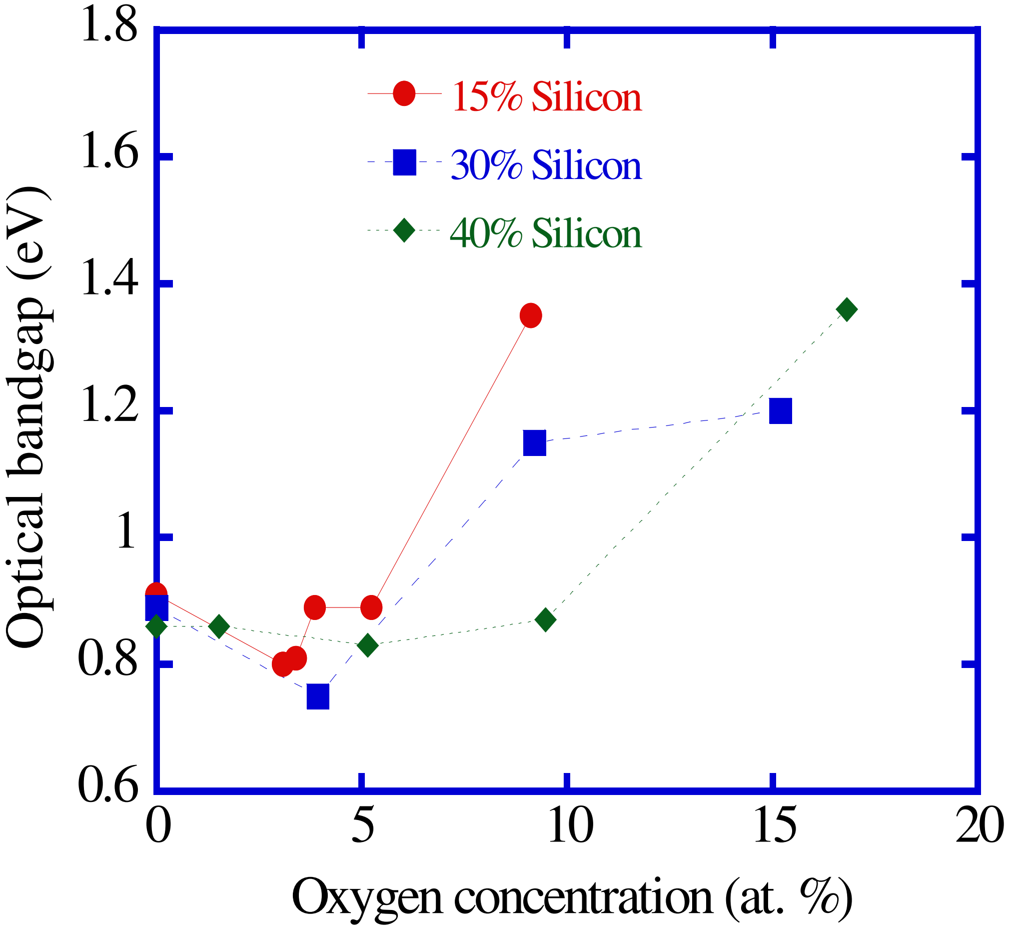

Figure 2.17 The optical bandgap energy of $Si_xGe_{1-x}O_y$ thin films

where, α is the absorption coefficient, B is a constant. The absorption coefficient α was determined from the relation [23]

$$T = \frac{(1-r)^2 \exp(-\alpha x)}{1-r^2 \exp(-2\alpha x)} \tag{2.3}$$

where, T is the transmittance, r is the reflectance and x is the film thickness. Extrapolation of $(\alpha h\nu)^{1/2} = 0$ of linear portion in the plot of $(\alpha h\nu)^{1/2}$ versus the photon energy $h\nu$, gave the value of optical bandgap [21], [22], [23], [24]. Figure 2.16 shows the graph for determining the optical bandgap value. Figure 2.17 shows the optical bandgap for different silicon concentrations with varying oxygen concentration. It can be observed from Figure 2.17 that for $Si_{0.15}Ge_{0.85}O_y$ thin films, the increase in oxygen concentration increased the optical bandgap. However, for low oxygen concentrations the optical bandgap changes very little with the increase in oxygen concentration, perhaps decreasing slightly before increasing dramatically for concentrations above 5 %. For the 3 % and 3.5 % oxygen concentration samples, which showed the decrease in optical bandgap, the Si concentration was measured to be 9.85 % and 11.88 % respectively, which are lower than the other samples whose Si concentrations were close to 15 %. Samples with 30 % and 40 % Si concentrations had similar optical bandgap characteristics to the 15 % Si concentration when the oxygen concentration was varied. These results are complying with Ahmed et. al [18].

For amorphous semiconductors like $Si_xGe_{1-x}O_y$ or Si_xGe_{1-x}, there exists a smooth variation of the density of states with energy in the localized states, which are known as band tails [25]. These band tails form due to disorder [18] and lie in the vicinity of midgap. The dominant conduction mechanism in these films is believed to be due to the excitation of carriers from the midgap to the band tails. For all the samples the activation energy was found to be less than half of the optical bandgap. The existence of similar variation of optical bandgap and the activation energy with the oxygen concentration support this argument for the band structure in all the samples. All the films found to transmit at a larger wavelengths (<1000 nm). So to make them suitable for long infrared (8-14 μm) operation, the use of an absorber is necessary.

2.4 Conclusions

Deposition technique of $Si_xGe_{1-x}O_y$ or Si_xGe_{1-x} thin films by RF magnetron sputtering was discussed in this chapter. Some of the optical and electrical properties of amorphous films of $Si_xGe_{1-x}O_y$ or Si_xGe_{1-x} were discussed. Other than presence of high 1/*f*-noise, films of $Si_xGe_{1-x}O_y$ or Si_xGe_{1-x} were found to be an attractive for microbolometer thermometer.

CHAPTER 3

DOPED Si_xGe_{1-x} MICROBOLOMETER

3.1 Introduction

Highly doped semiconductor materials have the advantage of low resistivity. Bolometers of doped Si_xGe_{1-x} were fabricated to obtain a lower pixel resistance. In chapter two it was discussed that the suitable combination of RF sputtered films of $Si_xGe_{1-x}O_y$ would result in moderate resistivity. While attempted to fabricate $Si_xGe_{1-x}O_y$ bolometers, it was found that the pixel resistance of 40 × 40 μm^2 bolometer was about 30 MΩ. The pixel resistance increased to about 80 MΩ after completing the surface micromachining. Surface micromachining was done by taking off the sacrificial polyimide layer in the oxygen plasma ashing for about ten hours. Exposing the sensing layer for that much long period might have resulted in increase in the detector pixel resistance. In order to achieve a lower detector pixel resistance, highly doped silicon germanium was used as the thermometer.

3.2 Bolometer Fabrication

The infrared bolometers were designed to form suspended bridge structures of linear arrays and single pixel devices. In the linear arrays the pixel sizes are 60×60 and 40×40 μm^2 and they are separated from each other by 10 μm. To fabricate miocrobolometers, all the layers were deposited in a similar way by RF magnetron

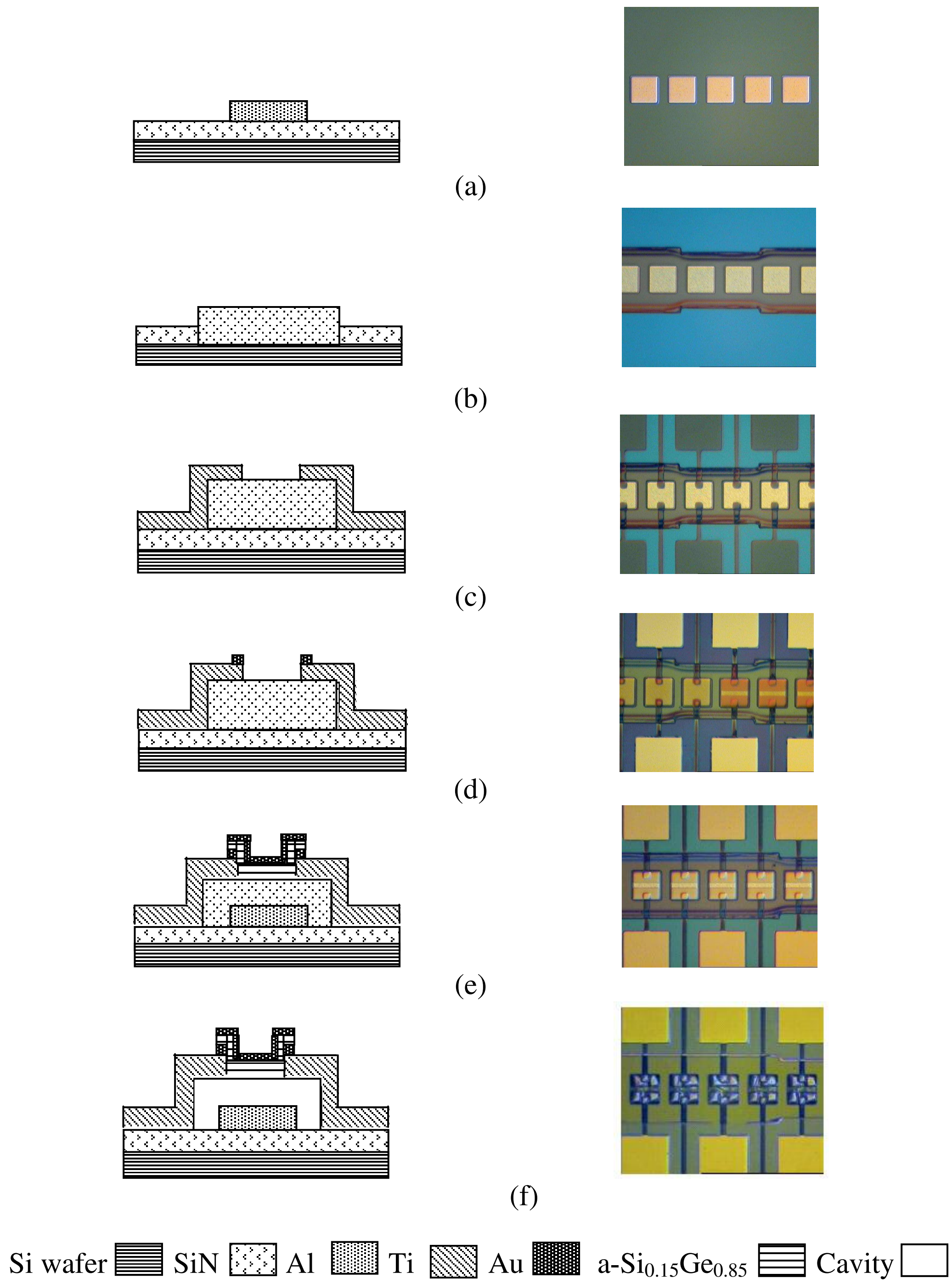

Figure 3.1 Doped a-$Si_{0.15}Ge_{0.85}$ bolometer fabrication steps: schematic (left) and optical microscope picture (right) after (a) SiN deposition and Al pattern (b) polyimide cure (c) Ti arm pattern (d) Au contact and bond pad pattern (e) a-$Si_{0.15}Ge_{0.85}$ and Au lift off (f) polyimide ash

sputtering system mentioned in section 2.1.

The fabrication procedure began with the deposition of a 400-nm-thick SiN layer on top of a cleaned lightly doped p-type 3″ diameter Si wafer. This SiN layer serves as the electrical insulation layer between Si and other subsequent layers which will be deposited later. Then a 340-nm-thick Al layer was deposited. Sputtered Al-film was patterned by positive photo lithography with the help of positive photoresist S1813 from Shipley Company and diluted Al-etch. Positive lithography was done by spin coating S1813 at 2000 rpm for 40 seconds followed by pre bake at 95 ^{o}C for 120 seconds on a hot plate. Then it was exposed by using ultraviolet ray. Then the resist was baked on hot plate for 120 seconds at 115 ^{o}C to complete the post exposure bake. It was then developed in MF319 positive resist developer for 120 seconds. A diluted aluminum etch (Al etch : DI water = 1: 9) heated at 55 ^{o}C was used to etch the aluminum. An etch rate of about 40nm/minute was obtained. The wafer was then rinsed in DI water, followed by a blow dry in nitrogen. Patterned Al has the square geometries of pixel size and served as the mirror to reflect the incident infrared ray. Figure 3.1 (a) shows patterned Al mirrors. A sacrificial layer made of photo definable polyimide PI2737 form HD Microsystems was used to form the bridge structure and was removed at the last step of fabrication. PI2737 was spin coated onto the wafer at 1630 rpm for 60 seconds and then baked on hot plates at 65 ^{o}C and 95 ^{o}C, both for 180 seconds. Then the polyimide was exposed to ultra violet light and developed in DE 9040 for 30 seconds followed by a rinse in rinse solution RI 9180 for 40 seconds. The patterned polyimide was cured in the convection oven at 275 ^{o}C for four hours which resulted in rectangular mesa structure of 2.2 μm thick. Figure 3.1 (b) shows the device after polyimide cure. Ti electrode arms were patterned using lift off by a combination of imaging negative resist NR7-1500P from Futurrex Corporation and lift-off resist LOR 3B from MicroChem Corporation. First the wafer was baked at 200 ^{o}C on a contact hot plate for 5 minutes to dehydrate. Then LOR 3B was spin coated at 3000 rpm for 45 seconds followed by a pre-bake at 170 ^{o}C for 180 seconds. Then the negative resist NR7-1500P was spin coated at 3000 rpm for 40 seconds followed by a pre-bake at 150 ^{o}C on a hot plate for 60 seconds. Then the sample was exposed in the ultra violet ray and followed by a post exposure bake on the hot plate at 120 ^{o}C for 60 seconds. The resist was then developed in the diluted solution of RD6-a negative resist developer from Futurrex Corporation for 90 seconds followed by a rinse in the DI water and blow dry with N_2. The developer solution was diluted by mixing DI water in it to have better control during the developing. Then a 145-nm-thick Ti film was deposited and the wafer was immersed into the 1165 Striper from MicroChem Corporation and performed ultrasonic agitation for 10 seconds followed by a DI water rinse and blow dry with N_2 to complete the lift-off process. Figure 3.1 (c) shows the device after Ti arm pattern. Then a 70-nm-thick Au layer was sputtered to form the contact pads and the contacts between the Ti arms and the sensing layer of $Si_{0.15}Ge_{0.85}$. The Au layer was patterned and etched in KI : I_2 solution. Figure 3.1 (d) shows the device after Au contact and pad pattern. Then a 200-nm-thick $Si_{0.15}Ge_{0.85}$ film was sputtered from a compound target of $Si_{0.15}Ge_{0.85.}$ The target was prepared by bonding pieces of a doped n-Si (B doped, 2×10^{14} /cm^{3}) wafer to a Ge sputter target with the area

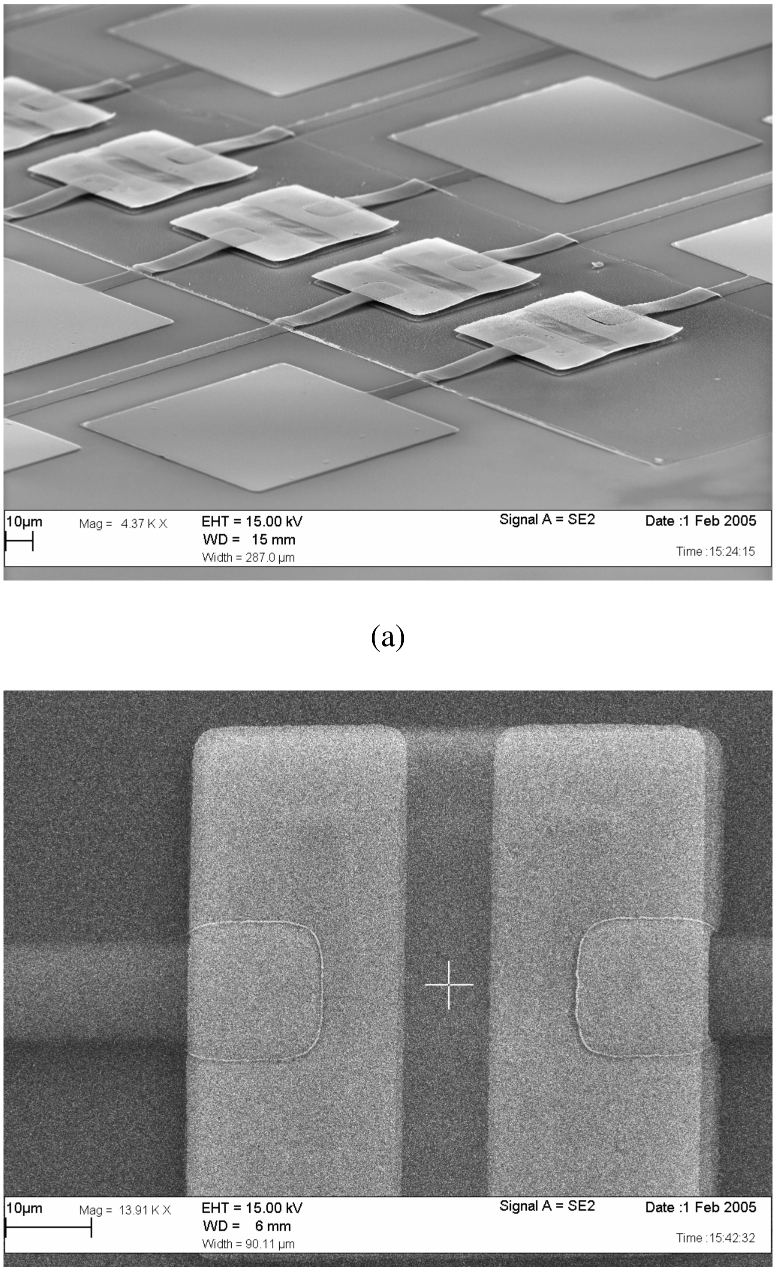

(a)

(b)

Figure 3.2 (a) SEM micrograph of suspended 60 × 60 µm^2 detectors array (b) closer view of an individual 60 × 60 µm^2 detector occupied by the Si pieces determined the Si concentration. This was followed by a deposition of 20-nm-thick Au layer. The deposited $Si_{0.15}Ge_{0.85}$ and Au layers were lifted off together using the procedure mentioned before for Ti lift off. Figure 3.1 (e) shows the device after lift off. The top Au layer serves as an absorber for infrared radiation, path for low resistance current flowing and stops the oxidation of $Si_{0.15}Ge_{0.85}$ layer when it will be exposed to O_2 plasma for removing the sacrificial layer of PI2737 later on. After that, the PI2737 sacrificial layer was removed in the O_2 plasma ashing for about 10 hours and 100 watts of RF power at 120 mTorr pressure and 40.1 SCCM O_2 flow. The completed device is shown in Figure 3.1 (f). At this stage microbolometers of suspended structure (micromachined) are obtained. Figure 3.2 (a), and 3.2 (b) show the SEM pictures of arrays of micromachined devices and a single pixel of $60 \times 60\ \mu m^2$ respectively.

3.3 Bolometer Characterization and Discussions

Two devices namely 10C51 and 10C52 of $60\times60\ \mu m^2$ pixel size were bonded and characterized. The resistance of the device 10C51 was found 68.7 kΩ at 325 K and 155 kΩ at 270 K while for device 10C52 these values were 41.4 kΩ and 87.5 kΩ respectively. The activation energy was found for device 10C51 and 10C52 were 0.0843 eV and 0.0931 eV respectively. Thus at 294 K the TCR was -1.13%/K and – 1.25%/K for device 10C51 and 10C52 respectively (Figure 3.3). The low TCR value obtained from these devices is believed mainly to be due to the highly doped Si target used which is in agreement with Garcia et al. [14]. In fabricating the microbolometers, contact resistance, pixel resistance, and 1/*f*-noise were found to be important issues in the application of room temperature, sputtered $Si_{0.15}Ge_{0.85}O_{0.035}$ and $Si_{0.15}Ge_{0.85}$ thin films. In current work, as mentioned before, the use of intrinsic $Si_{0.15}Ge_{0.85}$ and $Si_{0.15}Ge_{0.85}O_{0.035}$ films as thermister resulted in high value of device resistances (~76 to 129 MΩ). A doped Si target with intrinsic Ge target resulted in decreased device resistance, however the TCR also decreased. Hence, there is a tradeoff between obtaining a reasonable pixel resistance and the TCR of the bolometer. The *I-V* characteristics of these devices were measured with a HP 4155B semiconductor parameter analyzer. The current was varied from -20 to 20 µm for this purpose. As seen in Figure 3.4, linear *I-V* characteristics were obtained with low device resistance. The linear *I-V* characteristics were the result of using highly doped Si in the Si_xGe_{1-x} sputter target and choosing Au as a contact material. The vertical conduction geometry of the bolometer pixel was designed to provide a relatively low resistance path from the moderately high resistivity $Si_{0.15}Ge_{0.85}$. In this case, the current flows through the device from one electrode through the Au contacts, and sensing layer to the absorber, and then comes back to the other electrode. This geometry reduced the device resistance significantly and hence resulted in a low Johnson noise. To develop an Ohmic contact between the sensing layer of Si_xGe_{1-x} and the electrode arm, two other metals- Cr and Ti were tested. Two test samples were fabricated with and without Au contacts in between the Cr or Ti and Si_xGe_{1-x} layer. At this time, a sputter target with lightly doped p-type Si was used to deposit the Si_xGe_{1-x} films. The currents through those samples were varied from -100 nA to 100 nA. The *I-V* curves for different samples are shown in Figure 3.5. It was found that the contacts formed with Au were more Ohmic and provided lower contact resistance to the

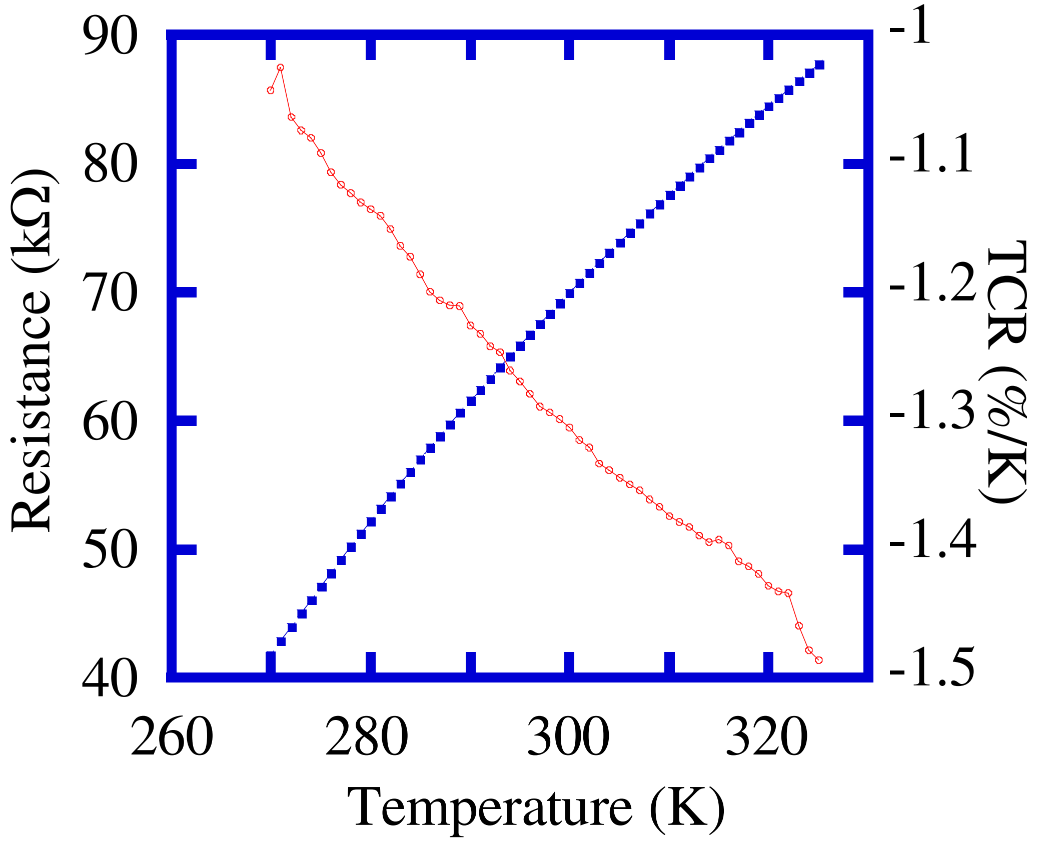

Figure 3.3 Dependence of TCR and resistance on temperature for device 10C52

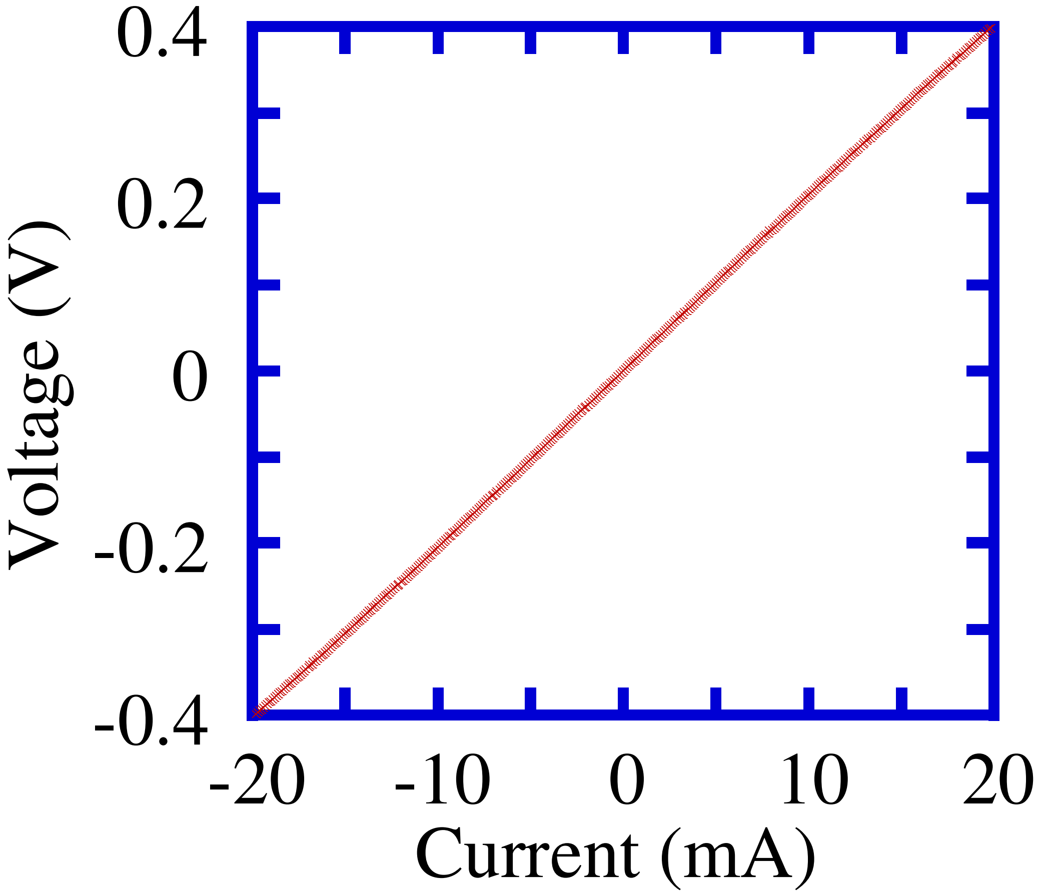

Figure 3.4 *I* –*V* characteristics of 10C52 in air

$Si_{0.15}Ge_{0.85}$ than either with Ti or Cr. Using a gold contact has the additional advantage that it is not expected to oxidize during the reactive sputtering of $Si_xGe_{1-x}O_y$ thin films. The thermal conductance of the device was measured by the method of Joule heating. The following relation was used to calculate the thermal conductance [26].

$$R(T) = R_0 + \frac{dR}{G_{th}dT} I_b^2 R(T) \tag{3.1}$$

The current was swept from -200 to 200 μA by a HP 4155B semiconductor parameter analyzer while the device 10C52 was placed in air and in vacuum ambient. This *I-V* data was used to determine the resistance associated at each point and the corresponding power dissipation. From the slope of the power versus resistance curve, the value of G_{th} was calculated. Figure 3.6 shows the *I-V* characteristics for determining the G_{th} of 10C52. The value of G_{th} for devices 10C51 and 10C52 were approximately 10^{-5} W/K in both air and vacuum. This value of thermal conductivity is higher than expected and shows poor isolation between the sensing layer and substrate. The electrical noise in the microbolometers was measured by placing them inside a cryostat in a low frequency electromagnetically shielded room. The cryostat was evacuated to a pressure of 75 mTorr by a mechanical vacuum pump. Each device was current biased and the noise voltage PSD was measured across the device. A PAR113 amplifier with gain of 50 was connected to a HP 3562A signal analyzer for this purpose. The noise voltage PSD was recorded over the frequency range of 1 Hz to 100 kHz. The recorded noise voltage PSD expresses the measure of 1/*f*-noise from the devices. The value of the noise PSD for device 10C52 was measured at different bias currents as shown in Figure 3.7. For 1 mA

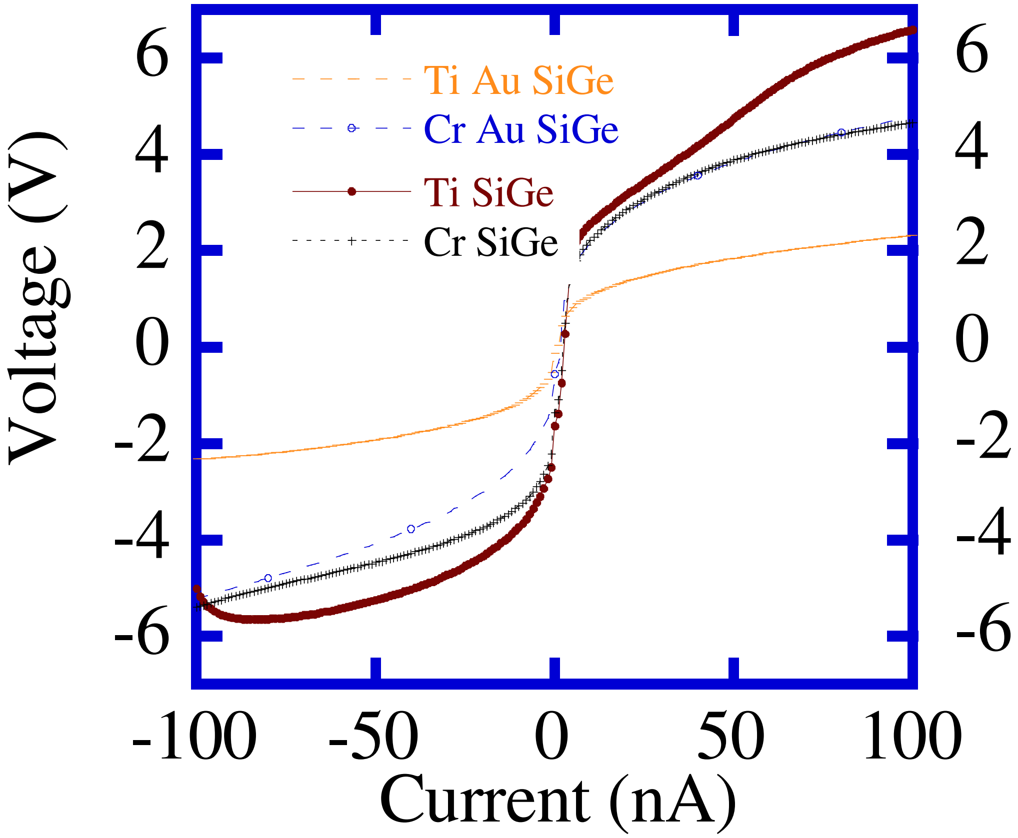

Figure 3.5 *I-V* characteristics of different metal and doped n-$Si_{0.15}Ge_{0.85}$ contacts

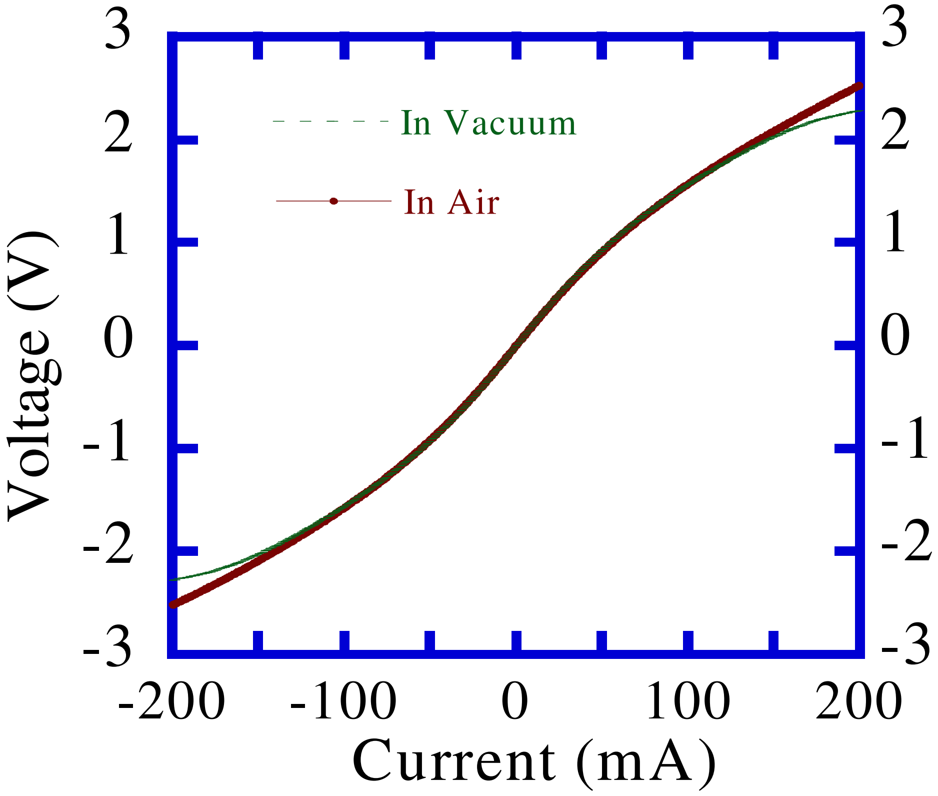

Figure 3.6 *I-V* characteristics of device 10C52 for determining G_{th} by Joule heating method

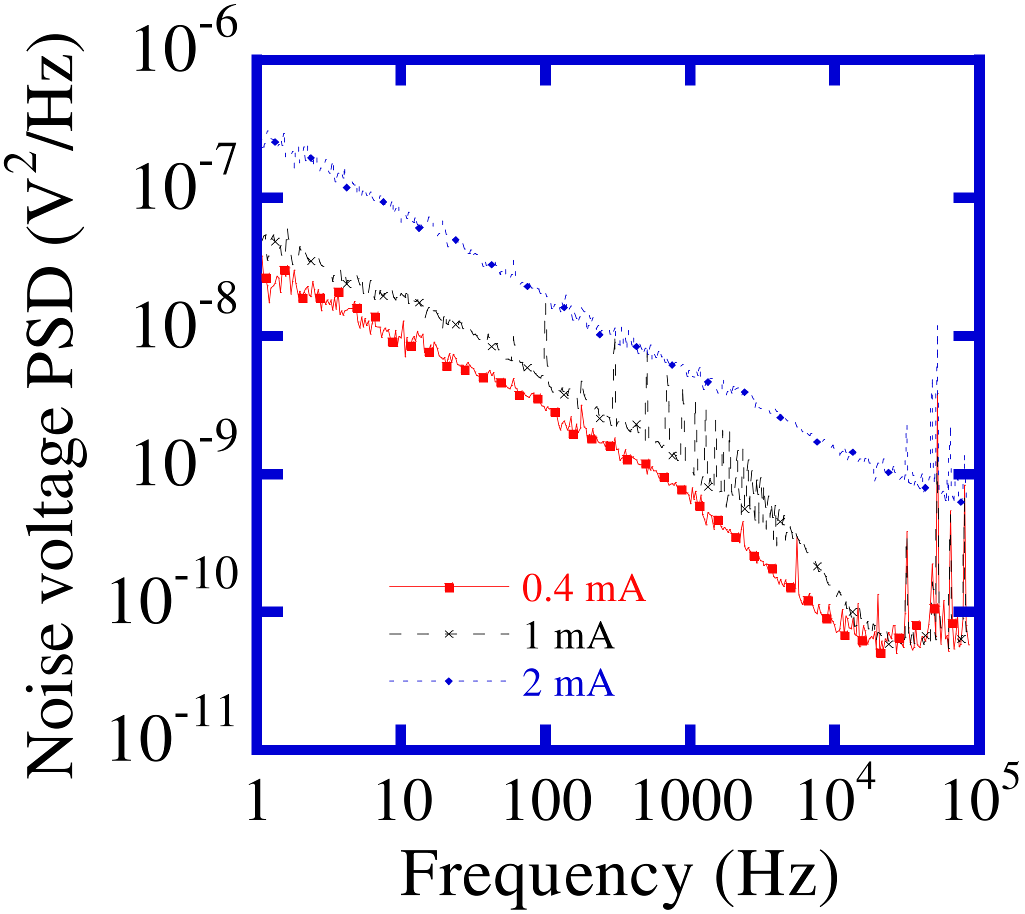

Figure 3.7 Noise voltage PSD of 10C52 at different bias currents

bias, the microbolometer was illuminated with filtered infrared radiation from a thermal source covering the spectral range of 2.5-15 µm with a modulation frequency of 100 Hz. In this case, the photon energies are less than the optical band gap energy of the $Si_{0.15}Ge_{0.85}$ thin films [2]. There was no observed effect on the noise power spectra due to the optical illumination. From the measured voltage noise power spectral densities, the relative magnitude of the $1/f$-noise was determined through the value of the normalized Hooge parameter K_f. In this case, K_f was measured to be 4.4×10^{-5}. This value is higher than the K_f value measured for several room temperature, RF sputtered thin films of Ge, $Si_{0.4}Ge_{0.6}$, and $Si_xGe_{1-x}O_y$ thin films investigated in chapter 2. The frequency dependence of the power spectral density was found to vary approximately as $1/f^{0.5}$.

3.4 Conclusions

Fabrication and characterization of doped Si_xGe_{1-x} microbolometer is discussed in this chapter. The use of boron doped Si reduced both the TCR and the resistance of the pixel. Presence of high $1/f$-noise degraded the bolometer performance.

CHAPTER 4

FORMING GAS PASSIVATION OF $Si_xGe_{1-x}O_y$ MICROBOLOMETERS

4.1 Introduction

The amorphous semiconductor detector materials are characterized by high 1/*f*-noise. Poly SiGe [8], amorphous SiGe alloys [14] and amorphous $Ge_xSi_{1-x}O_y$ [17], [27] are attractive materials of SiGe family for bolometers mainly because of their high TCR, although they exhibit high 1/*f*-noise. Ahmed et al. [20] reported the degradation of bolometer performance by excess 1/*f*-noise for amorphous $Ge_xSi_{1-x}O_y$ bolometers. Garcia et al. [14] used a mixture of SiH_4 + GeH_4 by low frequency low pressure chemical vapor deposition technique to deposit a-$Si_{1-x}Ge_x$:H,F. They also used a-Si_3N_4 to passivate the a-$Si_{1-x}Ge_x$:H,F layer. In this case, hydrogen is incorporated during the deposition process. When a-$Ge_xSi_{1-x}O_y$ is deposited typically by reactive RF magnetron sputtering, hydrogen is not incorporated into the system. So in this work, the post-deposition passivation by forming gas is investigated. Garcia et al. experienced lower detectivity (2.6×10^6 cmHz$^{-1/2}$ W^{-1}) because of relatively high 1/*f*-noise. NASA/Goddard Space Flight Center in collaboration with the University of Wisconsin [28] has reported that by increasing the Si or Ge thermistor's thickness significantly, the 1/*f*-noise can be reduced. This indicated a volumetric dependence of the 1/*f*-noise, rather than a dependence on surface states. But

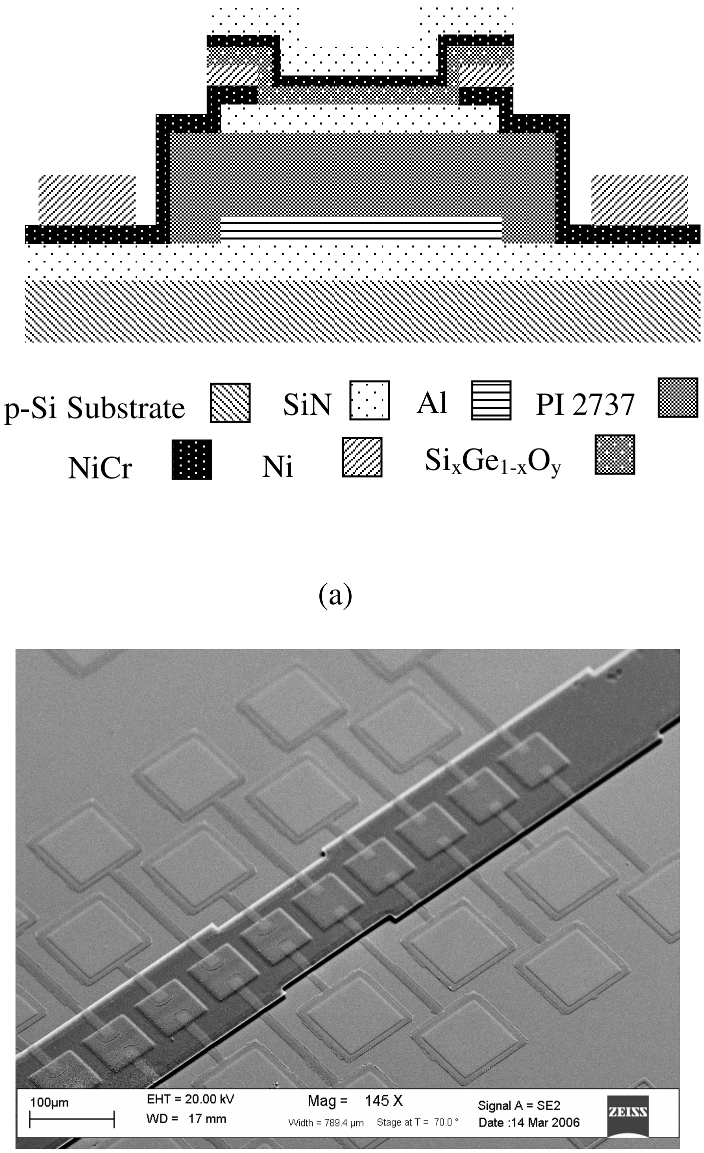

(a)

(b)

Figure 4.1 (a) Cross section of a $Si_xGe_{1-x}O_y$ microbolometer (b) SEM micrograph of 60 × 60 μm^2 microbolometer array

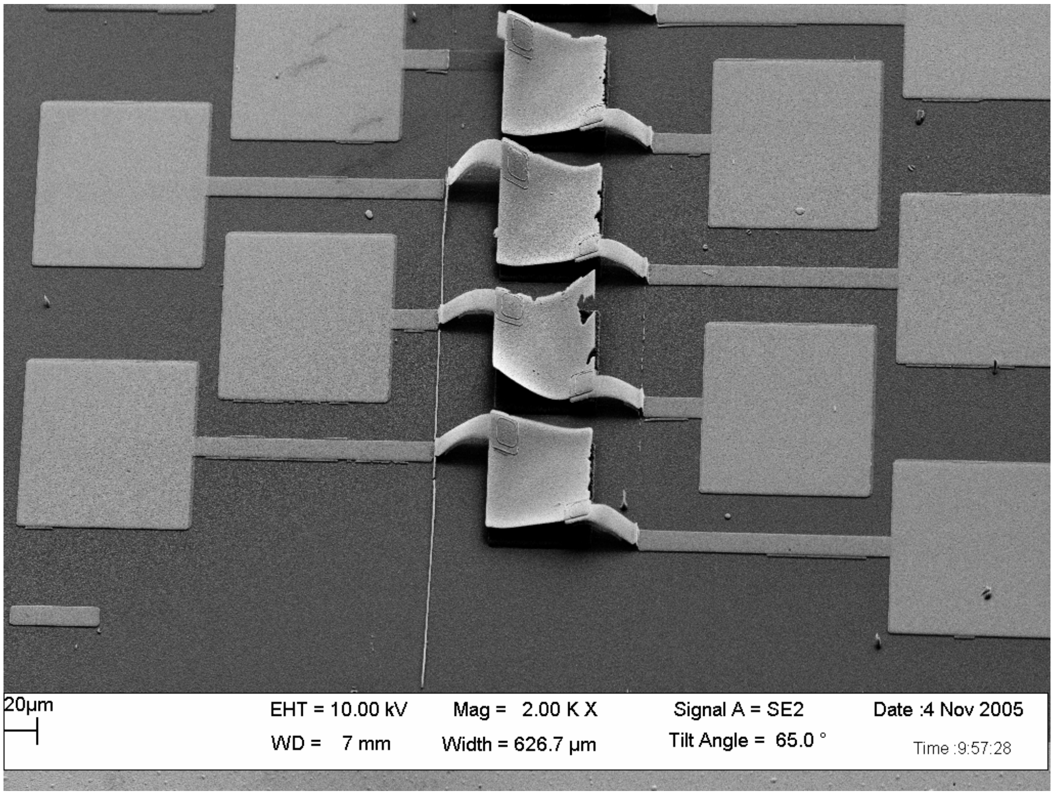

Figure 4.2 SEM micrograph of warped microbolometer arrays without silicon nitride sandwich layer

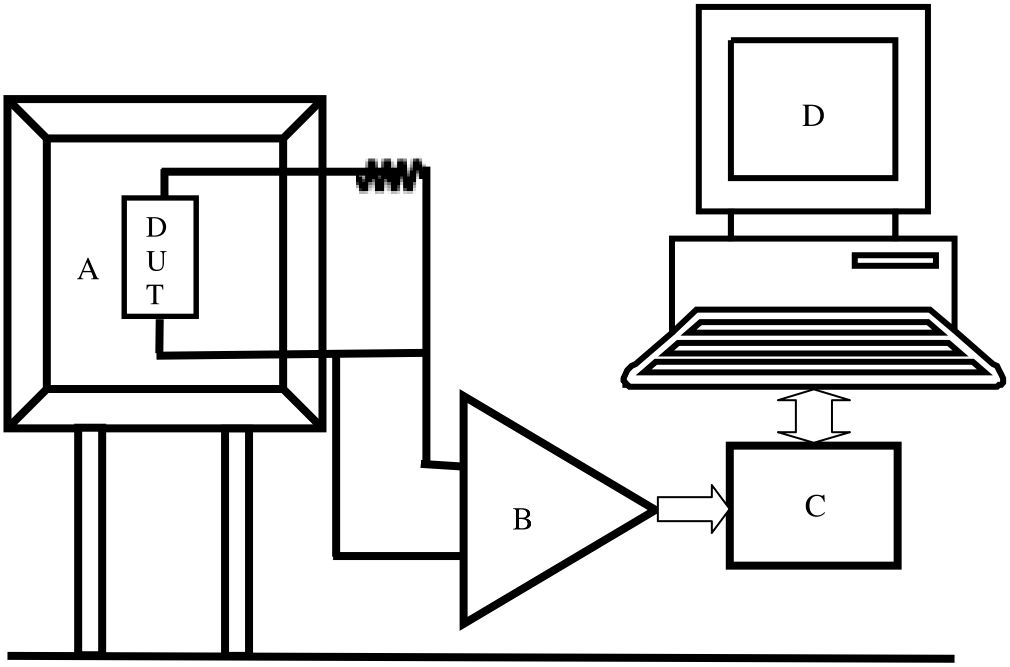

A Shielded Probe Station
B SRS 560 Low Noise Amplifier
C HP 3562A Dynamic Signal Analyzer
D Computer

Figure 4.3 Schematic for noise measurement setup increasing the thermistor thickness will add thermal mass and it will make the thermal time constant of the detector larger.

High 1/*f*-noise was found in the $Si_xGe_{1-x}O_y$ thin films and doped $Si_{0.15}Ge_{0.85}$ microbolometers as mentioned in chapter two and chapter three respectively. If this noise can be eliminated, then the detector's performance can be improved significantly. To reduce the noise voltage PSD of detectors, forming gas passivation was done for different interval of time. The origin of 1/*f*-noise and its reduction by forming gas passivation is explained in the results and discussions section.

4.2 Experimental Details

4.2.1 Bolometer Fabrication

Figure 4.1 (a) and Figure 4.1 (b) show the cross sectional view and the SEM micrograph of the fabricated device. The depositions of different layers other than the Al and polyimide were done by a RF magnetron sputtering system equipped with a turbo pump and a three-inch target holder. Prior to sputtering, the process chamber was evacuated to 3×10^{-6} Torr by the turbo pump. Sputtering was done at 10 mTorr pressure. An Ar flow of 32 SCCM was used in every sputtering process other than $Si_xGe_{1-x}O_y$ deposition. In fabricating the bolometer, lift off technique was used for patterning all the films because of its simplicity.

The fabrication of the bolometer starts by depositing 400 nm of silicon nitride on a cleaned lightly doped p-type, three inch diameter silicon wafer. This layer of silicon nitride served as the electrical insulation for the substrate and would withstand all the solvents used in next fabrication steps. Then a 400-nm-thick layer of Al was deposited by thermal evaporation and patterned. The cryo pump of the evaporator was cooled down to 20 K after which the sample was mounted. The chamber was evacuated to 1×10^{-6} Torr prior to evaporation. A deposition rate of 5 angstrom/sec was achieved at 100 Ampere of applied current. To perform the lift off, negative resist NR7-1500P from Futurrex Corporation was spin coated on the wafer at 3000 rpm for 30 seconds. Then the wafer was pre baked at 150 ^{o}C for 60 seconds on a hot plate and exposed under the ultraviolet light. A post exposure bake for 60 seconds was done at 120 ^{o}C on a hot plate. Then the resist was developed in RD6-a negative resist developer from Futurrex Corporation for 50 seconds. The resist thickness was found to be about 1.8 μm after developing. This was found to be thick enough to lift off 0.4-μm-thick Al layer. After depositing Al film, the wafer was kept in 1165 photo resist striper for about two hours to complete the lift off process. The wafer was then rinsed with acetone, methanol, and DI water followed by a blow dry in nitrogen to make it clean. This Al layer would serve as a mirror for reflecting the infrared rays and form the basis of an optically resonant cavity. Then a sacrificial layer of photo definable polyimide PI-2737 from HD Microsystems was spin coated, patterned by conventional photolithography and wet etching process. The polyimide was cured in the convection oven. After curing the polyimide thickness was found 2.2 μm. For patterning, the polyimide was spin coated at a speed of 1650 rpm for 60 seconds. Then it was baked on two steps hot plate. In first step, it was baked at 70 ^{o}C, while in second step it was baked at 100 ^{o}C, both for three minutes. Then it was exposed in ultraviolet light. For developing polyimide, developer DE 9040 along with rinse solution RI 9180, both from HD Microsystem, were used. To store these solutions and complete developing process, four tanks and one squeeze bottle were used. First two of the four tanks were filled with 100% DE 9040 solution, third tank was filled with 50% DE 9040 and 50% RI 9180 solutions, fourth tank was filled with 25% DE 9040 and 75% RI 9180 solutions, while the squeeze bottle was filled with 100% RI 9180 solution. The wafer was kept inside the first two tanks for 10 seconds and agitated ultrasonically. Then it was transferred to the second and third tank respectively where it was kept for 15 seconds in each of them. Then the wafer was rinsed with RI 9180 solution for 20 seconds, by holding it vertically to remove all the polyimide flakes. By using four tanks instead of one tank, the problem of flakes generation was solved. The polyimide thickness at that point was about 5.3 μm. This was then cured in an oven at 250 ^{o}C for four hours in nitrogen ambient. The temperature was ramped slowly (from room temperature to 250 ^{o}C in one and half hours) to avoid possible thermal stress in the film. To achieve low thermal mass, the sensing layer of $Si_xGe_{1-x}O_y$ was made 200-nm-thick. In order to make the sensing layer mechanically strong as well as free of warping, a sandwich structure of $Si_xGe_{1-x}O_y$ was made employing silicon nitride. The sandwich layers increase the thermal mass of the detector. However, they were found to be necessary, since the first type of the bolometers were fabricated without silicon nitride sandwich layers and they were found to be warped after removing the sacrificial polyimide. Figure 4.2 shows the SEM picture of these devices. To achieve the sandwich structure, first the bottom silicon nitride layer was deposited and patterned. The thickness of this layer was set to 100 nm. Silicon nitride was chosen for this case, because silicon nitride is known to passivate silicon dioxide [29], although in current work it was not observed any significant effect of passivating the $Si_xGe_{1-x}O_y$ sensing layer with silicon nitride. Next, a 200-nm-thick NiCr (20% Ni, 80% Cr) electrode arm was deposited and patterned. NiCr has very low thermal conductivity, and thus provides good thermal isolation between bolometer thermometer and substrate. To form an Ohmic contact with p-type $Si_xGe_{1-x}O_y$, a 50-nm-thick Ni film was deposited on top of NiCr arm and patterned. Then, the sensing layer of $Si_xGe_{1-x}O_y$ was deposited in an Ar:O_2 environment from a compound target of Si_xGe_{1-x}. Next, a 14-nm-thick Ni absorber and 100-nm-thick silicon nitride layers were deposited. This silicon nitride layer works as the bottom layer of the sandwich structure. These three layers were lifted of together. Finally, a 300-nm-thick Ni bond-pad-layer was deposited on top of NiCr for the simplicity of bonding the device ultrasonically. At this point, the bolometer fabrication was completed. The sacrificial layer of polyimide under the bolometer was not removed for the sake of simplicity in device fabrication.

4.2.2 Noise Measurement

To observe the effect of forming gas annealing at different intervals of time on the noise voltage PSD of the devices, the noise PSD was measured before the passivation, at the end of each interval of passivation time tracking individual devices. Four devices namely SSL3, SLT1, SRB4 and SLB1 having resistance of 15 kΩ, 70 kΩ, 65 kΩ and 70 kΩ respectively were tested for this purpose. They were fabricated on same substrate. The noise of the devices was measured inside a shielded probe station in dark to avoid photo generation of carriers. Figure 4.3 shows the schematic of noise measurement setup. A low noise voltage preamplifier, SRS model 560, with a gain of

193 was used to amplify the noise voltage PSD from the device. The metal film resistor R1 in Figure 4.2 was placed in series with the device under test (DUT) to limit the bias current and had a value in the MΩ range. This resistance value was varied to obtain the bias currents (I_b) of 0.85 µA, 0.6 µA, 0.3 µA, 0.1 µA and 42 nA to the bolometer circuit. A NiCd battery of 1.12 Volt was used to provide a low noise bias to the circuit. A Hewlett Packard model 3562A DSA was used to measure the noise voltage PSD and record the spectra. The noise PSD was recorded over the frequency range of 1 Hz to 100 kHz. The current-voltage characteristics were measured by placing the device in dark inside the shielded probe station and using a Hewlett Packard HP 4155B semiconductor parameter analyzer. For devices SLT1, SRB4 and SLB1 the noise voltage PSD was measured before passivation and after 0.5 hour, 1 hour, 2 hours, 3 hours, 4 hours and 8 hours of passivation time. For device SSL3 the noise voltage PSD was measured before passivation and after 2 hours, 3 hours, 4 hours and 8 hours of passivation time.

4.2.3 Forming Gas Passivation

The forming gas passivation of the samples was done by using an AXIC Jet First Rapid Thermal Annealing (RTA) System. The chamber of RTA was evacuated by a roughing pump before starting the passivation to avoid the possible effect of oxidation of the samples. A flow of 500 SCCM of 99.999% pure forming gas was used for the passivation purpose. The temperature inside the RTA chamber was ramped to 250 ^{o}C at a ramp rate of 40 ^{o}C per minute. The samples were kept inside the RTA at 250 ^{o}C for the time period specified in section 4.2.2.

4.2.4 Crystallinity and Atomic Composition Test

To measure the crystallinity and atomic composition of the thermometer before and after forming gas passivation, a 400-nm-thick layer of a-$Si_xGe_{1-x}O_y$ was sputtered on a 2 mm square glass substrate, and then passivated by forming gas for 8 hours under same condition as mentioned above.

A Siemens model D500 θ-2θ diffractometer using Cu K α radiation was used to measure the XRD of the samples. The 2θ angle was varied from 2^o to 120^o. Sharp XRD peaks corresponding to GeO_2 and SiO_2 were observed after the passivation process, indicating that the samples turned into a least partially crystalline during the passivation. Figure 4.4 shows the XRD of a sample annealed for 8 hours. No XRD peaks were observed in the spectra before passivation of the sample indicating that it was initially amorphous. Zacharias et al. [30] reported that annealing did not form crystals of SiGeO:H until an annealing temperature of 300 ^oC for a passivation time of 30 minutes. No XRD peaks of Ge, Si or SiGe were observed after passivation in this case.

The sensing layer's composition was measured by EDX analysis in a JOEL JSM-I6845 scanning electron microscope to observe the oxidation effect of $Si_xGe_{1-x}O_y$ sensing layer during passivation. An accelerating voltage of 20 keV was applied to determine the standard peaks as well as the concentration of each constituent element in the sample. The atomic composition of the $Si_{0.11758}Ge_{0.87}O_{0.0125}$ sensing layer remained same before and after passivation.

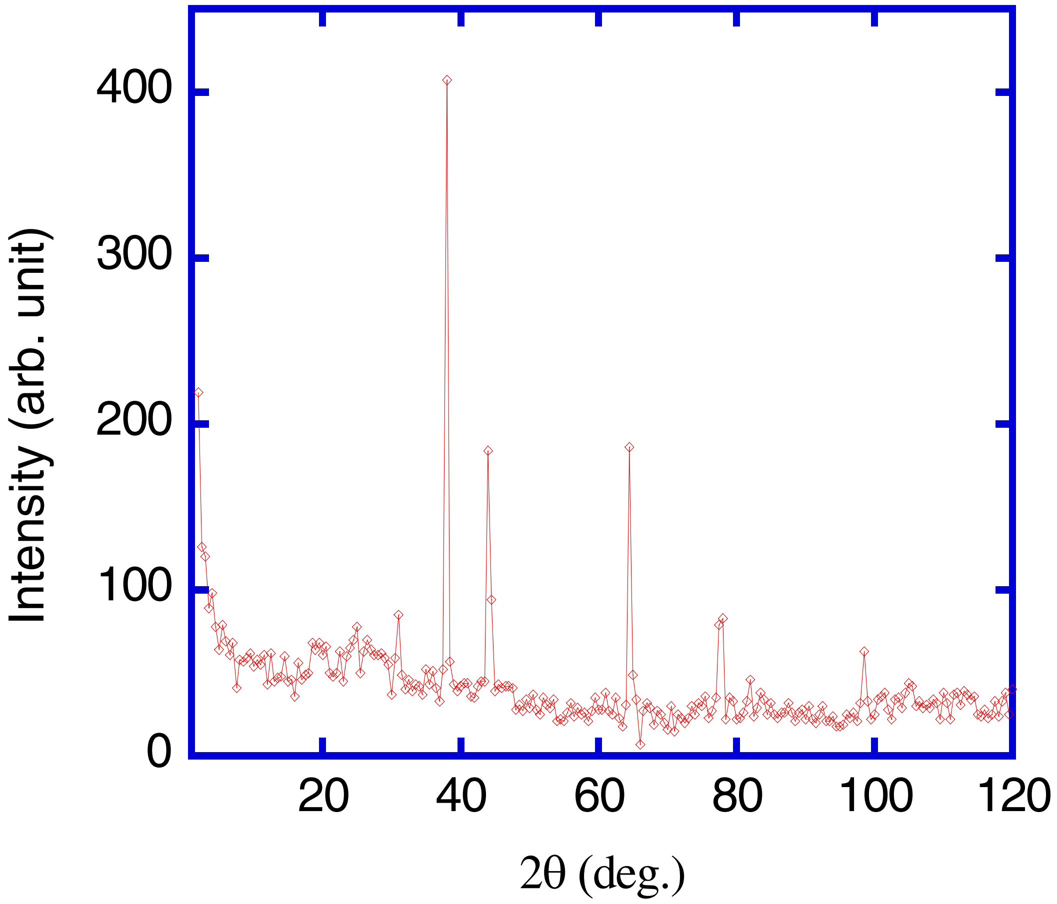

Figure 4.4 X-ray diffraction from $Si_{0.11758}Ge_{0.87}O_{0.0125}$ annealed for 8 hours at 250 ^{o}C in forming gas

4.2.5 Noise Data Analysis

The 1/*f*-noise or flicker noise can be expressed by Hooge's formula

$$S_v = \frac{K_f V_{dc}^{\beta}}{f^{\gamma}} \tag{4.1}$$

where, f^{γ} is the electrical frequency with γ has the value near 1 for 1/*f*-noise and 2 for g-r noise or non-stationary 1/*f*-noise, K_f is the flicker noise coefficient and is equal to α_H/N where, α_H is Hooge coefficient of 1/*f*-noise and N is the number of fluctuators in the sample, V_{dc}^{β} is the dc bias voltage in which β has the ideal value of 2, and S_v is the voltage noise PSD.

The value of β was determined by plotting $\mathrm{LOG}_{10}(S_v)$ versus $\mathrm{LOG}_{10}(I_b)$ using the 1, 5, and 10 Hz frequency data. The value of γ was determined from the slope of S_v in log-log plot at different bias currents in the frequency range of 1 to 10 Hz. From the equation of trend line the average value of γ was determined from four bias currents. The value of K_f was determined by using (4.1) at each bias current, and their average was taken to determine the final value of K_f as the measure of flicker noise. The values of K_f, γ, and β for different devices at different conditions are shown in Table 4.1

4.3 Results and Discussions

Different types of noise may be present in semiconductors [31]. The *I-V* characteristics of the devices before and after passivation are found to be linear. This implies that there is no potential barrier in the metal-semiconductor junctions, eliminating the possibility of shot noise [1].

The values of K_f were found to be decreasing as the passivation time was increased, as a result of the reduction in 1/*f*-noise. For the longest passivation time (480 minutes), the values of K_f were found to increase slightly with devices SRB4, SLT1, and SLB1. For cases like device SLT1, the value of K_f was increased from 4.81×10^{-9} to 1.10×10^{-8} as the passivation time increased from 60 to 120 minutes. The probable reason for this was the increase in the value of β. The average value of γ for all the devices was found to be between 0.96 to 1.25, indicating classic frequency dependence for the 1/*f*-noise.

Figure 4.5 shows the noise voltage PSD for SLB1 at 0.3 μA bias current at different passivation times. Noise sources in the bolometer are mainly due to the sensing layer of $Si_xGe_{1-x}O_y$, because as discussed in chapter two. Similar noise values for the thin films of $Si_xGe_{1-x}O_y$ or Si_xGe_{1-x} sputtered on glass substrates were obtained.

The noise spectra measured before the passivation shown in Figure 4.5 do not display thermal noise over this frequency range due to the presence of high level of 1/*f*-noise. The g-r noise has a Lorenzian spectrum and is white below a characteristics frequency and drops as f^2 above this frequency [32]. The presence of trapping states in the sensing layer is probably the greatest source of g-r noise [31]. The origin of 1/*f*-noise is still a debate. The value of α_H from Hooge relationship depends on the quality of the crystal and on the scattering mechanisms that determine the mobility μ [31]. 1/*f*-noise can also be attributed to the trapping and detrapping of carriers with a distribution of time constants [33]. The mobility on the other hand depends on the defects in the materials. From Figure 4.5 it can be seen that there is a sudden increase in the noise level after 100 Hz and also increase in the value of γ to 2.39 in the frequency range of 1 kHz to 10 kHz for before passivation case as compared to the value of 1.09 in the frequency range of 1 Hz to 10 Hz. The higher slope of the noise curve before and after 0.5 hour passivation is characterized by combination of 1/*f*-noise and g-r noise because of the fluctuation of electrons between the conduction band and the traps [31]. These two combined noise mechanisms dominate over the Johnson noise before passivation. For other passivated times, as the passivation time goes the reduction of trapping states or defects by hydrogen atom caused the electrical noise to be reduced.

After one, two, and three hours of passivation time, the noise spectra does not have any flat portions in the frequency range of 1 Hz to 10 kHz indicating the absence of Johnson noise. Probably for these conditions the g-r noise and 1/*f*-noise are dominated over Johnson noise.

After 4 hours and 8 hours of passivation we measured noise spectra that display Johnson noise above 100 Hz. However, between the frequency range 1-100 Hz the spectra is still dominated by 1/*f*-noise. The other three devices behaved similarly. Some of the potential sources of 1/*f*-noise are defect related. In the case of the largely amorphous $Si_xGe_{1-x}O_y$ thin film, a large number of defects can be present. According to Clement et al. [19] and Ahmed et al. [18], $Si_{1-x}Ge_xO_y$ consists of both Si-O and Ge-O bonds formed by non-equilibrium thermodynamic state from the glow discharge in the sputtering process. It is also possible to have some non-reacted Ge and Si and Si-Si, Ge-Ge, Si-Ge bonding with this low atomic percent of oxygen [34].

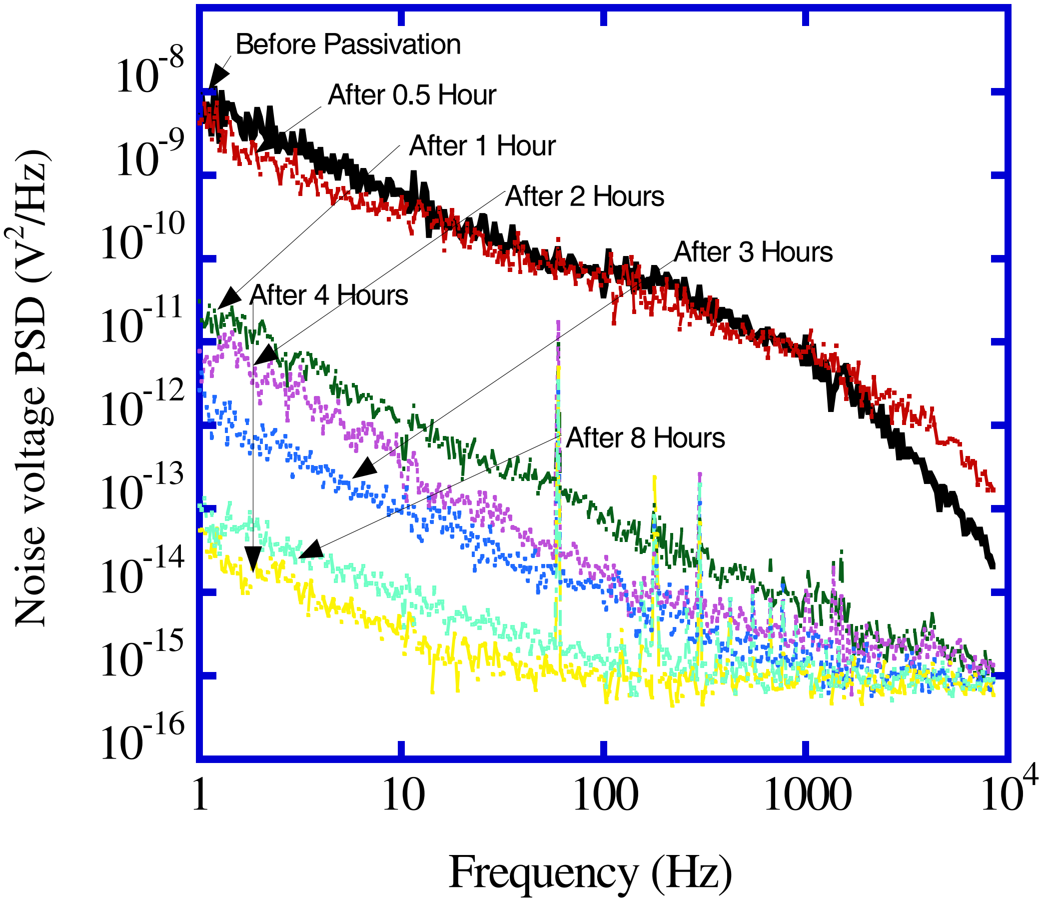

Figure 4.5 Noise voltage PSD of device SLB1 at different interval of passivation time for 0.3 μA bias current

Table 4.1 Variation of Noise Parameters in Different Devices with Different Passivation Time

Device	Noise Parameter	Passivation Time (Min)						
		0	30	60	120	180	240	480
SRB4	K_f	5.89×10^{-8}	2.53×10^{-08}	1.19×10^{-10}	1.50×10^{-09}	7.94×10^{-09}	5.54×10^{-11}	9.51×10^{-11}
	β	1.18	2.14	1.44	1.65	2.00	1.42	1.75
	γ	1.06	1.13	1.19	1.03	1.01	1.10	1.01
SLT1	K_f	1.61×10^{-06}	1.47×10^{-07}	4.81×10^{-09}	1.10×10^{-08}	5.03×10^{-11}	2.85×10^{-11}	8.76×10^{-11}
	β	1.50	1.39	1.70	2.38	1.30	1.52	1.31
	γ	1.12	1.19	0.97	1.15	1.01	0.96	1.01
SSL3	K_f	2.27×10^{-06}			1.18×10^{-05}	1.25×10^{-07}	1.02×10^{-08}	1.66×10^{-09}
	β	1.90			2.64	1.97	1.71	1.41
	γ	1.15			1.33	1.19	1.08	1.01
SLB1	K_f	7.54×10^{-07}	2.85×10^{-05}	1.04×10^{-08}	5.69×10^{-09}	1.89×10^{-11}	8.84×10^{-12}	2.21×10^{-10}
	β	1.26	2.17	1.78	1.89	0.90	1.22	1.78
	γ	1.09	1.25	1.11	0.96	1.20	0.94	1.01

The bonding of Si with the oxygen can have one major type of charge trap-E′-type paramagnetic defect [35], [36], [37]. This type of defect center consists of a $.Si{\equiv}O_3$ unit in which the . symbol represents an unpaired electron with a silicon dangling bond [38]. For SiO_x bonding ($0<x<2$), Si dangling-bond centers are defined by $.Si{\equiv}SO_2$, $.Si{\equiv}Si_2O$, and $.Si{\equiv}Si_3$. In our structure we have SiN layer underneath the $Si_xGe_{1-x}O_y$ layer which could serve as a passivation layer for $Si_xGe_{1-x}O_y$ [39]. We consider the existence of Pb-type of defects at the SiN-$Si_xGe_{1-x}O_y$ interface. It is well believed that the atomic N does not react with SiO_2 spontaneously [40], which may explain the lack of passivation by the SiN. Similar dangling bond of Ge ($.Ge{\equiv}O_3$) can exist for Ge-O or Ge-Ge bonding [41].Si-Ge bonding has a lattice mismatch between them and could produce stress in the films of Si-Ge although the authors did not notice this in the present work. It was found by XRD that the Si-Ge-O films were amorphous and lacked long range order. The lack of order indicates the presence of dangling bonds. There also presents recombination centers in the Si-Ge bonding structure [42]. They found that this recombination center is located close to the midgap of the CVD deposited $Si_{0.9}Ge_{0.1}$ for solar cell. By hydrogen passivation they found that the defect center concentration reduced by an order of a magnitude. According to Johanson et al. [43], due to the presence of large number of localized states in amorphous semiconductors, the generation-recombination noise model can be used to explain the conductance fluctuations. Localized traps reduce the conductance. The traps at a single energy level produce a Lorenzian noise spectrum according to relation mentioned in (4.2)

$$S(\omega)\alpha\frac{1}{1+\frac{\omega^2}{\omega_0^2}} \tag{4.2}$$

where, ω_0 is the sum of trap and release rates with deeper states having lower ω_0. A distribution in the trapping time constants can lead to a 1/*f*-noise spectra [33]. The trap centers in the SiGe alloy are located close to the midgap [42]. The presence of the deep traps tends to contribute to the noise spectrum at lower frequencies because of the lower values of ω_0 (long time constants). In addition, the metal semiconductor contacts may cause a noise contribution for the sandwich structure of the bolometer used here [43]. Since we have only one type of bolometer structure here (sandwich) so direct comparison of noise voltage PSD due to geometry of the device was not possible. It can be seen from Figure 4.5 that as the passivation time progressed, the electrical noise decreased through 4 hours of passivation time, clearly indicating the passivation of dangling bonds in the sensing layer. It is believed that the hydrogen effectively passivated the defects at the grain boundaries and thus reduced the recombination centers. According to Uchino et al. [37], the surface silicon atoms of the clusters are terminated by the hydrogen atoms to saturate the dangling bonds. S. Honda et al. [44] reported to have an increment in carrier mobility for their poly-Si films annealed in hydrogen, but in this case the authors did not notice significant change in the device resistance for different annealed conditions. However, the electrical noise and the value of the flicker noise coefficient K_f increased for some devices after 8 hours of passivation as compared to 4 hours of passivation as can be seen from Figure 4.5 and Table 4.1. The reason for this may be defects caused by hydrogen, in addition to hydrogen passivation of dangling bonds [45]. According to S. N. Rashkeev et al. [45], there are several significant behaviors associated with hydrogen at the Si-SiO_2 interface. For this case it is believed that:

1) Hydrogen passivates the dangling bonds at the interface, at the grain boundaries, and in the oxide via the reaction

$D + H \rightarrow SiH$ for Silicon, or

$D + H \rightarrow GeH$ for Ge

where, D is the Dangling bond and SiH and GeH are the Si-H and Ge-H bonds respectively.

2) H^+ arrives from the forming gas at the interface and after gathering one electron from the Si it passivates to SiH and if it encounters an SiH bond it depassivates through reaction

$SiH + H \rightarrow D + H_2$ for Silicon

A similar argument can be made for germanium.

So excess hydrogenation could be reason for increasing the number of dangling bonds as well as the electrical noise in this case.

The increase in the value of α_H/N after 30 minutes of passivation as compared with the as grown in sample SLB1 is probably due to the increase of the value of β, although we see from Figure 4.5 that the noise level remains same after 30 minutes of passivation.

4.4 Conclusions

Forming gas annealing was performed on $Si_xGe_{1-x}O_y$ microbolometers in order to reduce the electrical 1/*f*-noise. The value of flicker noise coefficient K_f, or α_H/N from the Hooge model was used as a measure of electrical 1/*f*-noise. The 1/*f*-noise is believed to originate from the defects and dangling bonds in the sensing layer. The hydrogen passivation leads to repair the dangling bonds and defects, thus played a role in reducing the electrical 1/*f*-noise. As the passivation time increased, the 1/*f*-noise decreased leading the hypothesis of reducing the number of dangling bonds with passivation time. The dangling bonds contribute to trap states and scattering centers for the carriers which lead to the production of 1/*f*-noise. It was found that the passivation done for excess time increased the electrical 1/*f*-noise of the device slightly.

CHAPTER 5

HIGH RESPONSIVITY a-$Si_xGe_{1-x}O_y$:H MICROBOLOMETER

5.1 Introduction

Silicon and its compounds had become attractive materials for microbolometers operating at room temperature [7], [13], [46], [47]. Both poly silicon germanium [3], [48], [49] and amorphous silicon germanium [14] had been used in microbolometers as the sensing material. Comparatively new in the family of silicon germanium, amorphous silicon germanium oxide (a-$Si_xGe_{1-x}O_y$), has the potential to be used in microbolometers operating at room temperature. It forms an Ohmic contact with metals of low thermal conductivity like NiCr which results in high responsivity and detectivity.

In this chapter, fabrication, characterization, and challenges faced during fabrication of a-$Si_{0.15}Ge_{0.85}O_{0.0236}$:H microbolometers were described. To reduce 1/*f*-noise and obtain better performance, the bolometers were passivated by using forming gas.

5.2 Experimental Details

5.2.1 Bolometer Fabrication

Two types of bolometers were fabricated. For the first type, Ni was used as the contact metal between NiCr electrode arm and a-$Si_xGe_{1-x}O_y$ sensing layer. For the second type, the NiCr electrode arm served as the contact metal to a-$Si_xGe_{1-x}O_y$ sensing layer. Figure 5.1 (a) (Device 19C1a and 19C1b) and 5.1 (b) (Device 21B1a and 21B1b) show the

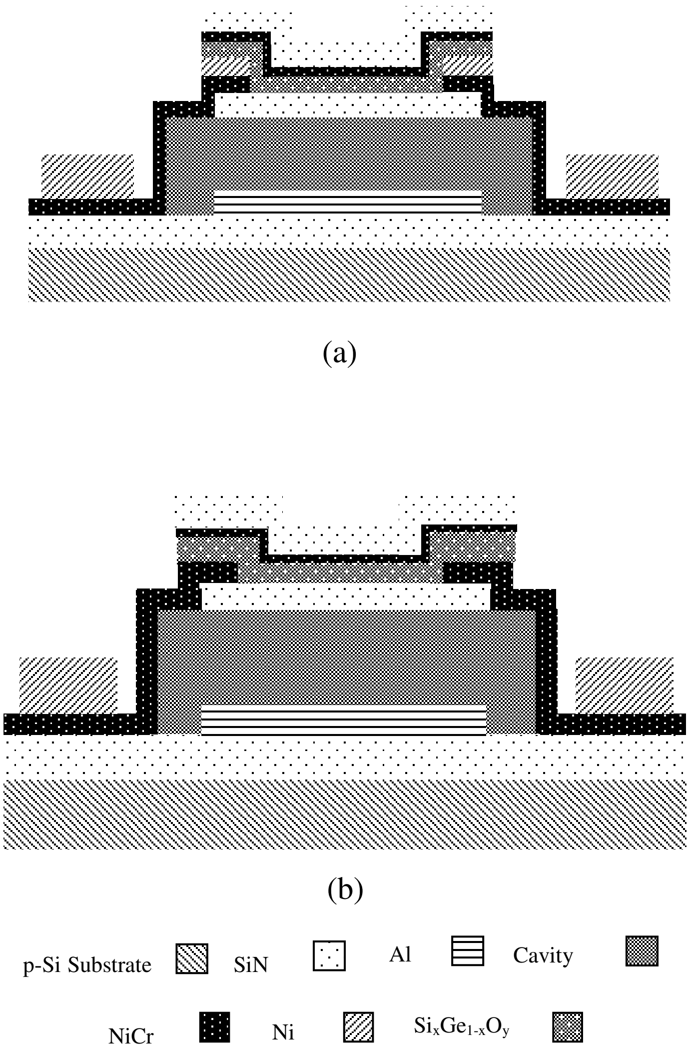

Figure 5.1 Cross section of a-Si$_{0.15}$Ge$_{0.85}$O$_{0.0236}$:H microbolometer with (a) Ni contact (b) NiCr contact

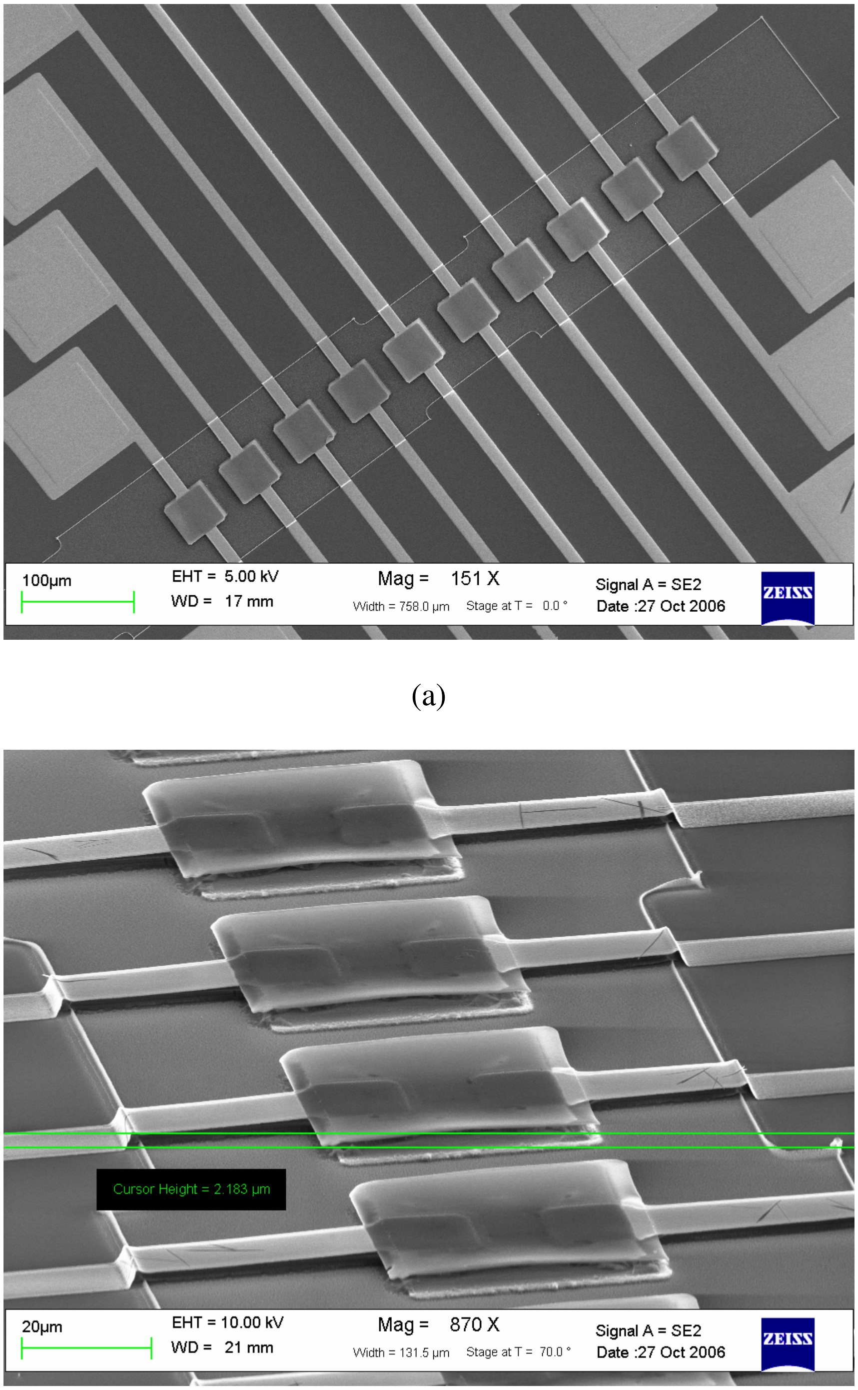

(a)

(b)

Figure 5.2 SEM micrograph of suspended $40 \times 40\ \mu m^2$ microbolometers arrays after surface micromachining (a) 10×10 array of microbolometers (b) closer view of microbolometers cross sectional view of the two types of fabricated devices by using NiCr contact and Ni contact respectively. The fabrication procedure and forming gas passivation technique for both types of devices are same as mentioned in section 4.2. After passivation, the microbolometers were ashed in a low pressure oxygen plasma to remove the polyimide sacrificial layer and suspend the thermometer above the substrate. During this process of surface micromachining, the temperature inside the asher was kept < 50 ^{o}C in order to avoid stress caused by heat. The suspended microbolometers are shown in Figure 5.2 (a) and 5.2 (b).

5.2.2 Bolometer Characterization

A small piece of the wafer containing the micromachined microbolometers was mounted on a ceramic package for characterization. Device 21B1b was ultrasonically wire bonded with Al wire while devices 19C1a, 19C1b, and 21B1a were bonded by indium with Al wire attached to it. TCR was calculated by using the formula mentioned in (5.1)

$$\alpha = -\frac{E_a}{k_B T^2} \tag{5.1}$$

The thermal conductivity of the device was measured by the Joule heating method mention in section 3.3.

The voltage responsivity of the bolometer was calculated by using (1.16) from the ratio of output power from the detector to incident power from a black body source heated at 1173 K. For calibration purposes, an Oriel 70124 pyroelectric detector with a responsivity of 1000 V/W was used. The ZnSe window of the cryostat served as the filter of IR radiation at long wavelengths, having a cutoff of 15 μm. A 2.5 μm long pass filter was used between the detector and IR source providing a short wavelength cutoff. For these devices, an abrupt change in device resistance was observed while illuminated by a microscope light. This characteristic suggests the presence of a high photo-generation rate. To avoid photo generation of carriers in this specified wavelength range, 2.5 μm long pass filter was used. The device was biased at different bias currents and the signal from the device was amplified by a Stanford Research Instruments model SR560 voltage preamplifier. The noise spectra and signal from the microbolometer were recorded at different modulated frequencies with the help of a Hewlet Packard, model HP3562 dynamic signal analyzer.

The thermal time constant, τ_{th}, was determined from the cutoff frequency of the responsivity versus chopper frequency characteristic. The thermal mass, C_{th}, was calculated from the values of thermal conductance and thermal time constant. The absorption coefficient was calculated from the low frequency responsivity by using (1.12).

For calculating detectivity, and NEP formulas mentioned in (1.17), and (1.18) were used respectively. For calculating NETD formula mentioned in (1.19) was used. For this purpose, *f*/1 optics arrangement was assumed. The values of transmittance and $(\Delta P / \Delta T)_{\lambda_1 - \lambda_2}$ assumed to be 0.9 and 2.6×10^{-4} W/cm^{2}K respectively.

5.3 Results and Discussions

The characterization results for different microbolometers are listed in Table 5.1. The resistance and TCR versus temperature characteristics for microbolometer 21B1b are shown in Figure 5.3. The TCR for this device was calculated to be -4.77%/K with a corresponding activation energy of 0.3576 eV at 295K. Other microbolometers fabricated showed similar values of TCR with a pixel resistance between 320 to 743 kΩ. The high TCR resulted from higher activation energy associated with the a-$Si_xGe_{1-x}O_y$ transport. Similar TCR values were obtained by using similar atomic composition of a-$Si_xGe_{1-x}O_y$ thin films mentioned in chapter 2. Evidently, it seems that forming gas passivation did not affect the TCR value of the material.

The *I-V* characteristic from device 19C1a is shown in Figure 5.4. It can be seen that the microbolometer has linear *I-V* characteristics. The slight nonlinearity in Figure 5.4 is due to the effect of Joule heating. All other microbolometers characterized had shown similar linear *I-V* characteristics.

The thermal conductance, G_{th}, of device 19C1b was found to be 4×10^{-8} W/K. Figure 5.5 shows the determination of thermal conductance for device 19C1b. This low value of thermal conductance indicates a good thermal isolation between the detector pixel and substrate. The responsivity and detectivity versus chopper frequency are plotted in Figure 5.6 for device 21B1b with 2.5 μm filter placed between the microbolometer and the black body source. The highest responsivity obtained with this device was 5.68×10^{3} V/W while device 19C1b showed a highest responsivity of 1.05×10^{4} V/W. The decrease in responsivity with increasing chopper frequency agrees with (1.16), indicating bolometric behavior. This high value of voltage responsivity with such value of moderate pixel resistance (743 kΩ) for device 19C1b was resulted from the combined effect of low thermal conductivity, high TCR, use of Al mirror and the absorber material.

The detectivity was calculated from the measured responsivity and the measured electrical noise at different chopper frequencies. The highest value of detectivity was obtained from device 19C1b. This detectivity value was 8.27×10^6 cm-Hz$^{1/2}$/W. Even though the bolometers were passivated by forming gas to reduce the electrical noise, significant 1/*f*-noise was still present degrading the performance of the microbolometers. Devices 19C1a and 19C1b were passivated by forming gas for seven hours while devices 21B1a and 21B1b were passivated for six hours. The detectivity value of 19C1a is four times higher than that of device 21B1b indicating the 1/*f*-noise for the seven hours case is lower than that for the six hours case. Figure 5.7 shows the signal at 9 Hz and the noise voltage PSD for microbolometer 21B1b at 1066 nA bias current. Careful observation of this noise spectrum would lead to the fact that there is no presence of Johnson noise. It is apparent that 1/*f*-noise limited performance is the main cause of deceased detectivity for this case. Further investigation is needed to reduce the 1/*f*-noise and hence improve the detectivity. One of the alternatives could be performing the hydrogen passivation while the sensing layer is growing. CVD deposition of the $Si_xGe_{1-x}O_y$ would be one way of accomplishing this process.

Without placing the 2.5 μm long pass filter between the device and the blackbody source, the detectors behaved like a photo conductor as seen from Figure 5.8 for device 21B1b. Both the responsivity and the detectivity were found to be increased at least by an order of magnitude and the responsivity values remained almost constant with respect to chopper frequency. While filtering out the radiation below 2.5 μm of wavelength, the $Si_xGe_{1-x}O_y$ microbolometers produced a bolometric behavior as evident by the attenuation due to the thermal time constant.

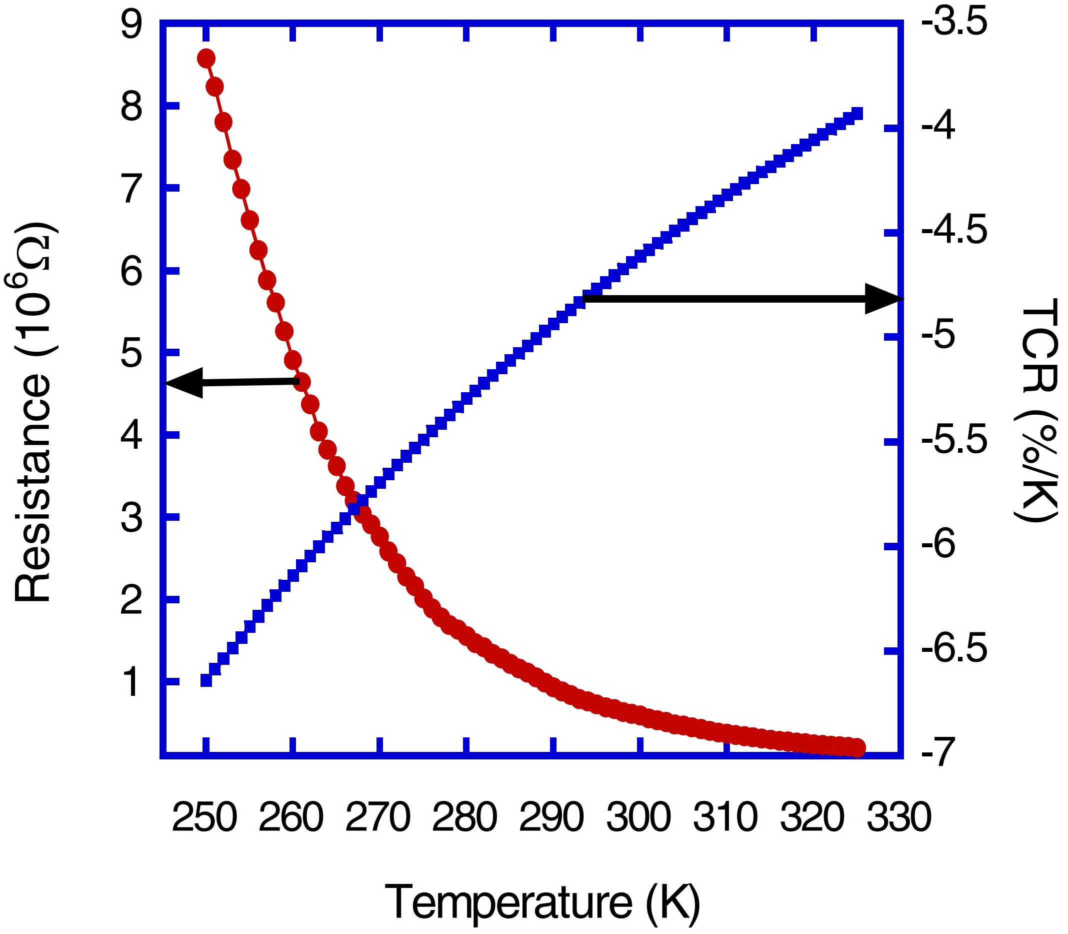

Figure 5.3 Variations of resistance and TCR at different temperature for 21B1b

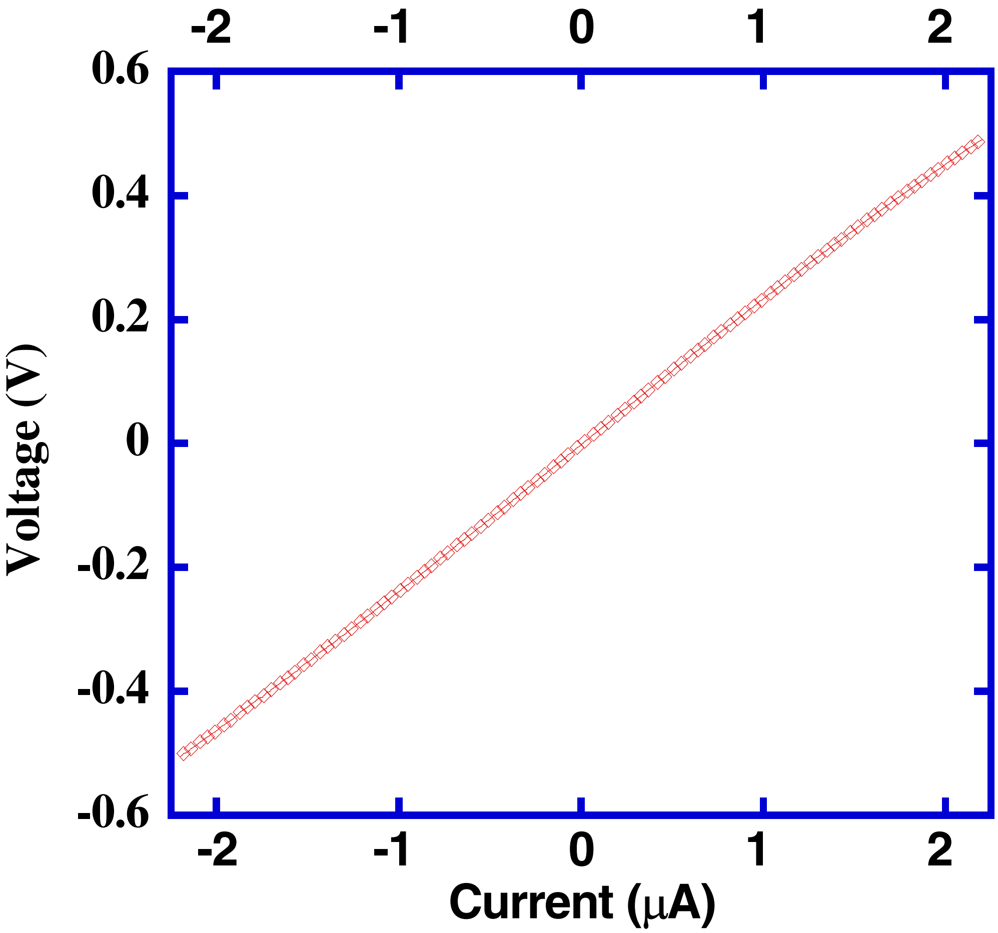

Figure 5.4 *I-V* characteristic from device 19C1a

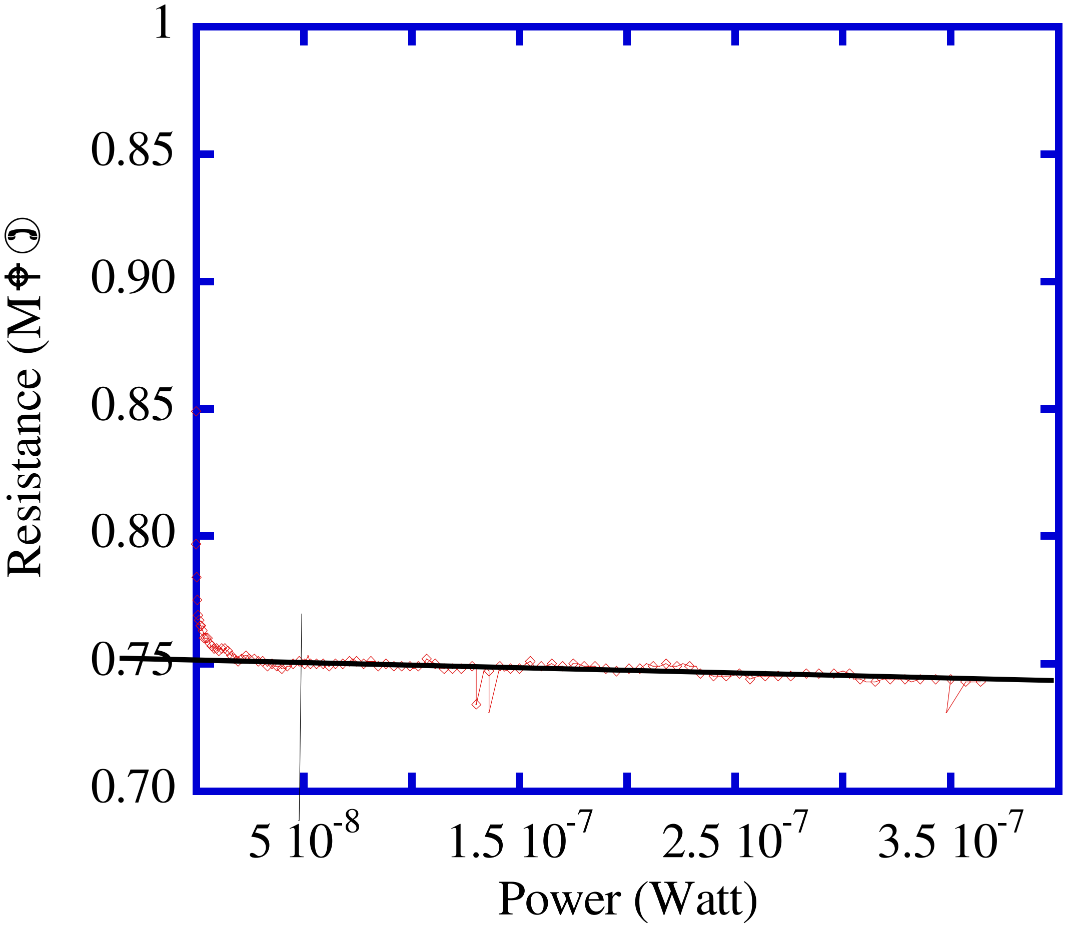

Figure 5.5 Determination of thermal conductivity by Joule heating method

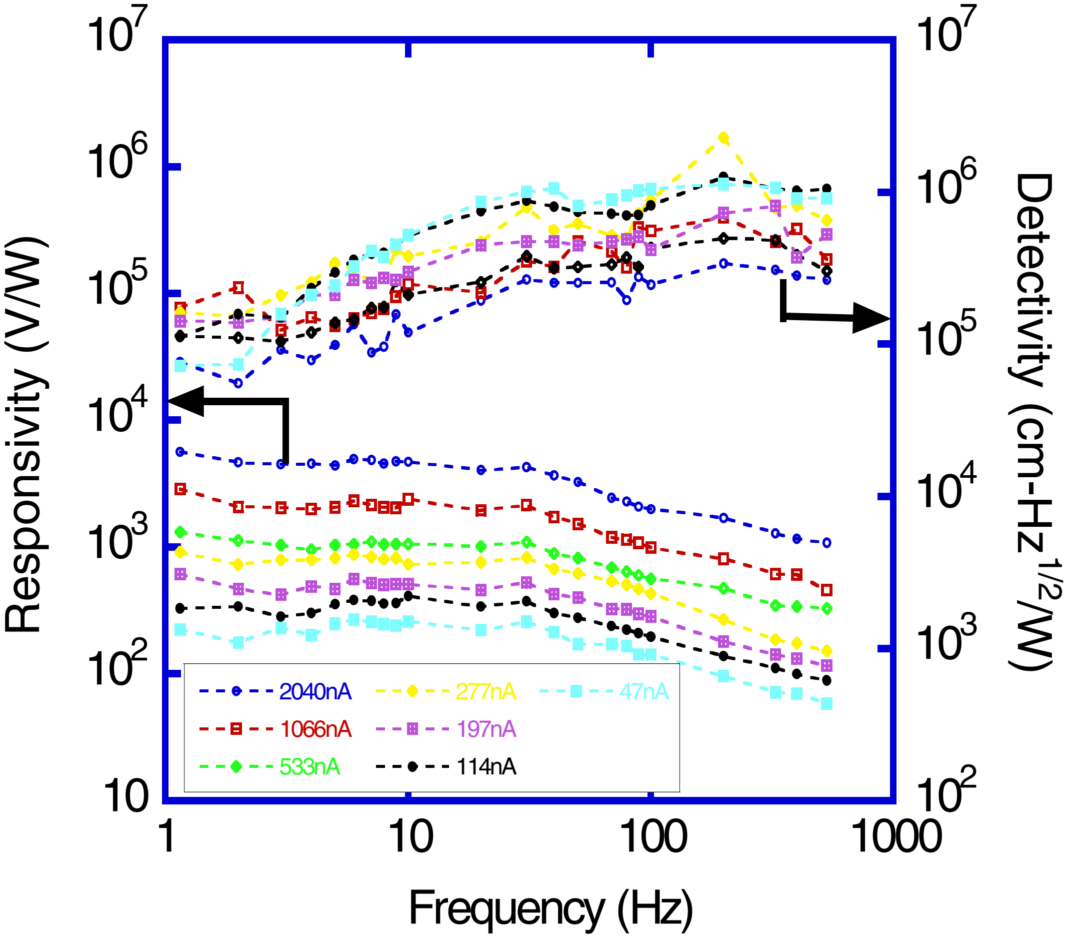

Figure 5.6 Variations of responsivity and detectivity at different chopper frequencies for device 21B1b with 2.5 μm long pass filter placed in front of the device

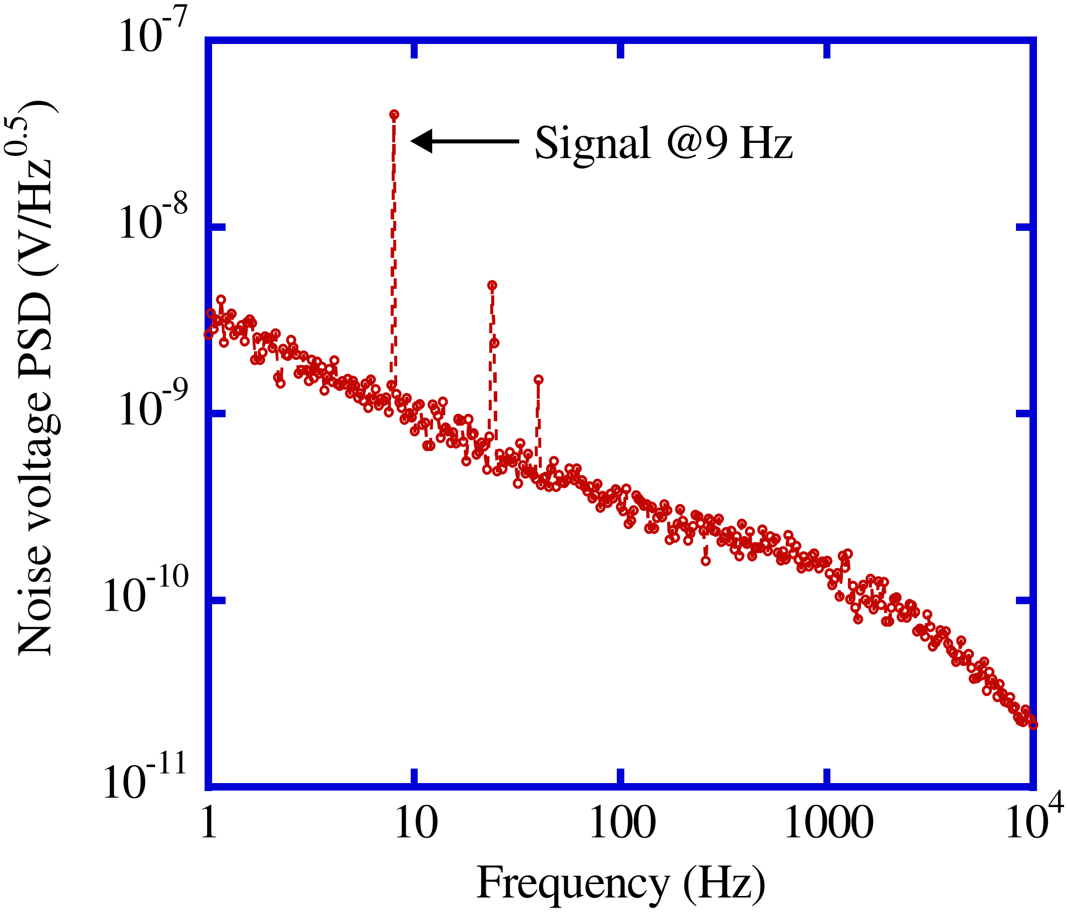

Figure 5.7 Noise voltage PSD of device 21B1b with signal modulated at 9 Hz

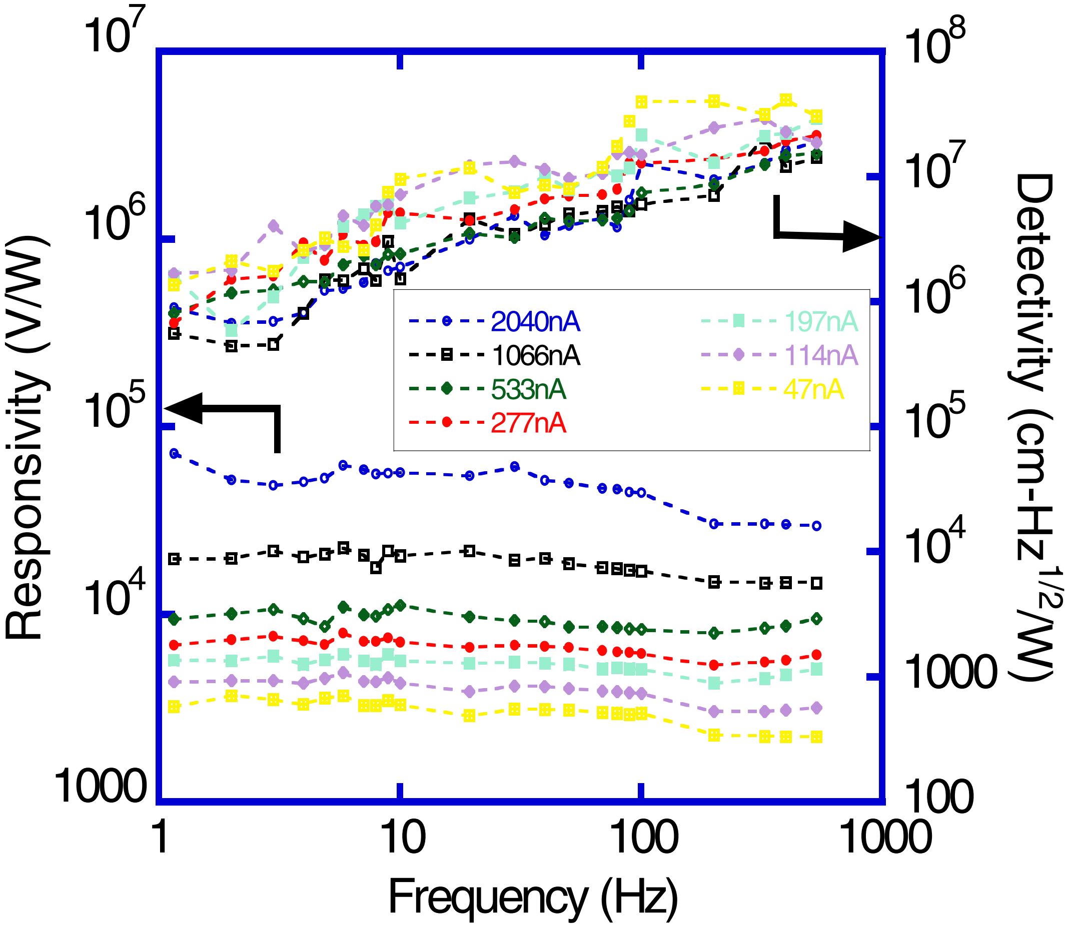

Figure 5.8 Variations of responsivity and detectivity for device 21B1b in vacuum

Table 5.1 Measured Figures of Merits of Different $Si_xGe_{1-x}O_y$ Microbolometers

Device number	21B1a	21B1b	19C1a	19C1b
Device resistance (KΩ)	575	630	320	743
Contact metal with thermometer	Ni	Ni	NiCr	NiCr
Passivation time (Hour)	6	6	7	7
Activation energy, E_a	0.3227	0.3576	0.3502	0.3601
TCR, β (-%/K)	4.23	4.77	4.67	4.80
Responsivity, R_v @ 2 μA bias current (V/W)	-	5.68×10^3	9.89×10^3	1.05×10^4
Detectivity, D^* ($cmHz^{1/2}/W$)	-	2.28×10^6	3.15×10^6	8.27×10^6
Thermal conductance, G_{th} (W/K)	-	-	5.88×10^{-8}	4×10^{-8}
Thermal time constant, τ_{th} (ms)	-	5.90	5.18	3.44
NEP ($W/Hz^{1/2}$)	-	1.75×10^{-9}	1.27×10^{-9}	4.84×10^{-10}
NETD in 8-14 μm wavelength (mK)	-	1838	1345	513
Thermal capacitance, C_{th} (J/K)	-	-	3.04×10^{-10}	1.38×10^{-10}
Absorption coefficient, η	-	-	0.13	0.525

The lowest NEP was found to be 1.38×10^{-10} $W/Hz^{1/2}$ from device 19C1b, A higher NEP value resulted from device 21B1b due to the lower value of detectivity.

The thermal time constant measured from the responsivity versus chopper frequency characteristic, was 3.44 ms for 19C1b. It can be further reduced by reducing the electrode arm width (currently 10 μm), although the obtained value can be used with current frame rate of IR cameras available for commercial applications.

The highest absorption coefficient was found 0.525 for device 19C1b. The NiCr absorber layer deposited has a thickness of 10 nm which is expected to result in the absorption coefficient near about unity [27]. Exposing this layer in oxygen plasma for about ten hours during the surface micromachining process could cause oxidation in that layer and thus increase in the sheet resistance. However, the sheet resistance of this layer was not measured before and after the oxygen plasma ashing, and this needs to be investigated further to improve the detector performance.

The lowest NETD value obtained was 513 mK. Lower detectivity caused the value of NETD to be increased.

Comparisons of detectivity figure of merit can be done to the temperature fluctuation noise limited detectivity, background noise limited detectivity, and Johnson noise limited detectivity. The temperature fluctuation noise limited detectivity is expressed by (5.2) [50]

$$D_{TF}^{*} = \sqrt{\frac{\eta^{2} A_{d}}{4 k_{B} T^{2} G_{th}}} \tag{5.2}$$

The background noise limited detectivity is expressed by (5.3) [50]

$$D_{BG}^{*} = \sqrt{\frac{\eta}{8 k_{B} (T^{5} + T_{B}^{5}) \sigma}} \tag{5.3}$$

where, T_B is the temperature of the blockbody, 1173 K in this case.

On the other hand, if the detectivity is limited by the Johnson noise, then the expression for detectivity can be obtained by substituting the value of Johnson noise voltage ($V_j = \sqrt{4k_B TR\Delta f}$) into (1.16)

$$D_{J}^{*} = R_{v} \sqrt{\frac{A_{d}}{4 k_{B} T R}} \tag{5.4}$$

Using the values mentioned in Table 5.1 for device 19C1b, and assuming the room temperature as 295 K, the temperature fluctuation noise limited detectivity can be

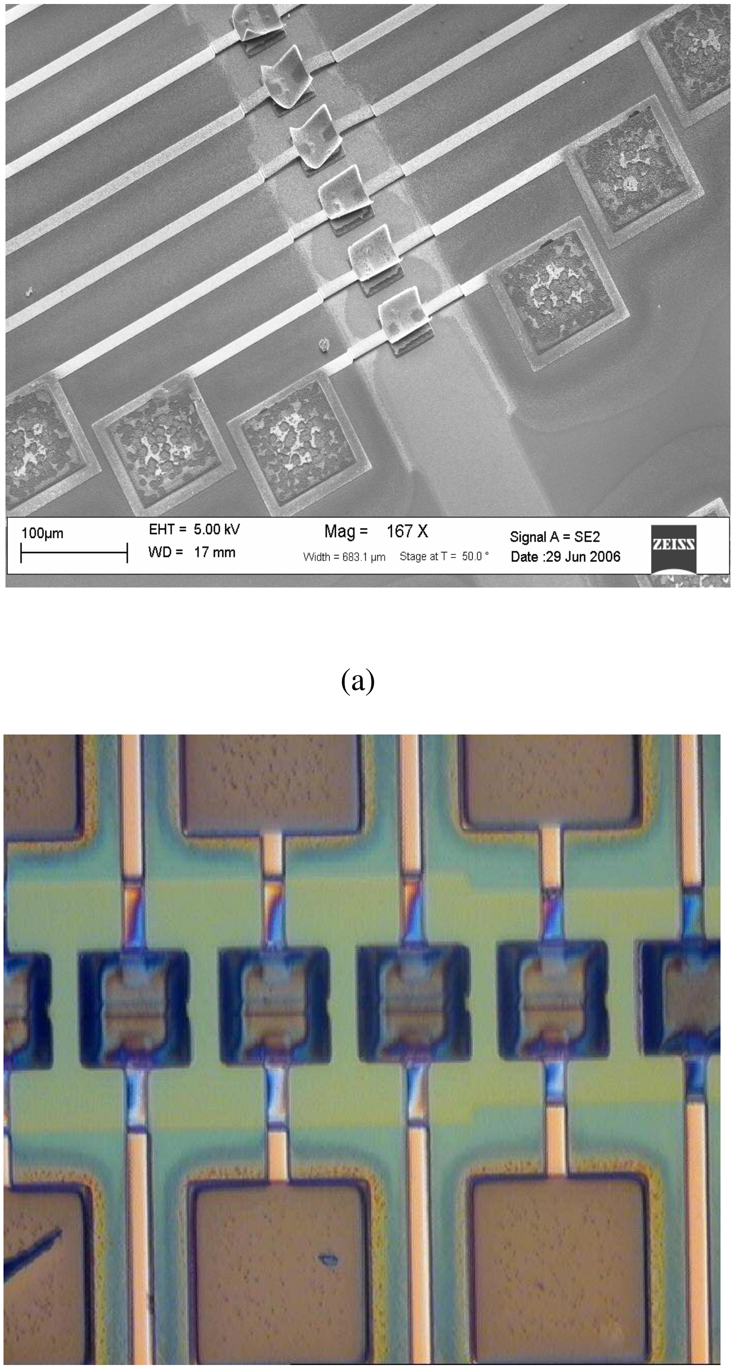

(a)

(b)

Figure 5.9 Curled sandwich structure detector's array after ten hours of ashing. Partially etched bond pads are seen clearly (a) SEM picture (b) optical microscope picture calculated to be 4.8 × 10^9 cm-$Hz^{1/2}$/W. The Background noise limited detectivity can be calculated to be 6.14 × 10^8 cm-$Hz^{1/2}$/W. Where, the Johnson noise limited detectivity can be calculated to be 7.60 × 10^8 cm-$Hz^{1/2}$/W at 2 μA bias current. Measured detectivity is lower than these values indicating the presence of higher noise value. These values of detectivity will improve the values of NEP and NETD significantly and is higher than any current reported values for Si_xGe_{1-x} compounds as compared to the pixel size and resistance [14], [17].

5.4 Challenges Faced in Fabricating Microbolometers

Suitable atomic compositions of $Si_xGe_{1-x}O_y$ films to be used for microbolometer applications have moderate to high resistivity. The use of top absorber layer let the current flow from one electrode through the sensing layer then through absorber and sensing layer to another electrode in a microbolometer. For sensing layer thickness of 400 nm, the device resistance was very high (> 120 MΩ). While sensing layer thickness was made 200 nm, the device resistance was found < 1 MΩ before ashing. After ashing, most of the devices were found open circuited and a few of them had a resistance value of > 120 MΩ. After inspecting in SEM, the sensing layer was found to be warped and curly as seen in Figure 4.3, most likely because of the less thickness. The increase in the pixel resistance is believed to be from the oxidation of sensing layer while ashing the device for about ten hours. In order to eliminate these problems, the sandwich layer of silicon nitride was used. Silicon nitride was used underneath the electrode arm and on top of absorber layer to protect the sensing layer from oxidation and to add mechanical strength to the thin layer pixel. This time almost all of the detectors found open circuited after micromachining. In this case, the detectors are suspended and found with minimal stress. Figure 5.9 (a) and 5.9 (b) show the microscopic and SEM pictures of the detectors after ashing. The change in color of silicon nitride layer and nickel bond pads was investigated. By EDX analysis on these areas, the presence of fluorine was found. This residual fluorine in the reactive ion etching chamber (used to ash the sample) is believed to come from CF_4/SF_6 gas. This fluorine produces HF by reacting with moisture present in the ambient environment at room temperature. HF partially etched the silicon nitride and Ni layers. This caused the whole sandwich layer to be stressed and curled. This problem was solved by ashing the devices in a new asher dedicated only for using ashing purpose.

5.5 Conclusions

Microbolometers of a-$Si_{0.15}Ge_{0.85}O_{0.0236}$ fabricated using a complimentary metal oxide semiconductor compatible process. A high TCR with high activation energy was achieved. Although the detectors were passivated by forming gas, but 1/*f*-noise could not be eliminated to a satisfactory level. The presence of 1/*f*-noise degraded detector performance. Photo generation of carriers was observed below 2.5 μm wavelengths. A good thermal isolation was obtained by using sacrificial polyimide layer which resulted in a thermal conductivity as low as 4×10^{-8} W/K. Investigation is needed to reduce the presence of high noise in a-$Si_{0.15}Ge_{0.85}O_{0.0236}$ sensing layer and to increase the detectivity of the bolometers.

CHAPTER 6

FABRICATION AND CHARACTERIZATION OF CAVITY BASED FABRY-PEROT MICROSPECTROMETER

6.1 Introduction

An infrared spectrometer measures the properties of light in the infrared part of the electromagnetic spectrum. These properties of light can be light intensity, polarization etc. over a certain portion of electromagnetic spectrum. Usually, the measured properties vary with frequency. A spectrometer is used in spectroscopy for measuring wavelengths and intensities. Spectrometer is a term that is applied to instruments that operate over a very wide range of wavelengths, from gamma rays and X-rays into the far infrared. In general, any particular instrument will operate over a small portion of this total range because of the different techniques used to measure different portions of the spectrum. Below optical frequencies (that is, at microwave, radio, and audio frequencies), the spectrum analyzer is a closely related electronic device.

Cavity based Fabry-Perot microspectrometer was fabricated and characterized using the constructive interference property of light. Constructive interference property of light wave employs addition of light waves by adding both their magnitude and phase. Fabry-Perot principle is used for sound waves, light waves to form infinite number of reflections of that wave. For this purpose, a tube like wall is used to form the reflection.

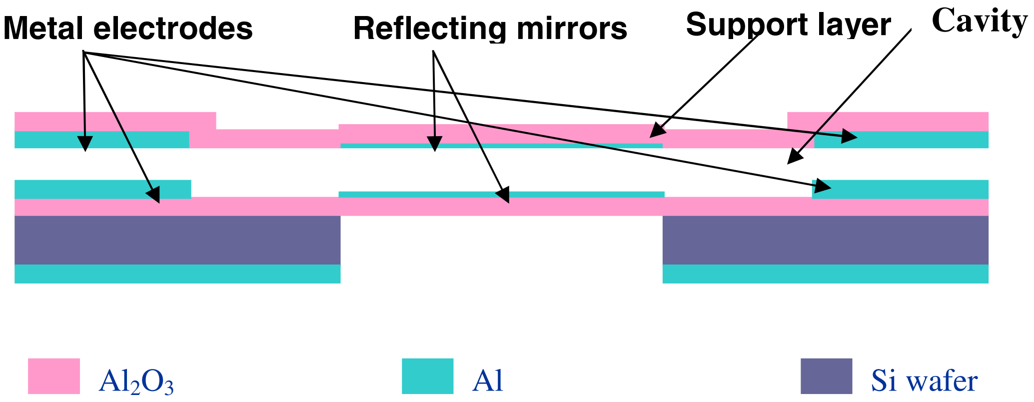

Figure 6.1 Cross section of a cavity based Fabry-Perot microspectrometer
(From reference 59, reprinted after the permission of author)

For this case, a partially transparent and partially reflective layer is used to form the walls where light wave can be passed and reflected inside the tube. If two of the walls are separated by a distance Δx, then for maximum constructive interference

$$\nabla x = (2n+1)\frac{\lambda}{2} \tag{6.1}$$

and for maximum destructive interference

$$\nabla x = (n+1)\lambda \tag{6.2}$$

where, n = 0,1,2,3,4…… and λ is the wavelength. The simulation for structural design, optical properties of the device as well as the actuation mechanism of Fabry-Perot cavity based spectrometer is done in previous work [51]. The current work is the continuation from there and its objective is to fabricate and test the microspectrometer.

6.2 Device Fabrication

The device was fabricated on a double sided polished, 250 µm ± 10 µm thick, four inch diameter lightly doped p-type wafer. Thin wafers have the advantage during bulk

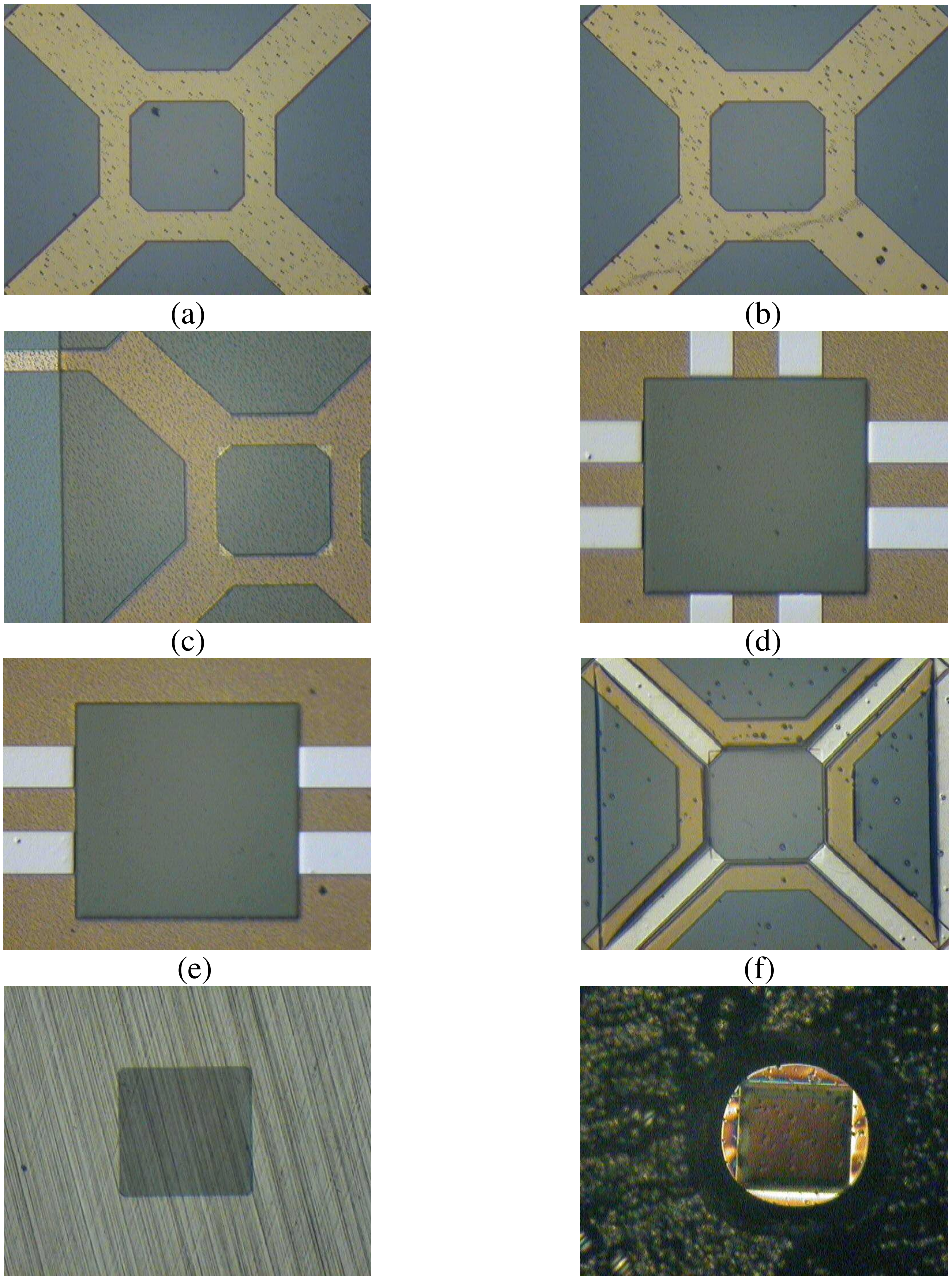

(a) (b)

(c) (d)

(e) (f)

(g) (h)

Figure 6.2 Microscopic view of microspectrometer at the end of different fabrication steps (a) after bottom electrode patterning (b) after bottom mirror patterning (c) after sacrificial polyimide patterning (d) after top electrode patterning (e) after top mirror patterning (f) after top Al_2O_3 electrode patterning (g) after backside Al etching (h) after bulk micromachining (picture 6.2 (h) was taken from back side of the wafer, the bottom of the Al layer can be seen through hole)

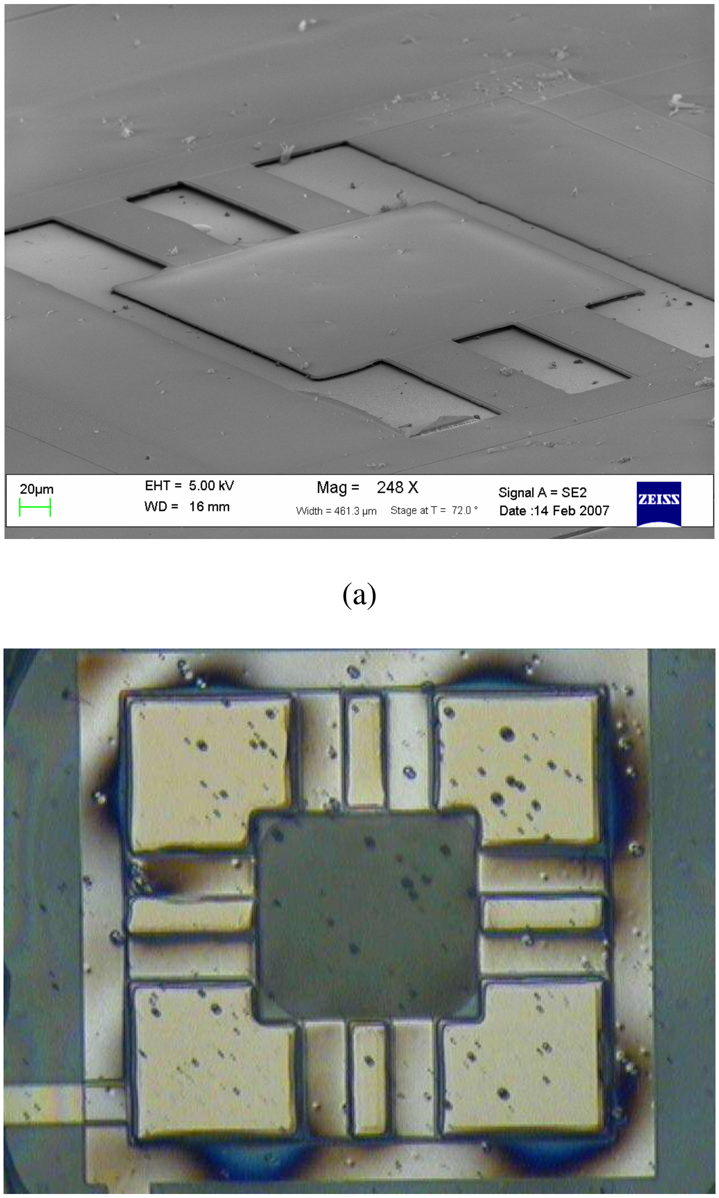

(a)

(b)

Figure 6.3 Completed microspectrometer after ashing (a) SEM picture (b) optical microscope picture micromachining [etching the silicon substrate from backside] process. The fabrication started with a 400-nm thick Al layer deposited on the back side of the wafer by an electron beam evaporator. The cryopump of the evaporator was cooled down to 10 K and then the substrate was loaded inside the chamber. The chamber was pumped down to a base pressure of 7.1×10^{-7} Torr. 99.999% pure Al pallets from Kurt J. Lesker Company were used as the evaporation source. After creating plasma in the system, the electron beam was swiped in both vertical and horizontal directions on a crucible containing the Al pallets during the evaporation process. Beam intensity was controlled to obtain an evaporation rate of about 1.1 nm/sec. A thickness monitor mounted approximately at the same height of sample, was used to monitor the film thickness while deposited. After obtaining the desired thickness, both the substrate and the source shutters were closed. The deposited Al film was found to be very uniform in thickness throughout the wafer surface and looked shiny. This deposited Al layer after patterning will be acting as the shield layer for incident infrared radiation. Then Al_2O_3 was deposited by RF magnetron sputtering. The same sputtering system mentioned in earlier chapters and commercially available 99.99% pure Al_2O_3 target were used for this purpose. It took about 24 hours of sputtering time to deposit 1.5-μm-thick Al_2O_3. An RF power of 200 W with an Argon gas flow of 36 SCCM was used to sputter. After every 5 hours the RF power supply of the sputtering system was turned off for about half an hour to cool down the sputtering system. During that interval time, Ar gas flow was kept on to avoid the layers formation rather than a single layer formed by continuous sputtering. The RF power turned on and turned off to the Al_2O_3 target very slowly to avoid cracking of target due to temperature gradient created by insulating property of Al_2O_3. This Al_2O_3 layer will be acting as the etch stop for bulk micromachining and also the bottom support layer for spectrometer. Then bottom electrode of Al was deposited by using a thermal evaporator. The cryo pump was cooled to 10 K after which the substrate was mounted. Then the chamber was evacuated to 2.1×10^{-6} Torr prior to evaporation. An evaporation rate of 4-5 angstrom/sec was obtained by using a current of 100 Ampere. Source shutter was closed after obtaining the desired thickness of 400 nm which was monitored by a thickness monitor mounted near to the substrate holder. The Al was patterned by lift off by using negative resist NR7-1500P and according to the same procedure mentioned in section 4.2. This Al layer can be seen in Figure 6.2 (a). Then the bottom Al mirror was deposited by using an electron beam evaporator. The Al mirror's thickness was controlled precisely to obtain a thickness of 8 nm. This Al was patterned by lift off. After patterning the bottom Al mirror, the device was looking like Figure 6.2 (b). Since the Al layer was very thin so by looking at the optical microscope picture, it is very hard to differentiate it from the previous step. Then the polyimide, PI 2737 from HD Microsystem, was spin coated to be used as the sacrificial layer to form the cavity. After spin coating, PI 2737 was patterned and cured according to the method mentioned in section 4.2. After cure, the polyimide thickness was found to be 2.2 μm. Figure 6.2 (c) shows the microscopic picture of the device after the polyimide was cured. Then the top Al electrode (400 nm thick) was deposited by electron beam evaporation and patterned by lift off by using negative resist NR7-1500P. Figure 6.2 (d) shows the optical microscope picture of the device after the top electrode is deposited. A 14-nm-thick top Al mirror was deposited by electron beam evaporation and patterned by lift off with negative resist.

Figure 6.2 (e) shows the microscopic picture of the device after the top mirror was deposited. The top Al_2O_3 layer of 1.5 μm thickness was deposited by RF magnetron sputtering after this and patterned by lift off with the help of positive resist S1813 and lift off resist LOR 3B, both are manufactured by Microchem Corporation. For this purpose, the same procedure was followed as mentioned before in chapter 3. The combination of lift off resist LOR 3B, and positive resist S1813 was seemed to be worked out nicely for lifting off 1.5-μm-thick film of Al_2O_3. Figure 6.2 (f) shows the optical microscope picture of the device after depositing top Al_2O_3 layer. Then, the bottom Al shield layer was patterned by commercially available Al etchant. Negative resist NR7-1500P was spin coated on the backside of the wafer at 3000 rpm for 30 seconds followed by a pre bake at 150 ^{o}C for 60 seconds. Then, the wafer was aligned with respect to the front side features and alignment marks. For this purpose, both the front and back side cameras of the aligner were used. After exposing, post exposure bake was done at 120 ^{o}C for 60 seconds, followed by developing in it negative resist developer, RD6, for 50 seconds. Then, the resist was hard baked at 180 ^{o}C for 300 seconds to make it suitable to withstand in Al etchant. Figure 6.2 (g) shows the optical microscope picture after Al etching. To perform the bulk micromachining by using deep reactive ion etching (DRIE), it was necessary to use a resist as mask. A special thick negative resist SU-8 2010 for microelectromechanical system (MEMS) applications, from Microchem Corporation, was selected for this purpose. This resist has a selectivity of 1:8 over the silicon substrate while subjected to DRIE treatment. The wafer was dehydrated first by keeping it on hot plate for 300 seconds at 200 ^{o}C. SU-8 2010 was spin coated at 1450 rpm for 50 seconds. Then it was soft baked on hot plates at 65 and 95 ^{o}C respectively, both for 3 minutes. It was then exposed and post exposure bake was done on hot plates at 65 and 95 ^{o}C respectively, both for 3 minutes. The resist was developed in the SU-8 developer from the Microchem Corporation for 3 minutes. The resist thickness was found to be ~9 μm. A fully automatic DRIE system from TRION was used to perform the bulk micromachining. The system's gas flow was set according to following:

$CF_4 \rightarrow 0$ SCCM

$O_2 \rightarrow 50$ SCCM

$SF_6 \rightarrow 50$ SCCM

$Ar \rightarrow 200$ SCCM

$He \rightarrow 200$ SCCM

The RIE power of 50 W with a process pressure of 50 mTorr was used. The DRIE was run for 800 seconds at a time during which time a total Si substrate etch of about 12 μm was obtained. The wafer was needed to be patterned with SU-8 2010 resist for 4 times during this process. Figure 6.2 (h) shows the optical microscope picture after completion of bulk micromachining. Then the sacrificial polyimide was removed by ashing the device in oxygen plasma for about 180 hours. The chamber pressure was 0.5 mbar and RF power was 150 W during this ashing process. The ashing process was interrupted after every 3 hours to cool down the asher. Figure 6.3 (a) and 6.3 (b) shows picture of the completed device taken by SEM and optical microscope respectively.

6.3 Conclusions

Cavity based Fabry-Perot microspectrometer was fabricated using only polyimide, Al and Al_2O_3 layers on a thin double sided polished Si wafer. The device is under test to measure its performance.

CHAPTER 7

SUMMARY AND CONCLUSIONS

7.1 Si_xGe_{1-x} and $Si_xGe_{1-x}O_y$ Thin Films For Infrared Sensing Material

Thin films of Si_xGe_{1-x} and $Si_xGe_{1-x}O_y$ were deposited by RF magnetron sputtering to find a suitable atomic combination to be used as sensing material for uncooled infrared detection. The silicon and oxygen concentrations were varied in a parametric investigation of the dependence of the electrical and optical characteristics of the thin films on composition.

As Si concentration was increased in Si_xGe_{1-x} films, TCR was decreased. For $Si_xGe_{1-x}O_y$ films, the addition of oxygen to Si_xGe_{1-x}, increased the activation energy, and TCR. TCR was measured to vary from -2.27 %/K to -8.69 %/K. The optical bandgap was increased with the increasing concentration of oxygen in $Si_xGe_{1-x}O_y$. The normalized Hooge coefficient for 1/*f*-noise was found to increase with the increasing concentration of O_2. With the addition of O_2 to Si_xGe_{1-x}, the transmittance of the films found to be increased while the reflectance remained almost constant. The optical bandgap was increased with the increasing concentration of O_2. A suitable atomic composition of $Si_xGe_{1-x}O_y$ for uncooled infrared detector applications was found to have a TCR of -5.10 %/K although presence of high 1/*f*-noise seemed to be a concern of degrading bolometer's performance.

7.2 Doped Si_xGe_{1-x} Microbolometers

Microbolometers of doped Si_xGe_{1-x} were fabricated and characterized. A TCR of 1.25%/K with a device resistance of 41.4 KΩ was achieved. Thermal conductivity was found to be 1×10^{-5} WK^{-1} for these doped Si_xGe_{1-x} microbolometers. The presence of high 1/*f*-noise was observed which caused to degrade bolometers performance.

7.3 Forming Gas Passivation of $Si_xGe_{1-x}O_y$ Microbolometers

This work reported the reduction of noise voltage PSD of a-$Si_xGe_{1-x}O_y$ microbolometers by forming gas passivation. Microbolometers fabricated from $Si_xGe_{1-x}O_y$ were passivated in a rapid thermal annealing chamber in presence of forming gas at 250 °C for 0.5 hour, 1 hour, 2 hours, 3 hours, 4 hours and 8 hours. The noise voltage PSD was measured at different bias currents before and after passivation.

The noise voltage PSD of the bolometers was found to be decreased as the passivation time increased. The 1/*f*-noise coefficient (K_f) was decreased from 7.54×10^{-7} to 2.21×10^{-10} after 8 hours of forming gas passivation performed at 250 °C. It was also found that passivating the samples for excess amount of time (8 hours of passivation time as compared to 6 hours case), increased the value of K_f leading to depassivation of $Si_xGe_{1-x}O_y$ sensing layer.

7.4 Fabrication and Characterization of a-$Si_xGe_{1-X}O_y$:H Microbolometers

Uncooled a-$Si_xGe_{1-x}O_y$ microbolometers were fabricated. Fabricated bolometers were passivated for 6 hours and 7 hours in forming gas at 250 °C. Polyimide was used as the sacrificial layer to form the cavity of microbolometers. Suspended bridge like structures were formed by employing NiCr arms. Silicon nitride was used to form the sandwich structure of $Si_xGe_{1-x}O_y$ to add mechanical strength to the pixel.

Four bolometers were characterized to determine their figures of merits. The highest responsivity and detectivity obtained from $Si_xGe_{1-x}O_y$:H microbolometers were 1.05×10^4 V/W and 8.27×10^6 cm-$Hz^{1/2}$/W respectively while the room temperature TCR was -4.80%/K. The lowest thermal conductivity was found to be 4×10^{-8} WK^{-1}. The high value of voltage responsivity with moderate pixel resistance (743 kΩ) was resulted from the combined effect of low thermal conductivity, high TCR, use of Al mirror, and the absorber material. The low value of thermal conductance reflects state-of-art thermal isolation between the substrate and pixel. The presence of 1/*f*-noise was found to be the main cause of reducing the detectivity of the device. If the detectivity was limited by Johnson noise, then the value of detectivity would have been 7.60×10^8 cm-$Hz^{1/2}$/W at 2 μA bias current. So, further investigations needed to reduce the 1/*f*-noise to improve the performance of the device.

7.5 Fabrication of Cavity Based Fabry-Perot Microspectrometer

Cavity based tunable Fabry-Perot microspectrometer was fabricated. Si substrate used for fabrication had been etched away by using DRIE system from the back side. Fabrication of different layers had been discussed. Al_2O_3 was used as the support layers for both top and bottom parts of the cavity. Al was used as the material for fabricating mirror and electrode arms for both top and bottom layers. The cavity was formed by using sacrificial polyimide.

The device is still under test to measure its performance.

REFERENCES

[1] E. L. Dereniak, and G. D. Boreman , “Infrared detectors and systems,” New York: John Wiley & Sons, 1996, chap. 5, 9.

[2] M. M. Rana, and D. P. Butler, “Radio frequency sputtered $Si_{1-x}Ge_x$ and $Si_{1-x}Ge_xO_y$ thin films for uncooled infrared detectors,” Thin Solid Films, vol. 514, 2006, pp. 355-360.

[3] S. Sedky, P. Fiorini, K. Baert, and R. Mertens, “Characterization and optimization of infrared poly SiGe bolometers,” IEEE Transaction of Electron Devices, vol. 46, no. 4, 1999, pp. 675-682.

[4] F.N. Hooge, “*1/f* noise is no surface effect,” Physics Letters, vol. 29A, no. 3, 1969, pp. 139-140.

[5] D. P. Butler, Z. Çelik-Butler, and R. Sobolewski, “Yttrium barium copper oxide as an infrared radiation sensing material,” in Handbook of Advanced Electronic and Photonic Material and Devices, Edi. H. S. Nalwa, vol. 3, 2001, pp. 169-195.

[6] M. Almarsi, D. P. Butler, and Z. Çelik-Butler, "Self-supporting uncooled infrared microbolometers with low-thermal mass," Journal of Microelectromechanical Systems, vol. 10, no. 3, 2001, pp. 469-476.

[7] L. Dobrzanski, E. Nossarzewska-Orlowska, Z. Nowak, and J. Piotroski, "Micromachined silicon bolometers as detectors of soft X-ray, ultraviolet, visible

and infrared radiation," Sensors and Actuators A: physical, vol. 60, 1997, pp. 154-159.

[8] S. Sedky, P. Fiorini, M. Caymax, S. Loreti, K. Baert, L. Hermans, and R. Mertens, "Structural and mechanical properties of polycrystalline silicon germanium for micromachining applications," Journal of Microelectromechanical Systems, vol. 7, no. 4, 1998, pp. 365-371.

[9] C. Chen, X. Yi, J. Zhang, and X. Zhao, "Linear uncooled microbolometer array based on VO_x thin films," Infrared Physics and Technology, vol. 42, 2001, pp. 87-90.

[10] X. He, G. Karunasiri, T. Mei, W. J. Zeng, P. Neuzil, and U. Sridhar, “Performance of microbolometer focal plane array under varying pressure,” IEEE Electron Device Letter, vol. 21, no. 5, 2000, pp. 233–235.

[11] E. Monticone, L. Boarino, G. Lérondel, R. Steni, G. Amato, and V. Lacquaniti, “Properties of metal bolometers fabricated on porous silicon,” Applied Surface Science, vol. 142, 1999, pp. 267–271.

[12] J. S. Shie, Y. M. Cheng, M. Ou-Yang, and B. C. S. Chou, “Characterization and modeling of metal-film microbolometer,” Journal of Microelectromechanical Systems, vol. 5, no. 4, 1996, pp. 298–306.

[13] T. A Enukova, N. L. Ivanova, Y. V. Kulikov, V. G. Malyarov, and I. A. Khrebtov, “Amorphous silicon and germanium films for uncooled microbolometers,” Technical Physics Lettter, vol. 23, no. 7, 1997, pp. 504–506.

[14] M. García, R. Ambrosio, A Torres, and A. Kosarev, "IR bolometers based on amorphous silicon germanium alloys," Journal of Non-Crystalline Solids, vol. 338-340, 2004, pp. 744-748.

[15] C. Marshall, N. Butler, R. Blackwell, R. Murphy, and T. Breen, "Uncooled infrared sensor with digital focal plane array," Proceedings of SPIE, vol. 2746, 1996, pp. 23-31.

[16] T. Breen, N. Butler, M. Kohin, C. A. Marshall, R. Murphy, T. Parker, and R. Silva, "More applications of uncooled microbolometer sensors," Proceedings of SPIE, vol. 3436, 1998, pp. 530-540.

[17] E. Iborra, M. Clement, L. V. Herrero, and J. Sangrador, "IR uncooled bolometers based on amorphous $Ge_xSi_{1-x}O_y$ on silicon micromachined structures," Journal of Microelectromechanical Systems, vol. 11, no. 4, 2002, pp. 322-329.

[18] A.H.Z. Ahmed, and R.N. Tait, "Characterization of $Ge_xSi_{1-x}O_y$ for micromachined uncooled bolometer application," Journal of Applied Physics, vol. 94, no. 8, 2003, pp. 5326-5532.

[19] M. Clement, E. Iborra, J. Sangrador, and I. Barberán, "Amorphous $Ge_xSi_{1-x}O_y$ thin films for integrated sensor applicationson," Journal of Vacuum Science Technology B, vol. 19, no. 1, 2001, pp. 294-298.

[20] A. Ahmed, and R. N. Tait, "Noise behavior of amorphous $Ge_xSi_{1-x}O_y$ for microbolometer applications," Infrared Physics & Technology, vol. 46, 2005, pp. 468-472.

[21] J. Tauc, R. Grigorovici, A. Vancu, “Optical properties and electronic structure of amorphous germanium,” Physics Status Solidi, vol. 15, 1966, pp. 627-637.

[22] A.H. Moharram, A.A. Othman, M.A. Osman, “Optical characterization of amorphous $Ga_{50}Se_{45}S_5$ films,” Applied Surface Science, vol. 200, 2002, pp. 143-149.

[23] H. Kavak, S. Eker, and A. Mamedov, “Harmonic oscillator model and determination of optical parameters,” Journal of Quantitative Spectroscopy and Radiative Transfer, vol. 86, 2004, pp. 223-229.

[24] T.H Bang, S.H. Choe, B.N Park, M.S. Jin, and W.T Kim, “Optical energy gap of $CuAl_2S_4$,” Semiconductor Science and Technology, vol. 11, 1996, pp. 1159-1162.

[25] N.F. Mott, and E.A. Davis, Electronic Processes in Non-crystalline Materials, Clarendon, Oxford, 1979, ch. 1.

[26] A. Mahmood, S. Dayeh, D. P. Butler, and Z. Celik-Butler, “Micromachined infrared sensor arrays on flexible polyimide substrates”, Proceedings of IEEE Sensors, vol. 2, 2003, pp. 777 – 782,

[27] A. Ahmed, R.N. Tait, “Fabrication of a self-absorbing, self-supported complimentary metal-oxide-semiconductor compatible micromachined bolometer” Journal of Vacuum Science & Technology A, vol. 22, no. 3, 2004, pp. 842-846.

[28] M. Galeazzi, K. R. Boyce, R. Brekosky, J. D. Gygax, R. L. Kelley, D. Liu, D. McCammon, D. B. Mott, F. S. Porter, W. T. Sanders, C. K. Stahle, C. M. Stahle, A. E. Szymkowiak, and P. Tan, “Non-ideal effects in doped semiconductor

thermistors," LOW TEMPERATURE DETECTORS: Ninth International Workshop on Low Temperature Detectors, Edi. F.S. Porter, D. McCammon, M. Galeazzi, and K**.** Stahle, Madison, Wisconsin, 2001, Proceedings 2002, pp. 83-86.

[29] C. Boehme, and G. Lucovsky, "Origins of silicon solar cell passivation by SiN_x:H anneal," Journal of Non-Crystalline Solids, vol. 299-302, part 2, 2002, pp. 1157-1161.

[30] M. Zacharias, J. Bläsing, M. Löhman, and J. Christen, "Formation of GeO_x and $SiGeO_x$ alloy films," Thin Solid Films, vol. 278, 1996, pp. 32-36.

[31] F. N. Hooge, "1/f noise sources," IEEE Transaction on Electron Devices, vol. 41, no. 11, 1994, pp. 1926-1935.

[32] B. K. Jones, "Electrical noise as a reliability indicator in electronic devices and components," IEE Proceedings on Circuits, Devices and Systems, vol. 149, no. 1, 2002, pp. 13 -22.

[33] A. van der Ziel, "Noise in solid state devices and circuits," Wiley, New York, 1986..

[34] M. Zacharias, R. Weygand, B. Dietrich, F. Stolze, J. Bläsing, P. Veit, T. Drüsedau, and J. Christen, "A comparative study of Ge nanocrystals in $Si_xGe_yO_z$ alloys and SiO_x/GeO_y multilayers," Journal of Applied Physics, vol. 81, no. 5, 1997, pp. 2384-2390.

[35] S. P. Karna, H. A. Kurtz, W. M. Shedd, R. D. Pugh, and B. B. K. Singaraju, “New fundamental defects in a-SiO_2,” IEEE Transaction on Nuclear Science, vol. 46, no. 6, 1999, pp. 1544-1552.

[36] A. Stirling, and A. Pasquarello, “First-principles modeling of paramagnetic Si dangling-bond defect in amorphous SiO_2,” Physical Review B, vol. 66, 2002, pp. 245201-11.

[37] T. Uchino, M. Takahashi, and T. Yoko, “Model of a switching oxide trap in amorphous silicon dioxide,” Physical Review B, vol. 64, 2001, pp. 081310-4.

[38] S. Mukhopadhyay, P. V. Sushko, A. M. Stoneham, and A. L. Shluger, “Modeling of the structure and properties of oxygen vacancies in amorphous silica,” Physical Review B, vol. 70, 2004, pp. 195203-15.

[39] M. J. Kerr, J. Schmidt, A. Cuevas, and J. H. Bultman, “Surface recombination velocity of phosphorus-diffused silicon solar cell emitters passivated with plasma enhanced chemical vapor deposited silicon nitride and thermal silicon oxide,” Journal of Applied Physics, vol. 89, no. 7, 2001, pp. 3821-3826.

[40] W. Orellana, “Energetic of nitrogen incorporation reactions in SiO_2,” Applied Physics Letter, vol. 84, no. 6, 2004, pp. 933-935.

[41] W. L. Warren, K. Simmons-Potter, B. G. Potter, and J. A. Ruffner Jr., “Charge trapping, isolated Ge defects, and photosensitivity in sputter deposited GeO_2 : SiO_2 thin films,” Applied Physics Letter, vol. 69, no. 10, 1996, pp. 1453-1455.

[42] A. Daami, A Zerrai, J. J. Marchand, J. Poortmans, and G. Brémond, "Electrical defect study in thin-film SiGe/Sisolar cells," Materials Science in Semiconductor Processing, vol. 4, 2001, pp. 331-334.

[43] R. E. Johanson, M. Gunes, and S. O. Kasap, "1/f noise in hydrogenated amorphous silicon-germanium alloys", IEE Proceedings on Circuits Devices and Systems, vol. 150, no. 4, 2003, pp. 345-349.

[44] S. Honda, T. Mates, M. Ledinsky, J. Oswald, A. Fejfar, J. Kočka, T. Yamazaki, Y. Uraoka, and T. Fuyuki, "Effect of Hydrogen passivation on polycrystalline silicon thin films," Thin Solid Films, vol. 487, 2005, pp. 152-156.

[45] S. N. Rashkeev, D. M. Fleetwood, R. D. Schrimpf, and T. Pantelides, "Proton-induced defect generation at the Si-SiO_2 interface," IEEE Transactions on Nuclear Science, vol. 48, no. 6, Dec. 2001, pp. 2086-2092.

[46] A.J. Syllaios, T.R. Schimert, R.W. Gooch, W.L. McCardel, B.A. Ritchey, and J.H. Tregilgas, "Amorphous silicon microbolometer technology," Material Resource Society Symposium Proceedings, no. 609, 2000, pp. A14.4.1.

[47] J. J. Yon, A. Astier, S. Bisotto, G. Chamingis, A. Durand, J. L. Martin, E. Mottin, J. L. Ouvrier-Buffet, and J. L. Tissot, "First demonstration of 25-µm pitch uncooled amorphous silicon microbolometer IRFPA at LETI-LIR," Proceedings of SPIE, vol. 5783. April. 2005, pp. 432-440.

[48] P. D Moore, S Kavadias, V. Leonov, and C. V. Hoot, “Process development of fast and sensitive polySiGe microbolometer arrays,” Proceedings of SPIE, vol. 4288, 2001, pp. 94-99.

[49] D. Liang, Y. Rui-Feng, and L. Li-Tian, “Characterization of uncooled poly SiGe microbolometer for infrared detection,” Chinese Physics Letter, vol. 20, no. 5, May 2003, pp. 770-773.

[50] M. Almasri, Z. Çelik-Butler, D.P. Butler, A. Yaradanakul, and A. Yildiz, "Uncooled multimirror broad-band IR microbolometers," Journal of Microelectromechanical Systems, vol. 11, no. 5. Oct. 2002, pp. 528-535.

[51] A. Mahmood, “Device level vacuum packaged microbolometer on flexible substrate,” PhD. Dissertation, The University of Texas, Arlington, 2005, pp. 123-143.

BIBLIOGRAPHICAL INFORMATION

Mukti M Rana was born in Chapai Nawabganj, Bangladesh in 1973. He got BSc. in Electrical and Electronics Engineering in 1997 from Khulna University of Engineering and Technology, Khulna, Bangladesh. He completed his Masters and PhD. in Electrical Engineering from The University of Texas, Arlington in May, 2002 and in May, 2007 respectively.

Mr. Rana's research interest includes uncooled infrared detectors, noise in thermal detectors, pressure and acceleration sensors.